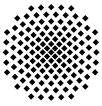

University of Stuttgart
Germany

Hybrid plasmonic structures for giant Faraday rotation

Von der Fakultät Mathematik und Physik der Universität Stuttgart
zur Erlangung der Würde eines Doktors der
Naturwissenschaften (Dr. rer. nat.) genehmigte Abhandlung

vorgelegt von
Dominik Franz Flöß
aus Inneringen

Hauptberichter: Prof. Dr. Harald Giessen
Mitberichterin: Prof. Dr. Stefanie Barz
Vorsitzender: Prof. Dr. Christian Holm

Tag der mündlichen Prüfung: 04.10.2017

4. Physikalisches Institut der Universität Stuttgart

Oktober 2017

I hereby certify that this dissertation is entirely my own work except where otherwise indicated. Passages and ideas from other sources have been clearly indicated.

Stuttgart, October 2017

Dominik Franz Flöß

ABSTRACT

When linearly polarized light propagates through a magneto-optic material with an applied static magnetic field, the polarization plane of the electromagnetic wave is rotated by an angle. This phenomenon is known as the Faraday effect. An intriguing and unique property of this effect is that both time-reversal symmetry and Lorentz reciprocity are broken. For that reason, Faraday rotators are widely utilized as core elements in nonreciprocal optical devices such as optical isolators, which require a Faraday rotation of 45° in order to ensure one-way light propagation.

Most systems that involve Faraday rotators have recently undergone massive miniaturization. Hence, there is a high demand for down-sized Faraday rotators. However, such systems are very challenging to realize, since Faraday rotation is proportional to the thickness of the magneto-optic material. Therefore, when the size of a magneto-optic crystal is decreased, the achievable Faraday rotation is smaller. A key to overcome this problem lies with plasmonic nanostructures: In this dissertation, it is demonstrated that the Faraday effect of a dielectric thin film can be enhanced significantly by the incorporation of a nanosized metallic grating. Different approaches based on EuSe and EuS thin films are investigated both in experiment and theory. An important outcome of the theoretical analysis is that the working principle of such structures can be described elegantly by means of a simple harmonic oscillator model based on the Lorentz force.

At low temperatures, the presented hybrid magnetoplasmonic structures yield giant Faraday rotation of up to 14° for a thickness of less than 200 nm and a magnetic field of 5 T. By varying the magnetic field from -5 to $+5$ T, a rotation tuning range of over 25° is realized. As this performance is only a factor of three away from the Faraday isolation requirement, the demonstrated concept could lead to highly integrated, nonreciprocal photonic

devices for optical isolation, light modulation, and optical magnetic field sensing.

DEUTSCHE ZUSAMMENFASSUNG

Propagiert linear polarisiertes Licht durch ein magneto-optisches Medium, so bewirkt ein angelegtes statisches Magnetfeld eine Drehung der Polarisation der elektromagnetischen Welle. Dieses Phänomen wird als Faraday-Effekt bezeichnet. Was diesen Effekt besonders auszeichnet, ist die Tatsache, dass durch den Einfluss des angelegten Magnetfeldes sowohl die Zeitumkehrinvarianz, als auch die Lorentz-Reziprozität gebrochen werden. Aufgrund dieser Eigenschaft, werden Faraday-Rotatoren als Grundbaustein in einer Vielzahl von nichtreziproken optischen Systemen eingesetzt. Das wichtigste Beispiel sind optische Isolatoren, die eine Faraday-Rotation von 45° benötigen, um Licht in Vorwärtsrichtung zu transmittieren und in Rückwärtsrichtung vollständig zu blockieren.

Sehr viele optische Komponenten, die Faraday-Rotatoren beeinhalten, unterliegen dem Trend hin zu immer stärkerer Miniaturisierung. Daraus folgt ebenfalls ein großer Bedarf an Faraday-Rotatoren mit kleinsten räumlichen Abmessungen. Allerdings ist die Realisierung solcher Systeme sehr anspruchsvoll, da die Faraday-Rotation proportional zur Dicke des verwendeten magneto-optischen Materials ist. Das bedeutet, dass mit einem kleineren magneto-optischen Kristall auch die maximal erreichbare Faraday-Rotation sinkt. Um diesem Verhalten entgegenzuwirken, werden in dieser Dissertation mehrere neuartige Methoden vorgestellt, die es erlauben den Faraday-Effekt eines Dünnfilms mithilfe von periodischen metallischen Nanostrukturen zu verstärken. Die verschiedenen Ansätze werden sowohl experimentell, als auch theoretisch untersucht. Weiterhin wird gezeigt, dass das magneto-optische Verstärkungsprinzip der Nanostrukturen mithilfe eines einfachen Oszillatormodells elegant beschrieben werden kann.

Die in dieser Dissertation vorgestellten hybriden magnetoplasmonischen Systeme bestehen aus EuSe- und EuS-Dünnfilmen, sowie aus Gold-Nanogittern. Es wird gezeigt, dass diese weniger als 200 nm dicken Strukturen bei einer Temperatur von 20 K und einem statischen Magnetfeld von 5 T eine Faraday-Rotation von bis zu 14° erzeugen können. Weiterhin kann die Polarisation des transmittierten Lichts durch Umpolung und Variation des Magnetfeldes über einen 25° breiten Winkelbereich hinweg reguliert werden. Da die für optische Isolation benötigte Drehung von 45° nur einen Faktor drei größer ist als die von der Dünnfilmstruktur erreichte Faraday-Rotation, ist das hier präsentierte Konzept sehr vielversprechend und könnte wichtige Anwendungen im Bereich integrierter nichtreziproker photonischer Systeme finden. Besonders herauszustellen sind hier Anwendungen in den Bereichen optische Isolation, Lichtmodulation und Magnetfeldmessung.

PUBLICATIONS

Parts of this work have already been published in scientific journals:

1. D. Floess, M. Hentschel, T. Weiss, H.-U. Habermeier, J. Jiao, S. G. Tikhodeev, and H. Giessen,
   "*Plasmonic Analog of Electromagnetically Induced Absorption Leads to Giant Thin Film Faraday Rotation of 14°*," Physical Review X **7**, 021 048 (2017).

2. D. Floess, T. Weiss, S. G. Tikhodeev, and H. Giessen, "*Lorentz nonreciprocal model for hybrid magnetoplasmonics*," Physical Review Letters **117**, 063 901 (2016).

3. D. Floess, J. Y. Chin, A. Kawatani, D. Dregely, H.-U. Habermeier, T. Weiss, and H. Giessen,
   "*Tunable and switchable polarization rotation with nonreciprocal plasmonic thin films at designated wavelengths*," Light: Science & Applications **4**, e284 (2015).

Parts of this thesis have also been presented at international conferences:

1. D. Floess, T. Weiss, S. G. Tikhodeev, M. Hentschel, and H. Giessen, "*Plasmonically driven Lorentz non-reciprocal nanooptics*," Nanometa Conference, Seefeld, Austria (2017).
   Session: "**Programme Committee Top Picks**".

2. T. Weiss, D. Floess, M. Schäferling, M. Mesch, H. Giessen, W. Langbein, and E. A. Muljarov, "*Optical resonances and their normalization: Efficient modeling in nanophotonics*," Nanometa Conference, Seefeld, Austria (2017).

3. D. Floess, M. Hentschel, T. Weiss, H.-U. Habermeier, J. Jiao, S. G. Tikhodeev, and H. Giessen, "*Plasmonic analog of electromagnetically induced absorption leads to giant thin-film Faraday*

rotation," Spring Meeting of the German Physical Society, Dresden, Germany (2017).

4. D. Floess, T. Weiss, S. G. Tikhodeev, and H. Giessen, "*Analytical model for hybrid magnetoplasmonics*," Spring Meeting of the German Physical Society, Regensburg, Germany (2016).

5. D. Floess, T. Weiss, S. G. Tikhodeev, and H. Giessen, "*Tunable and switchable Faraday rotation in magnetoplasmonic waveguides: Classical harmonic oscillator modeling*," Nanometa Conference, Seefeld, Austria (2015).

6. S. G. Tikhodeev, D. Floess, T. Weiss, and H. Giessen, "*Resonantly enhanced Faraday rotation in magnetoplasmonic waveguides*," XIX International Symposium on Nanophysics and Nanoelectronics, Nizhny Novgorod, Russia, (2015).

7. D. Floess, T. Weiss, S. G. Tikhodeev, and H. Giessen, "*Tunable and switchable thin film Faraday rotation in magnetoplasmonic waveguides: experiments and coupled oscillator model*," Spring Meeting of the German Physical Society, Berlin, Germany (2015).

8. D. Floess, J. Y. Chin, A. Kawatani, D. Dregely, H.-U. Habermeier, T. Weiss, and H. Giessen, "*Tunable and switchable polarization rotation with magnetoplasmonic thin-films*," META Conference, Singapore (2014).

9. D. Floess, J. Y. Chin, A. Kawatani, D. Dregely, H.-U. Habermeier, T. Weiss, and H. Giessen, "*Plasmonically enhanced thin film Faraday effect with up to 4 degrees rotation*," Spring Meeting of the German Physical Society, Dresden, Germany (2014).

Further publications and contributions which are not covered in this dissertation:

1. B. Metzger, L. Gui, J. Fuchs, D. Floess, M. Hentschel, and H. Giessen, "*Strong Enhancement of Second Harmonic Emission by Plasmonic Resonances at the Second Harmonic Wavelength*," Nano Letters **15**, 3917 (2015).

2. L. Gui, J. Fuchs, B. Metzger, D. Floess, M. Nesterov, and H. Giessen, "*Nonlinear plasmonics of aluminum nanoantennas resonant at the second harmonic frequency*," Spring Meeting of the German Physical Society, Berlin, Germany (2015).

3. D. Floess, E. Andersson, M. Hillery, "*Quantum algorithms for testing and learning Boolean functions*," Mathematical Structures in Computer Science **23**, 386 (2013).

CONTENTS

1 INTRODUCTION

The presence of a static magnetic field influences the optical properties of certain materials that are referred to as magneto-optic (MO) materials. This gives rise to several MO effects, such as the Faraday effect [1] in transmission and the MO Kerr effect in reflection [2]. Here, the Faraday effect is of special interest as it is the potentially largest MO effect. It describes the following phenomenon: When linearly polarized light propagates through a MO material, in the direction of an applied static magnetic field B, the polarization plane of the electromagnetic wave is rotated by the angle

$$\theta = VBz, \tag{1.1}$$

where z is the thickness of the material and V is the material specific Verdet constant. A very intriguing and unique property of the Faraday effect is that time-reversal symmetry and Lorentz reciprocity are broken [3]. As a result, the direction of the polarization rotation is determined by the direction of the applied magnetic field and not by the direction of the wave vector of the incident light. This fact fundamentally distinguishes it from effects such as optical activity [4]. MO effects are actually the only practical way to break Lorentz reciprocity in passive optical systems, since other approaches rely on either nonlinear effects [5–7] or time modulation [8–12]. For that reason, Faraday rotators are widely utilized as core elements in nonreciprocal optical devices such as optical isolators [13], which require a Faraday rotation of 45°. As such, Faraday rotators are essential components in a multitude of optical systems, including optical telecommunication networks [14–16] and laser systems [17–19]. Furthermore, Faraday rotators are also attractive for magnetic field sensing [20, 21] and optical modulation [22].

Most systems that involve Faraday rotators have recently undergone massive miniaturization. Hence, there is a high demand for down-sized Faraday rotators [23, 24]. However, such systems are very challenging to realize, since, according to equation (1.1), Faraday rotation is proportional to the thickness of the MO material. A promising approach to overcome this problem is to combine MO materials with plasmonic nanostructures. It has been demonstrated that this combination enables nanoscale optical systems that offer magnetic tunability as well as strong nonreciprocal optical response in ultracompact structures [25–31]. The first approaches to enhance Faraday rotation of conventional materials were based on MO nanoparticles [32], photonic crystals [33–37], and microcavities [38–40] but were hampered by either weak MO effects or relatively large structure sizes that are also difficult to fabricate. There have also been efforts to enhance the rather weak MO Kerr effect in reflection by means of ferromagnetic metallic nanoparticles [41–44] and dielectric films [45]. Considerable attention was received by a recent approach by Chin *et al.*, where the Faraday rotation of a dielectric bismuth-iron-garnet (BIG) thin film is enhanced by attaching a metal grating [46, 47], resulting in a Faraday rotation of about 0.8° for a 215 nm thick structure. Here, the strong Faraday rotation originates from the interaction between waveguide resonances in the BIG thin film and localized surface plasmon resonances (LSPRs) in the metal grating [48–50]. At that time, this performance was already a remarkable achievement considering that conventional Faraday rotators require centimeter sized crystals to achieve 45° rotation.

In this dissertation the approach by Chin *et al.* is further developed in various ways, resulting in novel magnetoplasmonic systems with significantly larger Faraday rotation. In addition to the experimental demonstration of these systems, the underlying MO enhancement mechanism is unraveled by introducing a theoretical description based on harmonic oscillators. The dissertation is divided into four main parts:

As a theoretical primer, chapter 2 introduces all physical concepts involved in hybrid magnetoplasmonic systems. This includes magneto-optic effects, plasmonics and the optical properties of corrugated waveguides. Furthermore, the utilized experimental setup for measuring Faraday rotation of nanostructures is explained.

In chapter 3, the hybrid magneto-plasmonic approach by Chin *et al.* is employed and advanced to 220 nm thick devices, which, at low temperatures, show five times greater polarization rotation than in previously reported experiments. In contrast to BIG, the utilized waveguide material EuSe provides a stronger magneto-optical response and also allows much simpler sample fabrication, which paves the way for the creation of sophisticated 2D and 3D magnetoplasmonic metamaterials. Furthermore, it is demonstrated, for the first time, that the dispersion properties of such structures can be exploited to freely tailor the working wavelength within the transparency window of the magneto-optical material. In addition, active magnetic tuning of the polarization rotation is realized. This novel concept for an actively tunable thin film optical rotator with a designated working wavelength could have important applications in highly integrated optical environments.

While the experimental realization and numerical simulation of hybrid magnetoplasmonic systems received considerable attention, an analytical theoretical description hast been missing. In chapter 4, a simple coupled oscillator model is presented, that reveals the underlying physics inside hybrid magnetoplasmonic systems and yields analytical expressions for the resonantly enhanced magneto-optical response. The Lorentz nonreciprocity of the oscillator model is intrinsically incorporated via the Lorentz force, which is proportional to $\mathbf{v} \times \mathbf{B}$. Moreover, the predictions of the model are in good agreement with rigorous numerical solutions of Maxwell's equations for typical sample geometries. The demonstrated ansatz is transferable to other complex and hybrid nanooptical systems and will significantly facilitate device design.

Usually, the maximal MO response of magneto-plasmonic systems is limited by the low Q factor of the plasmon resonances of the grating. This limitation is lifted elegantly by a novel approach presented in chapter 5, which is based on a classical optical analog of electromagnetically induced absorption (EIA) [51, 52]. Here, a strongly damped plasmon oscillation is weakly coupled to a narrow linewidth waveguide resonance with a phase delay, leading to constructive interference. By tuning this coupling carefully, a high-Q absorptive hybrid mode is realized, which can be used to resonantly amplify the Faraday rotation response. Furthermore, the EIA mechanism allows to utilize the large oscillator strength of the plasmonic resonance, leading to an efficient coupling of the incident light into the structure without reducing the effective Q factor due to the broad plasmonic resonance as was the case in previous approaches [45, 47, 53]. Although less than 200 nm thick, at low temperatures, the novel EuS-Au structure design exhibits Faraday rotation of 14°. This is an order of magnitude improvement over previous approaches which only resulted in fractions of degree rotation [35–37, 46, 47]. Furthermore, for low magnetic fields, the presented technique still yields rotation angles that were only achievable with 20 times stronger field strength in previous approaches [53]. The performance of the thin film structure is only a factor of 3 away from the 45°, which are required for building a Faraday isolator. Such devices usually require MO media with a thickness on the order of centimeters. As such, the demonstrated concept could lead to highly integrated, nonreciprocal photonic devices for optical isolation, light modulation and optical magnetic field sensing.

2 FUNDAMENTALS

This chapter provides a basic discussion of the physical phenomena utilized in the following chapters such as magneto-optic effects, plasmonics, and the modal dispersion of grating-waveguide structures. Furthermore, the experimental techniques for measuring Faraday rotation of nanostructures at low temperatures is discussed.

2.1 POLARIZATION OF LIGHT

At first, the mathematical foundation and nomenclature for describing the polarization state of classical electromagnetic waves is introduced. The relations compiled in this section are the basis for the discussions throughout this dissertation. The derivations and naming conventions in this section are adapted from Zvezdin and Kotov [54].

A plane electromagnetic wave propagating in z-direction can be written in the form

$$\mathbf{E}(z,t) = \begin{bmatrix} a\cos(kz-\omega t) \\ b\cos(kz-\omega t+\delta) \end{bmatrix}, \tag{2.1}$$

where ω is the angular frequency and k the wave number [54]. As an alternative formulation to (2.1) it is often more convenient to use a notation which is based on the assumption that the actual physical electric field is given by the real part of the complex electric field

$$\mathbf{E}(z,t) = \tilde{\mathbf{E}} e^{i(kz-\omega t)} \tag{2.2}$$

with

$$\tilde{\mathbf{E}} = \begin{bmatrix} E_x \\ E_y \end{bmatrix} = \begin{bmatrix} a \\ be^{i\delta} \end{bmatrix}. \tag{2.3}$$

As in the definition of the real electric field (2.1), the amplitudes a and b, as well as the phase angle δ are assumed to be real. It is immediately clear that the real part of $\mathbf{E}(z,t)$ in (2.2) is equal to $\mathbf{E}(z,t)$ in (2.1).

The electromagnetic wave described by the general expressions (2.2) and (2.3) can be interpreted as the superposition of two waves, where one is oscillating only in x direction and the other in y direction. However, depending on the phase δ between the two partial waves, the resulting field vector (2.2) performs an elliptical movement. This is illustrated by figure 2.1. It shows a parametric plot of the real part of the electric field, where the varied parameter is the propagator term $\omega t - kz$. The resulting shape is an ellipse, which is fully characterized by the two angles θ and ψ. While θ determines the *tilt* of the polarization ellipse with respect to the x-axis, the angle ψ describes the degree of *ellipticity*. If $\psi = 0$, the wave is linearly polarized, whereas for $|\psi| = \pi$ the wave is circularly polarized. Furthermore, the handedness of the circular polarization can be expressed via die sign of ψ, i.e., $\psi = +(-)\pi$ corresponds to right(left)-handed circular polarization. The two angles are related to the coefficients in (2.1) in the following way [54]:

$$\tan(2\theta) = \frac{2\,\mathrm{Re}(\chi)}{1 - |\chi|^2} \tag{2.4a}$$

$$\tan(2\psi) = \frac{2\,\mathrm{Im}(\chi)}{1 - |\chi|^2} \tag{2.4b}$$

with

$$\chi \equiv \frac{E_y}{E_x} = \frac{be^{i\delta}}{a}. \tag{2.5}$$

For the important case of $|\chi| \ll 1$ the equations (2.4) become

$$\theta \approx \mathrm{Re}(\chi) \tag{2.6a}$$

$$\psi \approx \mathrm{Im}(\chi). \tag{2.6b}$$

While θ and ψ fully determine the polarization state of a plane wave they are not directly accessible in experiment. The reason

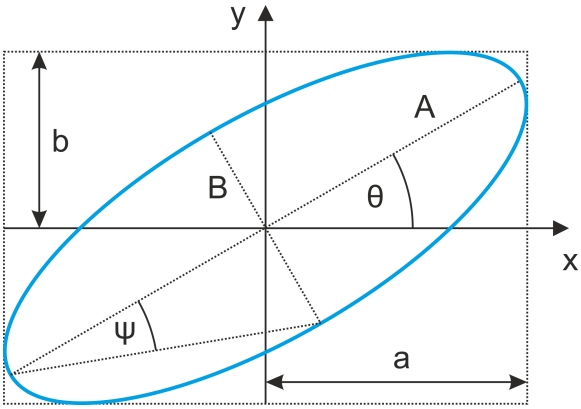

Figure 2.1: Polarization ellipse of a plane electromagnetic wave with a tilting angle θ and ellipticity angle ψ.

is that the electric and magnetic fields of a light wave usually cannot be measured directly and have to be derived from time-averaged intensity measurements. For that reason, the *Stokes formalism* is an important alternative description of polarization states as it is only based on time-averaged intensities. In this formalism the polarization state of light can be expressed by means of the four Stokes parameters [54, 55]

$$S_0 = I_x + I_y \tag{2.7a}$$
$$S_1 = I_x - I_y \tag{2.7b}$$
$$S_2 = I_{+45^\circ} + I_{-45^\circ} \tag{2.7c}$$
$$S_3 = I_R + I_L. \tag{2.7d}$$

The quantities I_x and I_y correspond to the time averaged Intensity of the x- and y-polarized components of the light. Furthermore, I_{+45° and I_{-45° denote the time averaged Intensity measured after the light passes a perfect polarizer tilted by $+45^\circ$ and -45° respectively. Similarly, I_R and I_L are the time-averaged intensities of the right-handed and left-handed components of the plane

wave. The time-averaged description of the Stokes formalism also allows to take the degree of polarization

$$\Pi = \frac{\sqrt{S_1^2 + S_2^2 + S_3^2}}{S_0} \quad (0 \leq \Pi \leq 1) \tag{2.8}$$

into account. Since every plane wave of the form (2.1) has a well defined polarization state, the degree of polarization is $\Pi = 1$. On the other hand, in the case of unpolarized light, the measurement of the Stokes parameters would lead to $\Pi = 0$. This is the typical situation for incoherent light emitted by thermal light sources with rapidly and randomly changing field amplitude vectors. If the degree of polarization is in between the two extremes, the light is partially polarized.

In the case of $\Pi = 1$, the Stokes parameters can be related to the quantities in equation (2.1) in the following way:

$$S_0 = a^2 + b^2 \quad = \sqrt{S_1^2 + S_2^2 + S_3^2} \tag{2.9a}$$

$$S_1 = a^2 - b^2 \quad = S_0 \cos(2\psi)\cos(2\theta) \tag{2.9b}$$

$$S_2 = 2ab\cos\delta = S_0 \cos(2\psi)\sin(2\theta) \tag{2.9c}$$

$$S_3 = 2ab\sin\delta \; = S_0 \sin(2\psi). \tag{2.9d}$$

Dividing equation (2.9c) by (2.9b) and equation (2.9d) by (2.9a) yields the angles

$$\theta = \frac{1}{2}\arctan\left(\frac{S_2}{S_1}\right) \tag{2.10a}$$

$$\psi = \frac{1}{2}\arcsin\left(\frac{S_3}{S_0}\right). \tag{2.10b}$$

In the case of a complex electric field, the Stokes parameters can be derived using

$$S_0 = E_x E_x^* + E_y E_y^* \tag{2.11a}$$

$$S_1 = E_x E_x^* - E_y E_y^* \tag{2.11b}$$

$$S_2 = E_x E_y^* + E_x^* E_y \tag{2.11c}$$

$$S_3 = i(E_x E_y^* - E_x^* E_y). \tag{2.11d}$$

2.2 LIGHT PROPAGATION IN MAGNETO-OPTIC MATERIALS

The characteristic property of magneto-optic (MO) materials is that their associated permittivity tensor possesses magnetic field induced off-diagonal elements which are antisymmetric. In this section it will be elaborated on how this characteristic structure of the permittivity tensor influences the propagation of light inside magneto-optic materials. The most important outcome of this section is that the *Faraday effect* is directly proportional to the off-diagonal elements in the permittivity tensor.

A key element of the following discussions is the Helmholtz wave equation, which describes the evolution of an electromagnetic wave inside a medium with a given permittivity tensor. At first, this relation is derived from the macroscopic Maxwell equations in matter and then applied to both anisotropic and isotropic MO materials. The derivations in this section are based on the works by Jackson [56], Yariv [57], as well as by Zvezdin and Kotov [54].

2.2.1 *Wave equation*

Electromagnetic fields in a medium can be described by the macroscopic Maxwell equations

$$\boldsymbol{\nabla} \times \mathbf{E} + \frac{\partial \mathbf{B}}{\partial t} = 0 \tag{2.12a}$$

$$\boldsymbol{\nabla} \times \mathbf{H} - \frac{\partial \mathbf{D}}{\partial t} = \mathbf{J} \tag{2.12b}$$

$$\boldsymbol{\nabla} \cdot \mathbf{B} = 0 \tag{2.12c}$$

$$\boldsymbol{\nabla} \cdot \mathbf{D} = \rho \tag{2.12d}$$

together with the constitutive equations

$$\mathbf{D} = \varepsilon_0 \mathbf{E} + \mathbf{P} \tag{2.13a}$$

$$\mathbf{H} = \frac{1}{\mu_0} \mathbf{B} - \mathbf{M}. \tag{2.13b}$$

In the following, it is assumed that no sources are present, i.e., $\mathbf{J} = 0$ and $\rho = 0$. Furthermore, the time-harmonic ansatz

$$\mathbf{\Psi}(\mathbf{r}, t) = \mathbf{\Psi}(\mathbf{r}) e^{-i\omega t} \qquad (\mathbf{\Psi} = \mathbf{E}, \mathbf{B}, \mathbf{D}, \mathbf{H}) \tag{2.14}$$

turns the equations (2.12) and (2.13) into

$$\boldsymbol{\nabla} \times \mathbf{E}(\mathbf{r}) - i\omega \mathbf{B}(\mathbf{r}) = 0 \tag{2.15a}$$
$$\boldsymbol{\nabla} \times \mathbf{H}(\mathbf{r}) + i\omega \mathbf{D}(\mathbf{r}) = 0 \tag{2.15b}$$
$$\boldsymbol{\nabla} \cdot \mathbf{B}(\mathbf{r}) = 0 \tag{2.15c}$$
$$\boldsymbol{\nabla} \cdot \mathbf{D}(\mathbf{r}) = 0 \tag{2.15d}$$

and

$$\mathbf{D}(\mathbf{r}) = \varepsilon_0 \varepsilon(\omega) \mathbf{E}(\mathbf{r}) \tag{2.16a}$$
$$\mathbf{B}(\mathbf{r}) = \mu_0 \mu(\omega) \mathbf{H}(\mathbf{r}). \tag{2.16b}$$

In general, both the relative permittivity $\varepsilon(\omega)$ and the relative permeability $\mu(\omega)$ are tensorial quantities and frequency dependent. However, at optical frequencies we can assume that $\mu = 1$ [58]. By applying the operator $\boldsymbol{\nabla}\times$ to equation (2.15a) and by using the relations $\boldsymbol{\nabla} \times (\boldsymbol{\nabla} \times \mathbf{E}) = \boldsymbol{\nabla}(\boldsymbol{\nabla} \cdot \mathbf{E}) - \boldsymbol{\Delta}\mathbf{E}$ and (2.15d), the Helmholtz wave equation

$$\boldsymbol{\Delta}\mathbf{E}(\mathbf{r}) + \frac{\omega^2}{c_0^2} \varepsilon(\omega) \mathbf{E}(\mathbf{r}) = 0 \tag{2.17}$$

is obtained. This differential equation describes the evolution of an electromagnetic wave inside a medium with a given dielectric tensor $\varepsilon(\omega)$.

2.2.2 *Propagation in anisotropic media*

The effect of a static magnetic field on a MO material can be expressed by means of the dielectric tensor of the material. In the following we consider an anisotropic MO material with an applied static magnetic field $\mathbf{B}$ pointing in z direction. Furthermore,

we assume that the principal dielectric axes of the material are $\mathbf{e}_x$, $\mathbf{e}_y$ and $\mathbf{e}_z$. In this case, the dielectric tensor takes the form

$$\varepsilon = \begin{pmatrix} \varepsilon_x & +ig(B) & 0 \\ -ig(B) & \varepsilon_y & 0 \\ 0 & 0 & \varepsilon_z \end{pmatrix}. \tag{2.18}$$

The magnetic-field induced off-diagonal elements of ε are the characterizing property of MO materials and the origin for all MO effects, such as the Faraday effect or the MO Kerr effect. The quantity g is often referred to as *gyration coefficient*. For small magnetic fields the gyration coefficient is usually proportional to B, whereas for larger magnetic fields saturation sets in. This is also the case for the materials EuSe and EuS, which are utilized in the MO nanostructures presented in later chapters.

To solve the wave equation (2.17) we make the ansatz for a plane wave propagating in z-direction:

$$\mathbf{E}(\mathbf{r}) = \tilde{\mathbf{E}} e^{ikz}. \tag{2.19}$$

Since we can assume that the amplitude vector $\tilde{\mathbf{E}}$ lies within the xy plane, we omit its z component in the following derivations. Hence, we can reduce the permittivity tensor to

$$\varepsilon = \begin{pmatrix} \varepsilon_x & +ig \\ -ig & \varepsilon_y \end{pmatrix}. \tag{2.20}$$

Inserting (2.19) and (2.20) into the wave equation (2.17) leads to the eigenvalue problem

$$\varepsilon \tilde{\mathbf{E}} = \lambda \tilde{\mathbf{E}} \tag{2.21}$$

with

$$\lambda = k^2 \frac{c_0^2}{\omega^2}. \tag{2.22}$$

Solving the eigenvalue problem yields the eigenvalues

$$\lambda_{1,2} = \frac{\varepsilon_x + \varepsilon_y}{2} \mp \sqrt{g^2 + \frac{(\varepsilon_x - \varepsilon_y)^2}{4}} \tag{2.23}$$

and the eigenvectors

$$\tilde{\mathbf{E}}^{(1,2)} = \begin{bmatrix} \left(\frac{\varepsilon_x - \varepsilon_y}{2} \mp \sqrt{g^2 + \frac{(\varepsilon_x - \varepsilon_y)^2}{4}} \right) \frac{1}{-ig} \\ 1 \end{bmatrix}. \tag{2.24}$$

Consequently, the general solution of (2.17) is then given by the superposition

$$\mathbf{E}(\mathbf{r}) = A\, \tilde{\mathbf{E}}^{(1)} e^{ik_1 z} + B\, \tilde{\mathbf{E}}^{(2)} e^{ik_2 z} \tag{2.25}$$

with

$$k_{1,2} = \frac{\omega}{c_0} \sqrt{\lambda_{1,2}}. \tag{2.26}$$

The coefficients A and B are determined by the initial condition. For example, the case of x-polarized incident light implies that $E_y(z = 0) = 0$ and $B = -A$, which leads to

$$\mathbf{E}(\mathbf{r}) = A \left[\tilde{\mathbf{E}}^{(1)} e^{ik_1 z} - \tilde{\mathbf{E}}^{(2)} e^{ik_2 z} \right]. \tag{2.27}$$

Similarly, y-polarized incident light is described by $E_x(z = 0) = 0$ and implies $B = -A\tilde{E}_x^{(1)} / \tilde{E}_x^{(2)}$. This leads to a wave propatation of the form

$$\mathbf{E}(\mathbf{r}) = A \left[\tilde{\mathbf{E}}^{(1)} e^{ik_1 z} - \frac{\tilde{E}_x^{(1)}}{\tilde{E}_x^{(2)}} \tilde{\mathbf{E}}^{(2)} e^{ik_2 z} \right]. \tag{2.28}$$

In both cases, the coefficient A is an arbitrary normalization parameter depending on the incident intensity. The equations (2.27) and (2.28) are utilized in section 4.1 where the magneto-optical response of hybrid plasmonic nanostructures is described by means of a birefringent effective medium.

2.2.3 *Faraday rotation*

Many bulk magneto-optic materials, such as EuSe and EuS are not birefringent, i.e., the diagonal elements of the dielectric function are equal. In this case, the relative permittivity tensor (2.20) simplifies to

$$\varepsilon(\omega) = \begin{pmatrix} \varepsilon_x & +ig \\ -ig & \varepsilon_x \end{pmatrix} \tag{2.29}$$

and the solution of the eigenvalue problem (2.21) turns into

$$\lambda_{1,2} = \varepsilon_x \pm g \tag{2.30}$$

and

$$\tilde{\mathbf{E}}^{(1,2)} = \begin{pmatrix} \pm i \\ 1 \end{pmatrix}. \tag{2.31}$$

Furthermore, the absolute value of the gyration is typically significantly smaller than the diagonal permittivity, i.e., $|g|/|\varepsilon_x| \ll 1$. In this approximation, we can write the two propagation constants k_1 and k_2 as

$$k_{1,2} = \frac{\omega}{c_0}\sqrt{\varepsilon_x \pm g} \approx \kappa \mp \gamma, \tag{2.32}$$

with

$$\kappa = \frac{\omega}{c_0}\sqrt{\varepsilon_x} \tag{2.33}$$

$$\gamma = -\frac{1}{2}\frac{\omega}{c_0}\frac{g}{\sqrt{\varepsilon_x}}. \tag{2.34}$$

From this, through equation (2.27) for x-polarized incident light, we obtain

$$\mathbf{E}(\mathbf{z}, t) = A e^{i(\kappa z - \omega t)} \left[\begin{pmatrix} +i \\ 1 \end{pmatrix} e^{-i\gamma z} - \begin{pmatrix} -i \\ 1 \end{pmatrix} e^{+i\gamma z} \right]. \tag{2.35}$$

To evaluate how the polarization state of the wave (2.35) evolves, we can apply the relations (2.11) to derive the corresponding Stokes parameters

$$S_0 = +4|A|^2 \cosh\left(2\,\mathrm{Im}\left\{\gamma\right\} z\right) \tag{2.36a}$$

$$S_1 = +4|A|^2 \cos\left(2\,\mathrm{Re}\left\{\gamma\right\} z\right) \tag{2.36b}$$

$$S_2 = -4|A|^2 \sin\left(2\,\mathrm{Re}\left\{\gamma\right\} z\right) \tag{2.36c}$$

$$S_3 = -4|A|^2 \sinh\left(2\,\mathrm{Im}\left\{\gamma\right\} z\right). \tag{2.36d}$$

Furthermore, in the limit of a relatively weak gyration, i.e., for $|\gamma|z \ll 1$, the relations (2.10) and (2.34) yield

$$\theta = \frac{1}{2}\frac{\omega}{c_0}\mathrm{Re}\left\{\frac{g}{\sqrt{\varepsilon_x}}\right\}z \tag{2.37a}$$

$$\psi = \frac{1}{2}\frac{\omega}{c_0}\mathrm{Im}\left\{\frac{g}{\sqrt{\varepsilon_x}}\right\}z. \tag{2.37b}$$

From this we see that in the case of low material losses and a small imaginary part of g, the ellipticity ψ stays small, while the tilting angle θ increases linearly with the propagation distance z. Since the gyration g is proportional to the applied magnetic field B, it is very common to write equation 2.37a in the alternative form

$$\theta = VBz, \tag{2.38}$$

where the proportionality factor V is commonly referred to as *Verdet constant*. However, the term *constant* is a bit misleading, since V is actually frequency dependent. This is immediately clear by considering that equation 2.37a contains both the factor ω and the gyration g, which is also frequency dependent. The magnetic field induced polarization rotation described by the expression 2.38 is called *Farady effect* and it is illustrated by the blue wave in figure 2.2. It is important to realize that the magnetic field induced polarization rotation breaks the *time-reversal symmetry*. The result of this symmetry breaking becomes clear when a mirror is added behind the MO material as indicated in figure 2.2. In relation to the magnetic field vector, the backward propagating orange light wave is rotated in the same direction and by the same angle as the forward propagating blue wave. Hence, the polarization states of the blue and orange waves on the left-hand side are different. Such a nonreciprocal behavior is not found in other linear and static systems [10]. For example, although an optically active medium [4] can also induce a polarization rotation of transmitted light, any back-reflected wave would rotate back to the polarization state of the incoming wave. In other words, in the case of an optically active medium the direction of polarization rotation is determined by the direction of the wave vector,

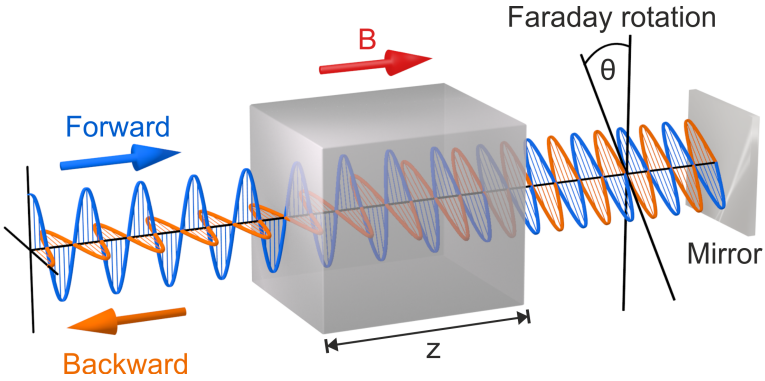

Figure 2.2: Illustration of the Faraday effect for the case of a real gyration g and negligible absorption. When light propagates through a magneto-optical material along the direction of the applied magnetic field (forward direction) the polarization plane gets rotated by the angle θ. Backward propagating light is rotated by the same angle and in the same direction (relative to the magnetic field).

whereas the direction of Faraday rotation is determined by the direction of the magnetic field.

This nonreciprocal nature [3, 59] of the Faraday effect directly leads to its most prominent application, namely optical isolation: If the rotation angle θ is equal to 45°, the polarizations of the forward and backward propagating waves on the left-hand side of figure 2.2 are perpendicular. In this case, the addition of one vertically aligned polarizer on the left-hand side of the MO material and another polarizer, which is tilted by 45°, on the right-hand side of the MO material, allows light to pass the system only in forward direction. Light traveling through the system in backward direction is blocked by the polarizer on the left side.

2.2.4 *Magneto-optic effects in reflection*

The Faraday effect is only one of several phenomena arising from the magnetically induced off-diagonal elements in $\epsilon(\omega)$. For example, also the reflection behavior of a MO material can change

depending on the applied magnetic field. This phenomenon is referred to as magneto-optic Kerr effect (MOKE). Since the MOKE does rely on reflection rather than propagation it cannot only be observed for transparent materials but also for opaque materials such as ferromagnetic metals.

Although the work presented in this dissertation concentrates on the Faraday effect, in the following a brief overview of the different types of the MOKE is given. As illustrated in figure 2.3, the different types are classified depending on the direction of the magnetization in relation to the plane of incidence and the material surface [54]. The black arrows indicate the wavevectors of the incident and reflected light. If the magnetization is perpendicular to the material surface, there occurs a magnetically induced polarization rotation as well as a change in ellipticity of the reflected light. This effect is referred to as the polar MOKE. Similarly, if the magnetization is parallel to the surface the longitudinal MOKE occurs. Here, the magnetization also induces a polarization rotation and an ellipticity change. If the magnetization is perpendicular to the plane of incidence, the intensity of the reflected light changes with the magnitude of magnetization. This phenomenon is called transverse MOKE.

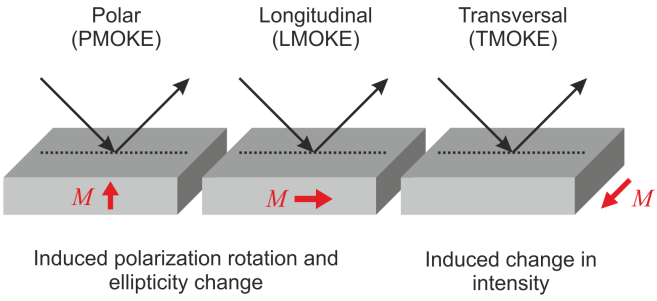

Figure 2.3: Illustration of the different manifestations of the magneto-optic Kerr effect (MOKE). While polar and longitudinal MOKE describe a magnetically induced polarization rotation and ellipticity change, in the case of transversal MOKE a magnetization dependent modulation of the reflected intensity occurs.

Since the polarization rotation of the MOKE only scales with the off-diagonal elements of the permittivity tensor, the MOKE is generally much weaker than the Faraday effect, which also scales with the optical path length through the material. For example, although Fe, Co and Ni possess an extremely large Verdet constant (see section 2.4) the rotation angles arising from the polar MOKE are usually less than 1 deg in the visible [54].

2.3 MICROSCOPIC DESCRIPTION OF THE FARADAY EFFECT

In the section 2.2 it has been shown that the magneto-optic response of a material can be described phenomenologically by the anti-symmetric off-diagonal elements of the material's permittivity tensor. However, the microscopic mechanisms which give rise to these off-diagonal elements were not discussed. In this section the microscopic origin of magneto-optic effects is explained by means of both a classical and a quantum mechanical approach.

2.3.1 *Classical description*

The microscopic origin of the magnetically induced off-diagonal elements in (2.18) can be understood intuitively in the picture of an extended Lorentz oscillator model. This model and the calculations in this section are largely based on the descriptions given in [60–62]. However, the model is presented in a slightly generalized way, which allows a more direct link to the development of the oscillator model of magnetoplasmonics presented in chapter 4. As in the standard version of the Lorentz oscillator model for dielectrics [62], the bound electrons of a solid are treated as classical mechanical oscillators, which are suspended by three springs. This is illustrated by figure 2.4. Furthermore, as each oscillator is assumed to have a charge q, it is driven by the harmonically oscillating electric field $\mathbf{E}(t) = \mathbf{E}\, e^{-i\omega t}$ of the light wave. The mass and the displacement vector of the oscillator are denoted by m and $\mathbf{r} = (x, y, z)^{\mathrm{T}}$ respectively. To account for magneto-optic effects, in the extended version of the model a static magnetic field $\mathbf{B}$ is assumed to be present, which additionally exerts the *Lorentz force*

$$\mathbf{F}_L = q\, \dot{\mathbf{r}} \times \mathbf{B} \tag{2.39}$$

on the oscillators. For the following discussions we assume that the magnetic field points in z direction. In this case, the Lorentz

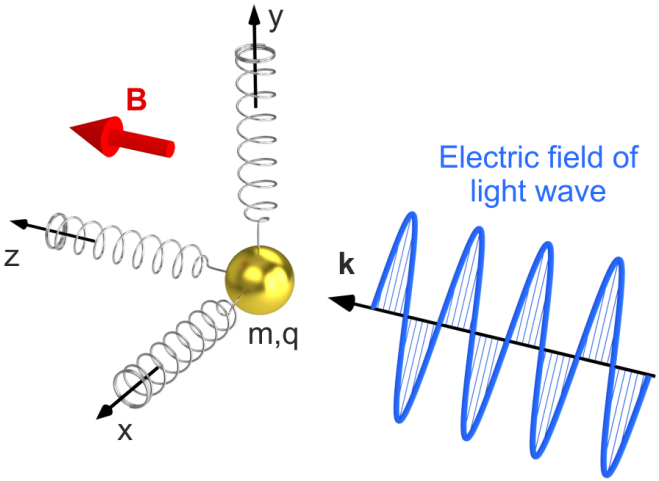

Figure 2.4: Schematic drawing of the mechanical oscillator model for magneto-optic solids. It corresponds to the standard Lorentz oscillator model for dielectrics, but with the addition of a static magnetic field, which exerts a Lorentz force on the bound electrons.

force is given by $\mathbf{F}_L = qB(\dot{y}, -\dot{x}, 0)^{\mathrm{T}}$ and the resulting equations of motion are

$$m\ddot{x} = -d_x x - 2\gamma_x \dot{x} + qB\dot{y} + qE_x \exp(-i\omega t) \tag{2.40a}$$
$$m\ddot{y} = -d_y x - 2\gamma_y \dot{y} - qB\dot{x} + qE_y \exp(-i\omega t) \tag{2.40b}$$
$$m\ddot{z} = -d_z x - 2\gamma_z \dot{z} \qquad + qE_z \exp(-i\omega t)\,. \tag{2.40c}$$

The quantities $\{d_x, d_y, d_z\}$ and $\{\gamma_x, \gamma_y, \gamma_z\}$ denote the stiffness and damping coefficients of the springs. To solve the equations, we start by making a time harmonic ansatz for the oscillator displacement, i.e.,

$$\mathbf{r}(t) = \mathbf{r}_0 \exp(-i\omega t)\,, \tag{2.41}$$

which turns the equations (2.40) into

$$(-\omega^2 + \Omega_x^2 - 2i\Gamma_x\omega)x_0 + i\omega\omega_c y_0 = \frac{q}{m}E_x \tag{2.42a}$$

$$(-\omega^2 + \Omega_y^2 - 2i\Gamma_y\omega)y_0 - i\omega\omega_c x_0 = \frac{q}{m}E_y \tag{2.42b}$$

$$(-\omega^2 + \Omega_z^2 - 2i\Gamma_z\omega)z_0 = \frac{q}{m}E_z, \tag{2.42c}$$

with $\Omega_i^2 = d_i/m$ and $\Gamma_i = \gamma_i/m$ $(i = x, y, z)$ and $\omega_c = qB/m$. The equations (2.42) can be reformulated in the matrix form, which yields

$$M(\omega)\,\mathbf{r}_0 = \frac{q}{m}\,\mathbf{E}, \tag{2.43}$$

with

$$M(\omega) = \begin{pmatrix} M_x & +i\omega\omega_c & 0 \\ -i\omega\omega_c & M_y & 0 \\ 0 & 0 & M_z \end{pmatrix} \tag{2.44}$$

and $M_i(\omega) = -\omega^2 + \Omega_x^2 - 2i\Gamma_x\omega$, $(i = x, y, z)$. Assuming that n is the oscillator density in the medium, we can express the macroscopic electronic polarization as

$$\mathbf{P} = nq\mathbf{r}_0 = \frac{nq^2}{m}M^{-1}\mathbf{E}. \tag{2.45}$$

Furthermore, the comparison with

$$\mathbf{P} = \varepsilon_0\chi\mathbf{E} \tag{2.46}$$

allows to identify the electronic susceptibility

$$\chi(\omega) = \omega_q^2 M(\omega)^{-1}, \tag{2.47}$$

with

$$\omega_q = \sqrt{\frac{nq^2}{\varepsilon_0 m}}. \tag{2.48}$$

The optical response of a material is usually expressed by the electric permittivity tensor $\varepsilon = I + \chi$, where I denotes the identity

matrix $\mathrm{diag}(1,1,1)$. To also account for a (scalar) background susceptibility due to other off-resonant electronic polarizations [62], we write the permittivity in the more general form $\varepsilon = \varepsilon_\infty I + \chi$, where ε_∞ corresponds to the value of the diagonal permittivity elements for infinite frequency. With that, we arrive at

$$\varepsilon(\omega) = I\varepsilon_\infty + \omega_q^2 M(\omega)^{-1}. \tag{2.49}$$

In the anisotropic case, i.e., when the stiffness and damping coefficients of all oscillators are different, the inverse of $M(\omega)$ and thus also the permittivity tensor $\varepsilon(\omega)$ exhibit a very complicated ω dependence. However, many magneto-optical materials are isotropic, that is, $\Omega_x = \Omega_y = \Omega_z = \Omega$ and $\Gamma_x = \Gamma_y = \Gamma_z = \Gamma$. In this case we obtain

$$\varepsilon = \begin{pmatrix} \varepsilon_{11} & \varepsilon_{12} & 0 \\ \varepsilon_{21} & \varepsilon_{22} & 0 \\ 0 & 0 & \varepsilon_{33} \end{pmatrix} \tag{2.50}$$

with

$$\varepsilon_{11} = \quad \varepsilon_{22} = \frac{\omega_q^2(-\omega^2 + \Omega^2 - 2i\Gamma\omega)}{(-\omega^2 + \Omega^2 - 2i\Gamma\omega)^2 - \omega^2\omega_c^2} + \varepsilon_\infty \tag{2.51a}$$

$$\varepsilon_{12} = -\varepsilon_{21} = \frac{-i\omega\omega_c\omega_q^2}{(-\omega^2 + \Omega^2 - 2i\Gamma\omega)^2 - \omega^2\omega_c^2} \tag{2.51b}$$

$$\varepsilon_{33} = \frac{\omega_q^2}{-\omega^2 + \Omega^2 - 2i\Gamma\omega} + \varepsilon_\infty. \tag{2.51c}$$

From the equations (2.51) we can see that the magnetic field not only influences the off-diagonal elements of the dielectric function but also the diagonal elements, which can be regarded as the classical manifestation of the *Zeeman effect* [61]: In the case of low damping (Γ is small), the resonance condition for ε_{11} is given by

$$\omega \approx \Omega \pm \frac{\omega_c}{2}, \tag{2.52}$$

which means that the material resonance is split by the magnetic field.

However, in most magneto-optical applications, the influence of the magnetic field on the diagonal components can be neglected, since usually $|\omega_c| \ll \omega, \Omega, \Gamma$. In this approximation the components of ε reduce to

$$\varepsilon_{11} = \varepsilon_{22} = \varepsilon_{33} \quad = \frac{\omega_q^2}{-\omega^2 + \Omega^2 - 2i\Gamma\omega} + \varepsilon_\infty \tag{2.53a}$$

$$\varepsilon_{12} = -\varepsilon_{21} = \frac{-i\omega\omega_c\omega_q^2}{(-\omega^2 + \Omega^2 - 2i\Gamma\omega)^2}. \tag{2.53b}$$

The model function (2.53) provides a very good qualitative description of the magneto-optic response of many materials. There are several important properties of the model: Firstly, since ω_c is proportional to the magnetic field, the model correctly predicts a linear relation between the off-diagonal elements of the permittivity and the magnetic field. In the regime of weak magnetic fields, this is the case for most magneto-optic materials. Furthermore, the model provides a Kramers-Kronig-consistent relation between the real and imaginary part of ε_{12} [54].

The permittivity function can be easily implemented in many numerical simulation tools. However, to obtain quantitatively correct simulation results, the free model parameters in the relations (2.53) have to be fitted to measurement data. For some MO materials it can be necessary to add further oscillators to the polarization (2.45) with different individual parameter sets, in order to account for a more complex MO behavior.

2.3.2 *Quantum mechanical description*

Compared to the simple mechanical model provided in section 2.3.1 the advantage of the following quantum mechanical description is that it can explain different dispersion behaviors of the magneto-optic spectra (i.e., diamagnetic and paramagnetic lineshapes) as well as the influence of temperature on the magnitude of the Faraday rotation. The following discussion is derived from references [54] and [63].

To understand the origin of Faraday rotation in atomic systems, we will make use of the fact that Faraday rotation can be regarded as a manifestation of magnetic circular dichroism (MCD), i.e., different absorption of right-handed circularly polarized (RCP) and left-handed circularly polarized (LCP) light [54]. The reason is that it is much simpler to relate atomic properties to MCD than to the Faraday effect directly. We note in passing, that, as in the case of optical activity [4, 64], polarization rotation and circular dichroism are connected via Kramers-Kronig relations [54].

In magneto-optics it is common to distinguish two contributions to MCD: Firstly, due to the Zeeman effect, atomic levels are split into several levels that can be excited only with light of the correct handedness. This results in absorption maxima of LCP and RCP light which are slightly split in energy. As a consequence, the absorption of LCP and RCP is different for most wavelengths. This mechanism is referred to as *diamagnetic* Faraday rotation, as it often occurs in diamagnetic materials. The second mechanism contributing to MCD usually (if present) exceeds the diamagnetic contribution: Due to temperature or other influences, the effective oscillator strength of either the LCP or RCP transition can be suppressed. This can dramatically increase the absorption difference of LCP and RCP and thus the Faraday rotation. This mechanism is called *paramagnetic* Faraday rotation as paramagnetic materials often exhibit such a behavior. At this point it should be emphasized that the terms diamagnetic and paramagnetic are not related to the magnetic susceptibility but are part of an established naming scheme for classifying the dispersion in magneto-optical spectra [54].

A more detailed comparison between the diamagnetic and paramagnetic mechanisms is illustrated in the figures 2.5a and 2.5b respectively. In the diamagnetic case the ellipticity spectrum is S-shaped (orange line) whereas the Faraday rotation shows a peak surrounded by two smaller negative peaks (blue line). This behavior is very similar to chiral media [64]. The lower part of figure 2.5a shows an exemplary and idealized energy level scheme which would result in such a magneto-optic

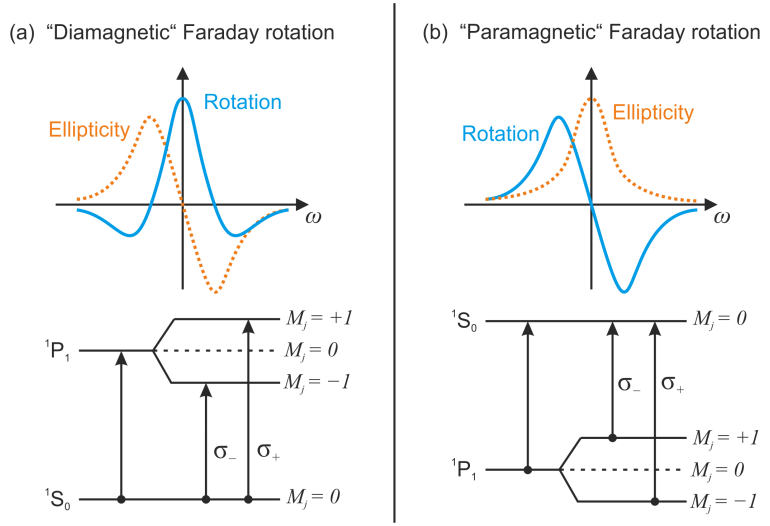

Figure 2.5: Comparison of the diamagnetic and paramagnetic Faraday rotation mechanisms. The line shapes of Faraday rotation and ellipticity are drawn schematically.

dispersion. In this example we consider a transition from a $^1S_0$ state to a $^1P_1$ state. Due to the magnetic field the $^1P_1$ state is split into three states with quantum numbers $M_J = 0, +1, -1$. An incoming LCP or RCP photon induces a transition with $\Delta M = +1$ or $\Delta M = -1$ respectively. Due to the magnetic splitting, the absorption lines of the LCP and RCP transitions (denoted by σ_+ and σ_-) are shifted in energy. Thus, the absorption for LCP and RCP light is different for most wavelengths and results in the depicted Faraday rotation dispersion. We note that this is in fact the dispersion behavior as predicted by the mechanical oscillator description in section 2.3.1.

A different behavior can be observed in the paramagnetic case, which is schematically depicted in figure 2.5b. This situation arises when the oscillator strengths of the LCP and RCP transitions is significantly different. To illustrate this, in the lower part of figure 2.5b an idealized energy level diagram is depicted. The transition energies and the magnetic field induced splitting are

assumed to be the same as in the diamagnetic example. Hence, there should also be a diamagnetic contribution to the Faraday rotation spectrum with the same magnitude. However, here the usually much stronger paramagnetic mechanism dominates the magneto-optical spectra: For $T \to 0$ the population probability of the ($M_J = -1$) level is much higher than for the ($M_J = +1$) level resulting in a magnetization. Therefore, the σ_+ transition dominates. This difference in oscillator strength is responsible for the paramagnetic Faraday rotation dispersion.

Influence of spin-orbit coupling

The absolute magnitude of the magneto-optical response depends on the specific atomic structure of the atoms in the medium. In the case of solids, the resulting band structure is critical. There are many factors that contribute to a strong magneto-optic response and also to a dispersion behavior deviating from the two idealized cases discussed above. This includes spin-orbit interactions, exchange interactions, and further effects. A more detailed compilation of possible influences is left to specialized literature, such as [54, 63, 65, 66]. However, in the following it is motivated why spin-orbit interaction is one of the most important ingredients for a large Faraday rotation response (as in the case of Eu compounds).

To understand the influence of spin-orbit coupling, we consider the exemplary dipole transitions depicted in figure 2.6. The diagram shows transitions from a $^2S_{1/2}$ state to ^2P states. Due to the spin-orbit interaction the ^2P state is split into the two levels $^2P_{1/2}$ ($J = 1/2$) and $^2P_{3/2}$ ($J = 3/2$). The presence of a magnetic field lifts the degeneracy of levels with the same total angular momentum. The arrows indicate the dipole allowed transitions which fulfill the selection rule $\Delta M_j = \pm 1$. It can be shown [54]

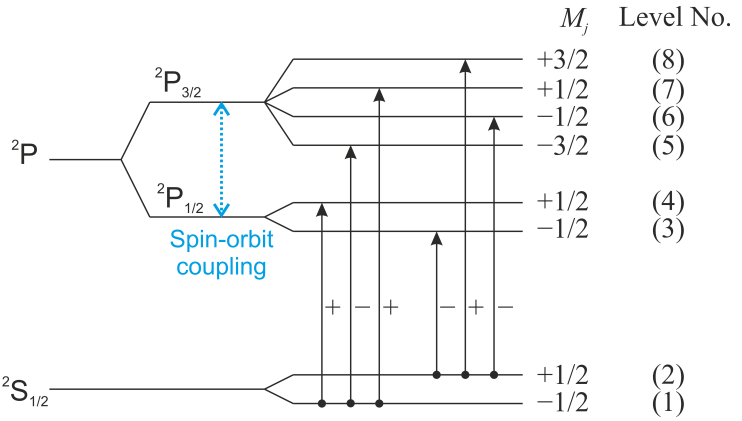

Figure 2.6: Schematic diagram of electric dipole transitions to illustrate that a large spin-orbit coupling can contribute to strong Faraday rotation.

that the non-zero transition dipole moments $d^{\pm}_{ab}$ fulfill the relations

$$|d^{+}_{14}|^2 = |d^{-}_{23}|^2 = (2/9)d^2 \tag{2.54}$$

$$|d^{-}_{15}|^2 = |d^{+}_{28}|^2 = (1/3)d^2 \tag{2.55}$$

$$|d^{+}_{17}|^2 = |d^{-}_{26}|^2 = (1/9)d^2, \tag{2.56}$$

where d is constant. For $T \to 0$ only level 1 is populated and only the transitions to the levels 4, 5 and 7 are possible. Neglecting the difference in transition frequency, their contribution to MCD (and thus Faraday rotation) would cancel out, since from equation (2.54) follows $|d^{+}_{14}|^2 - |d^{-}_{15}|^2 + |d^{+}_{17}|^2 = 0$. This means that the Faraday rotation occurs only due to the different transition frequencies, as it was the case in the diamagnetic mechanism discussed above. It can be seen directly from figure 2.6 that, with increasing spin-orbit splitting, the difference in the transition frequencies become larger and thus the overall Faraday rotation becomes larger. When the temperature increases, the population of level 2 starts to grow and also contributes to the Faraday rotation. In the high temperature limit, the populations of level 1 and 2 are the same and it can be shown that the overall contribution

to the Faraday rotation by the transitions from level 2 is of the same magnitude as the contribution by the transitions from level 1, yet with opposite sign [54]. More precisely, the Faraday rotation is proportional to the population difference between level 1 and 2, i.e., to the average magnetic moment of the atom or ion (as in the discussion of the paramagnetic mechanism). In summary, we have seen that Faraday rotation tends to decrease with higher temperatures (and lower average magnetic moment) and strong spin-orbit interaction can be beneficial for large rotation angles.

2.4 COMPARISON OF TYPICAL MAGNETO-OPTIC MATERIALS

Materials with a particularly strong magneto-optic response are usually referred to as magneto-optic (MO) materials. The general properties of these materials differ strongly, not only with respect to the magnitude of the MO response, but also in many other aspects. For example, there are metallic as well as non-metallic MO materials, magnetic MO materials with different magnetic susceptibility, as well as transparent and opaque materials (depending on wavelength). Furthermore, the MO properties usually strongly depend on temperature. In this section, some of the most relevant MO materials are compared. However, it should be mentioned that the collection of materials provided here is not complete, especially because there are many doped variants of the listed materials as well as materials with slightly modified chemical composition. An extended overview can be found in more specialized literature [54, 63, 66–70].

Figure 2.7 gives a rough overview of the range of available MO materials and the magnitude of the achievable MO response in terms of Faraday rotation per unit length. The data was extracted from reference [65]. The graph shows that the materials with the largest specific Faraday rotation response are ferromagnetic metals such as Fe, Co and Ni. Also quite strong Faraday rotation can be achieved by using Europium compounds at low temperatures such as EuSe or by CrI_3, $CrBr_3$ and MnBi. EuS, EuTe and EuO are not shown in the diagram but exhibit optical and MO properties similar to EuSe [63, 68]. Relatively weak Faraday rotation is obtained by yttrium-iron-garnet (YIG) as well as by $CrCl_3$ at shorter wavelengths. We should note at this point that although the spectrum of YIG is plotted for low temperatures [65] the material also exhibits Faraday rotation of comparable magnitude at room temperature [71].

In many cases the specific Faraday rotation is not a suitable figure of merit for the performance of a MO material. Especially, when a MO material is to be used in transmission geometry, the absorption of the material is relevant. Thus, a more useful way

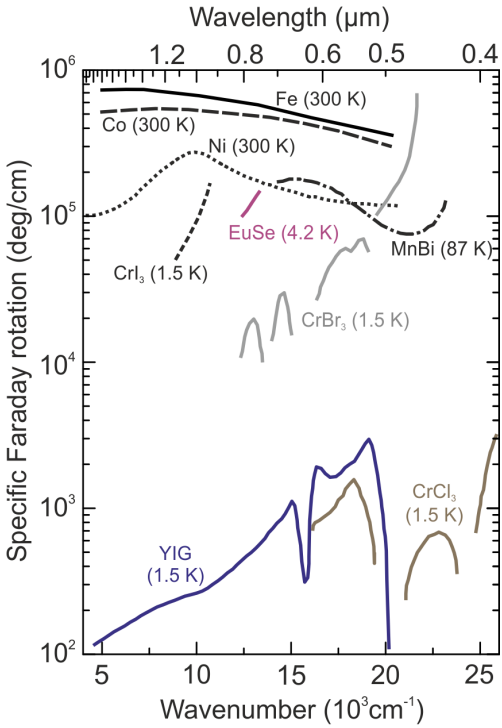

Figure 2.7: Faraday rotation per unit length for different magneto-optic materials. The data were extracted from reference [65].

to characterize MO materials can be the specific Faraday rotation normalized to attenuation (in dB/cm) shown in figure 2.8 (data from reference [65]). This graph reveals that ferromagnetic metals, which show by far the largest MO response, also show the largest optical losses. Although their room temperature compatibility is convenient, their opacity makes them only useful for MO effects in reflection geometry (e.g., for the MO Kerr effect). In contrast, EuSe exhibits both high MO response and high transparency. This is also the case for other Eu compounds such as EuS, EuTe, and EuO, which are not plotted here [63, 68]. Although the ratio of Faraday rotation and attenuation can be a

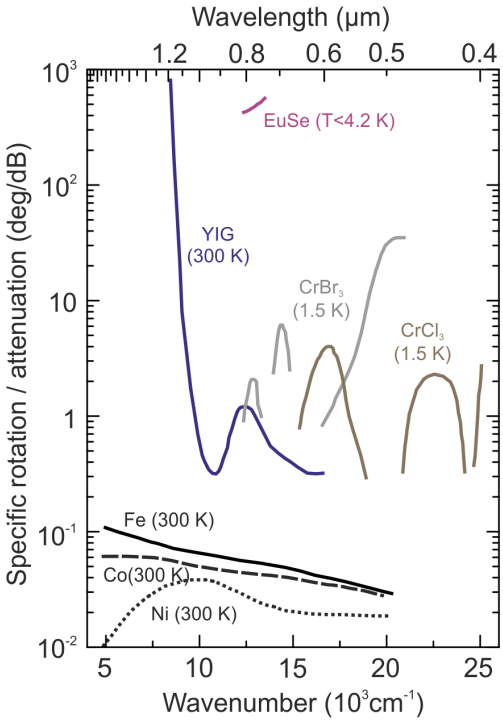

Figure 2.8: Faraday rotation normalized to attenuation in dB for different magneto-optic materials. The data were extracted from reference [65].

meaningful quantity, it should not be regarded as an universal figure of merit for MO applications. For example, in the near IR YIG exhibits a very high ratio of Faraday rotation and attenuation. However, the absolute Faraday rotation in this frequency region is extremely weak (see figure 2.7). This means that a polarization rotation device made of YIG would require a relatively large amount of MO material in order to achieve a sizable rotation angle. Hence, for realizing a small scale Faraday rotator, an Eu compound would be more suitable, yet at lower temperatures.

In state of the art nanoscale MO systems, there are three predominant groups of utilized MO materials: Metals [32, 41–44], iron garnets [26, 45–47] and Eu compounds (chapters 3 and 5).

Due to the high optical losses of metals, the first group is mainly used for systems that operate in reflection geometry (i.e., for utilizing the MO Kerr effect). In the following, we focus on the comparison between iron garnets and Eu compounds, which are suitable for the utilization in Faraday geometry.

Since garnets possess a relatively low Verdet constant, there have been efforts to modify their chemical structure in order to enhance their MO response. For example, in the case of YIG, substituting yttrium with bismuth leads to a greatly increased Faraday effect [70]. However, the relatively large Faraday rotation of bismuth-iron-garnet (BIG) comes with significant fabrication difficulties: BIG only forms in sophisticated non-equilibrium processes, which involve pulsed laser deposition as well as a subsequent high temperature annealing. This makes the fabrication of hybrid systems incorporating plasmonic nanostructures very challenging and restricts the number of possible structure geometries considerably. For example, any gold nanostructures that are incorporated inside a BIG film would get damaged due to the high temperatures. Moreover, BIG only grows on garnet substrates or special buffer layers.

Eu compounds such as EuSe and EuS provide very simple fabrication by physical vapor deposition and are also compatible with standard electron beam lithography processes. As such, these materials can be used to realize sophisticated layer based nanostructure geometries consisting of both magneto-optic an plasmonic materials. EuSe and EuS possess very strong MO response below and around their Curie temperatures at 7 K and 16.6 K, respectively.

2.5 PLASMONICS

In this section the basic optical properties of metal interfaces and nanostructures are summarized. This allows us to understand the emergence of localized surface plasmon resonances in gold nanostructures as used in the following chapters. It will turn that plasmonic resonances are of fundamental importance for tailoring the dispersion properties of hybrid magnetoplasmonic systems.

This section begins with a discussion of the general optical properties of metals based on the plasma model (also known as Drude model). This is the foundation for the subsequent analysis of the two most prominent plasmonic phenomena: Surface plasmon polaritons and localized surface plasmon resonances. As this section cannot provide full coverage of all aspects of plasmonics and related electrodynamic effects, the interested reader can find very detailed further discussions in the works [56, 72], which this section is based on.

2.5.1 *The dielectric function of metals*

The characterizing optical properties of metals can be derived from the *plasma model*, also known as the *Drude model*. For many metals the validity of this simple model extends over a surprisingly wide wavelength range. The basic assumption of the model is that the unbound electrons with number density n are moving freely against the fixed and positively charged ions. This means that the electrons are not subjected to a restoring force as in the Lorentz oscillator model discussed in section 2.3.1. However, as in the Lorentz model, the electrons are assumed to be driven by the time harmonic electric field $\mathbf{E}(t) = \mathbf{E}_0 e^{-i\omega t}$ of the light wave. The resulting equation of motion for the electron displacement $\mathbf{x}(t)$ is given by

$$m\ddot{\mathbf{x}}(t) + m\gamma\dot{\mathbf{x}}(t) = -e_0\mathbf{E}_0 e^{-i\omega t}, \tag{2.57}$$

where m and $-e_0$ are the effective mass and charge of an individual electron. Furthermore, the damping constant $\gamma = 1/\tau$ corresponds to the characteristic collision frequency of a plasma electron. The differential equation (2.57) can be solved by the time harmonic ansatz

$$\mathbf{x}(t) = \mathbf{x}_0 e^{-i\omega t}, \tag{2.58}$$

which leads to the solution

$$\mathbf{x}(t) = \frac{e_0}{m(\omega^2 + i\gamma\omega)}\mathbf{E}(t). \tag{2.59}$$

Furthermore, by means of equation (2.59), the macroscopic polarization of the plasma $\mathbf{P} = -ne_0\mathbf{x}$ can be written as

$$\mathbf{P} = \frac{-ne_0^2}{m(\omega^2 + i\gamma\omega)}\mathbf{E}. \tag{2.60}$$

With equation (2.60) we have now established the relation between the polarization of the plasma and the applied electric field. Hence, via the relation $\mathbf{P} = \varepsilon_0\chi(\omega)\mathbf{E}$, the electric susceptibility $\chi(\omega)$ can be identified as

$$\chi(\omega) = \frac{-ne_0^2}{m\varepsilon_0(\omega^2 + i\gamma\omega)}. \tag{2.61}$$

Finally, by introducing the *plasma frequency* ω_p

$$\omega_p = \frac{ne_0^2}{m\varepsilon_0} \tag{2.62}$$

and by using $\varepsilon(\omega) = 1 - \chi(\omega)$, the complex dielectric function of the free electron gas can be written as

$$\varepsilon(\omega) = 1 - \frac{\omega_p^2}{\omega^2 + i\gamma\omega}. \tag{2.63}$$

The real and imaginary parts of $\varepsilon(\omega)$ are given by

$$\mathrm{Re}\left[\varepsilon(\omega)\right] = 1 - \frac{\omega_p^2\tau^2}{1 + \omega^2\tau^2} \tag{2.64}$$

$$\mathrm{Im}\left[\varepsilon(\omega)\right] = \frac{\omega_p^2\tau}{\omega + \omega^3\tau^2}. \tag{2.65}$$

In order to increase the agreement between the modeled permittivity (2.63) and the one of real metals, it can be useful to introduce a slight modification. By adding a constant parameter to the expression (2.63), the contribution of the positive metal ions to the overall polarization can be taken into account [72]. With this modification, the dielectric function becomes

$$\varepsilon(\omega) = \varepsilon_\infty - \frac{\omega_p^2}{\omega^2 + i\gamma\omega}, \tag{2.66}$$

where ε_∞ is the permittivity at infinite frequency. Before the behavior of this model function is discussed in further detail, the role of the plasma frequency ω_p should be clarified.

Plasma frequency and volume plasmons

In order to understand the physical meaning of the plasma frequency ω_p, we now consider a plane wave propagating in an electron plasma with the dielectric function (2.63). For the sake of simplicity any material losses are neglected, i.e., we assume $\gamma = 0$ and obtain

$$\varepsilon(\omega) = 1 - \frac{\omega_p^2}{\omega^2}. \tag{2.67}$$

For the propagating electromagnetic wave we make the ansatz

$$\mathbf{E}(z,t) = \mathbf{E}_0 e^{i(kz-\omega t)}. \tag{2.68}$$

By inserting the equations (2.67) and (2.68) into the Helmholtz wave equation (2.17) the dispersion relation

$$k^2 = \frac{\omega^2}{c_0^2}\varepsilon(\omega) = \frac{\omega^2 - \omega_p^2}{c_0^2} \tag{2.69}$$

is obtained. It is evident that there are two distinct frequency regimes: For $\omega < \omega_p$ the propagation constant k becomes imaginary, i.e., there is no light propagation possible. On the other hand, for $\omega > \omega_p$ transverse electromagnetic waves can propagate through the plasma, as k is real.

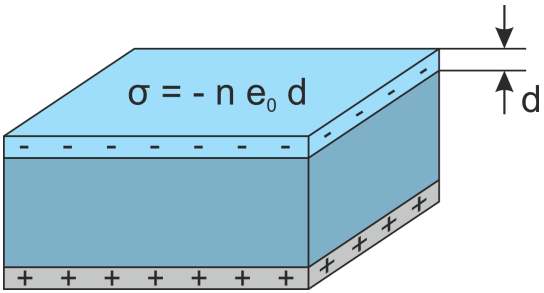

Figure 2.9: Illustration of a volume plasmon. The electrons in the metal are collectively driven at the plasma frequency ω_p. They are displaced by the distance d relative to positively charged ions. This results in a surface charge density $\sigma = -ne_0d$.

A physically interesting situation occurs if $\omega = \omega_p$. In this case, the propagation constant k vanishes, i.e., the electron excitation becomes a collective movement. Furthermore, the dielectric function $\varepsilon(\omega_p)$ becomes zero. Together with $\mathbf{D} = \varepsilon_0\varepsilon(\omega_p)\mathbf{E} = 0$ the equation (2.13) yields

$$\mathbf{E} = -\mathbf{P}/\varepsilon_0, \tag{2.70}$$

which means that the electric field is purely originating from the polarization of the medium. Figure 2.9 illustrates how this situation can be interpreted in the case of a flat piece of metal. The electrons are collectively displaced by a distance d leading to the surface charges $\sigma = -ne_0d$ and $\sigma = +ne_0d$ on the two sides of the slab. The attractive force between the two charged surfaces normalized to a single electron can be written as $F = m\ddot{d} = -e_0|E|$ with $|E| = ne_0d/\varepsilon_0$. This results in the equation of motion

$$\ddot{d}(t) + \omega_p^2 d(t) = 0. \tag{2.71}$$

From this follows that the plasma frequency can be interpreted as the characteristic frequency of an electron sea that is oscillating relatively to a fixed positively charged background. The excitation of such an oscillation is referred to as *volume plasmon*. At this point it should be noted that volume plasmons are a fundamentally different type of excitation compared to surface plasmons

and localized surface plasmons, which is discussed in the next sections. Volume plasmons are of longitudinal nature and can thus not couple to transverse light waves. Thus, they do not play a role for the magnetoplasmonic systems discussed in the following chapters.

Drude model vs real metals

Figure 2.10 depicts a comparison of the Drude model function (2.66) (orange curves) fitted to the measured permittivity of the most popular plasmonic material, namely gold (blue dots). The data was extracted from [72]. The top panel shows the imagi-

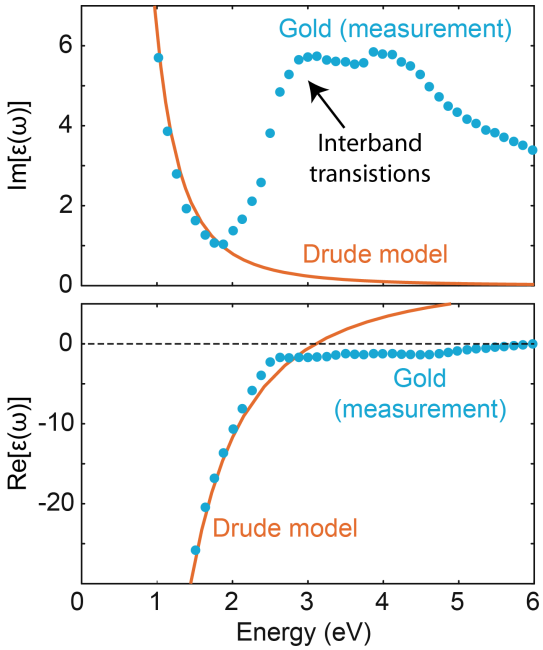

Figure 2.10: Comparison of the measured dielectric function of gold (blue dots) and the fitted model function (2.66) (orange curves). For low frequencies the is a good agreement between the modeled permittivity and the measurement. However, for higher frequencies interband transitions cause a significant deviation from the model. The measurement data was extracted from [72].

nary part, whereas the lower panel displays the real part of $\varepsilon(\omega)$. For photon energies below 2 eV (above 650 nm), there is good agreement between the model and the measurement. However, for larger frequencies the interband transitions of gold cause an increase of $\mathrm{Im}(\varepsilon)$. Silver exhibits a similar behavior (not shown here), however the accuracy of the Drude model extends until electron energies of about 3.5 eV (350 nm). Also for many other metals the Drude model yields a very accurate description of the permittivity, especially in the infrared.

In principle, the Drude model can be extended to take the interband transitions into account by adding further oscillators that contribute to $\varepsilon(\omega)$. In contrast to the equations of motion (2.57), these additional oscillators are then subjected to a restoring force in analogy to the Lorentz oscillators discussed in section 2.3.1.

2.5.2 *Surface plasmon polaritons*

Surface plasmon polaritons (SPPs) are electromagnetic waves propagating along metal-dielectric interfaces. Although SPPs are not directly utilized in the magnetoplasmonic systems analyzed in later chapters, the discussion of their most important properties provides an important context for the analysis of localized surface plasmon resonances presented in the next section.

In the following, the electrodynamics of a SPP are analyzed for the simplest case of a flat metal-dielectric interface at $z = 0$, as illustrated in figure 2.11. For an electromagnetic wave propagating in x direction we make the ansatz

$$\mathbf{E}(\mathbf{r}, t) = \mathbf{E}(z) e^{i(\beta x - \omega t)} \tag{2.72a}$$

$$\mathbf{H}(\mathbf{r}, t) = \mathbf{H}(z) e^{i(\beta x - \omega t)}. \tag{2.72b}$$

Since the geometry is invariant in y direction, $\mathbf{H}(z)$ and $\mathbf{E}(z)$ can be assumed to be independent of y. By inserting (2.72) into Maxwell's equations for time harmonic fields (2.15) it can be shown that there are two classes of solutions: TE-polarized waves, with only the components H_x, H_z and E_y being non-zero

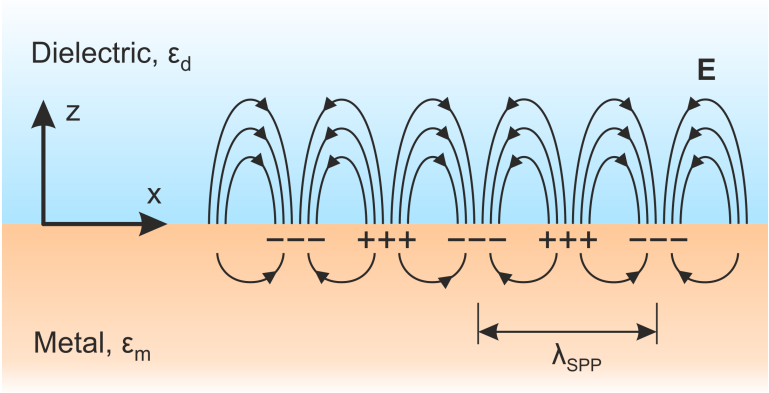

Figure 2.11: Illustration of a surface plasmon polariton (SPP) propagating along a flat metal-dielectric interface at $z = 0$.

and TM-polarized waves, with only the components E_x, E_z and H_y being non-zero. However, it should be noted that it can be shown that TE waves do not fulfill the condition that E_x and D_z are continuous at the metal-dielectric interface [72]. Hence, SPPs are always TM polarized. In the case of the TM waves, the Maxwell equations (2.15) yield

$$\frac{\partial^2}{\partial z^2} H_y(z) + \left[\frac{\omega^2}{c_0^2} \epsilon(\omega, z) - \beta^2 \right] H_y(z) = 0 \tag{2.73a}$$

$$E_x(z) = \frac{1}{i\omega\varepsilon_0\varepsilon(\omega, z)} \frac{\partial H_y(z)}{\partial z} \tag{2.73b}$$

$$E_z(z) = \frac{-\beta}{\omega\varepsilon_0\varepsilon(\omega, z)} H_y(z). \tag{2.73c}$$

Within the dielectric half-space ($z > 0$) the solutions of the equations (2.73) are given by

$$H_y(z) = C_d e^{-\kappa_d z} \tag{2.74a}$$

$$E_x(z) = C_d e^{-\kappa_d z} \frac{i\kappa_d}{\omega\varepsilon_0\varepsilon_d} \tag{2.74b}$$

$$E_z(z) = C_d e^{-\kappa_d z} \frac{\beta}{\omega\varepsilon_0\varepsilon_d} (-1), \tag{2.74c}$$

where the positive decay constant κ_d has to obey

$$\kappa_d^2 = \beta^2 - \frac{\omega^2}{c_0^2} \varepsilon_d. \tag{2.75}$$

Similary, for $z < 0$ the solutions are given by

$$H_y(z) = C_m e^{+\kappa_m z} \tag{2.76a}$$

$$E_x(z) = C_m e^{+\kappa_m z} \frac{i\kappa_m}{\omega\varepsilon_0\varepsilon_m} (-1) \tag{2.76b}$$

$$E_z(z) = C_m e^{+\kappa_m z} \frac{\beta}{\omega\varepsilon_0\varepsilon_m} (-1) \tag{2.76c}$$

with the condition

$$\kappa_m^2 = \beta^2 - \frac{\omega^2}{c_0^2} \varepsilon_m \tag{2.77}$$

for decay constant κ_m, wich is also positive. At the interface between the two half-spaces the normal component of $\mathbf{D} = \varepsilon_0 \varepsilon \mathbf{E}$ and the tangential component of $\mathbf{E}$ have to be continuous. From this follows that $C_m = C_d$ and

$$\frac{\kappa_m}{\kappa_d} = -\frac{\varepsilon_m}{\varepsilon_d}. \tag{2.78}$$

Equation (2.78) is an important intermediate result. We see that modal confinement ($\kappa_m, \kappa_d > 0$) requires $\mathrm{Re}(\varepsilon_m) < 0$, if $\varepsilon_d > 0$. In other words, SPPs indeed occur only at metal-dielectric interfaces. Furthermore, we can use equation (2.78) to eliminate κ_m and κ_d in the equations (2.75) and (2.77) and obtain the dispersion relation of SPPs:

$$\beta(\omega) = \frac{\omega}{c_0} \sqrt{\frac{\varepsilon_m(\omega)\varepsilon_d(\omega)}{\varepsilon_m(\omega) + \varepsilon_d(\omega)}}. \tag{2.79}$$

For the sake of simplicity, the dispersion of SPPs is discussed for the case of a perfect Drude metal without damping, i.e., it is assumed that the dielectric function of the metal half-space to be (2.63) with $\gamma = 0$. Figure 2.12 displays the plots of $\mathrm{Re}(\beta)$ (solid lines) and $\mathrm{Im}(\beta)$ (dotted lines) for a metal-air interface (blue) and a metal-glass interface (orange). The light cones of the corresponding dielectric half-spaces are indicated by dash-dotted lines. The dielectric function of glass is assumed to be $\varepsilon_d = 2.3$. The plots show that the SPP wavenumber is purely imaginary between the plasma frequency and the characteristic surface plasmon frequency $\omega_{SP} = \omega_p / \sqrt{1 + \varepsilon_d}$. Hence, the SPP propagation in this range is prohibited. On the other hand, for $\omega < \omega_{SP}$ the SPP wavenumber is purely real and the propagation of SPP waves is possible. For $\omega > \omega_p$ the metal becomes transparent (see section 2.5.1). Since the dispersion curves of the propagating SPPs lie outside of the light cones of the dielectric materials (dash-dotted lines), these waves cannot be excited by incident plane waves, as the photon energy and momentum cannot be conserved simultaneously. However, there is a variety of techniques that allow to excite SPPs by an incident light

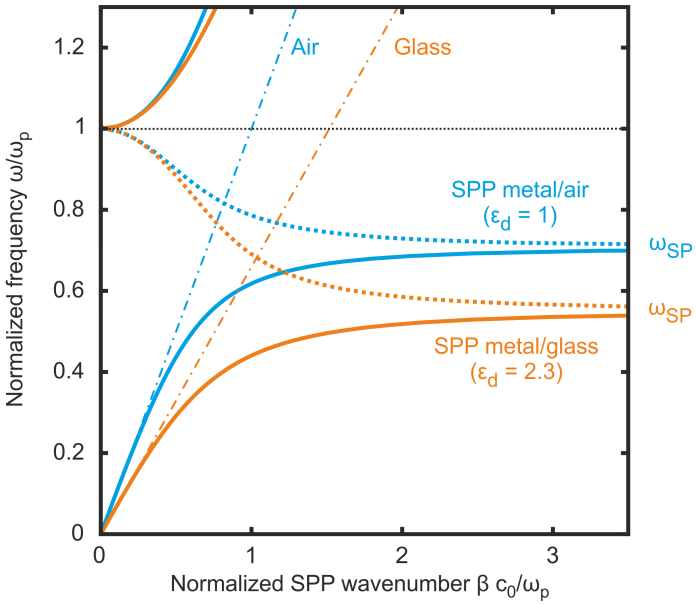

Figure 2.12: Dispersion diagram for surface plasmon polaritons at a metal-air interface (blue) and a metal-glass interface (orange). Solid lines correspond to the real part of the wavenumber β, whereas the dotted lines denote the imaginary part. The dash-dotted lines indicate the corresponding light cones of the dielectric half-spaces.

beam. Typical examples involve prism couplers, grating couplers and other surface perturbations such as edges or even dust particles. Finally, it should be pointed out that the dielectric function of a real metal does involve significant absorptive contributions, which result in a relatively fast decay of the propagating SPPs. Typical propagation lengths of SPPs are on the order of 10 to 100 μm [72].

2.5.3 *Localized surface plasmon resonances*

In this section the second important type of plasmonic excitations will be introduced: Localized surface plasmon resonances (LSPRs). This plasmonic phenomenon is of fundamental relevance for the magnetoplasmonic structures presented in later chapters. In contrast to the surface plasmon polaritons discussed in the previous section, LSPRs are non-propagating excitations. They occur in sub-wavelength metal nanoparticles surrounded by a dielectric medium. Typical resonance wavelengths of gold and silver particles are in the visible and near infrared. The small particle size also results in a high surface curvature, which enables the direct excitation of LSPRs by plane electromagnetic waves. It should be pointed out that LSPRs not only occur in metal volumes which are confined in all three dimensions, but also in structures which are infinitely extended in one dimension (i.e., in metal wires as utilized in the following chapters).

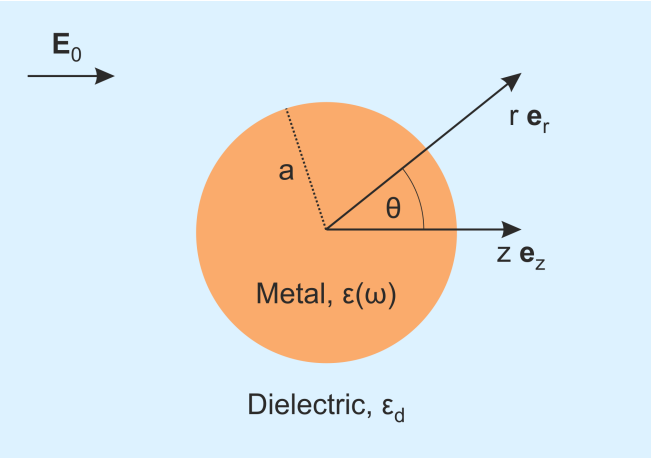

Figure 2.13: Illustration of a spherical metal nanoparticle surrounded by a dielectric medium. If the radius *a* is well below the wavelength of light, the condition for the localized surface plasmon resonance can be obtained by means of the quasistatic approximation.

To understand the fundamental mechanism behind a LSPR it is useful to investigate the simple case of a spherical metal particle with a radius a well below the wavelength of light. This situation is illustrated in figure 2.13. Due to the small particle size, the electric field of a surrounding electromagnetic wave can be assumed to be constant within a volume of the size of the sphere. Hence, the electric field of the light wave can be treated as a static field $\mathbf{E}_0 = E_0\mathbf{e}_z$ and the system is described by the Laplace equation

$$\Delta\Phi(\mathbf{r}) = 0, \tag{2.80}$$

where the electric field is obtained via $\mathbf{E}(\mathbf{r}) = -\boldsymbol{\nabla}\Phi(\mathbf{r})$. Any time-harmonic dependence can then be added subsequently to the static solution, i.e., $\mathbf{E}(\mathbf{r},t) = \mathbf{E}(\mathbf{r})e^{-i\omega t}$. This assumption is known as *quasistatic approximation*. Since the geometry in figure 2.13 possesses spherical symmetry we can write the general solution of (2.80) as

$$\Phi(r,\theta) = \sum_{l=0}^{\infty}\left[A_l r^l + B_l r^{-(l+1)}\right] P_l(\cos\theta), \tag{2.81}$$

where P_l are the Legendre polynomials [56]. The coefficients A_l and B_l are determined by the following conditions: Firstly, at the surface of the metal sphere, the tangential component of $\mathbf{E}(\mathbf{r})$ and the normal component of $\mathbf{D}(\mathbf{r}) = \varepsilon_0\varepsilon(\omega)\mathbf{E}(\mathbf{r})$ have to be continuous. Additionally, it is required that $\Phi(r,\theta) \to -E_0 r\cos\theta$ as $r \to \infty$. Applying these conditions results in

$$\Phi(r,\theta) = -\frac{3\varepsilon_d}{\varepsilon + 2\varepsilon_d} E_0 r\cos(\theta) \qquad (r < a) \tag{2.82a}$$

$$\Phi(r,\theta) = -E_0 r\cos(\theta) + \frac{\varepsilon - \varepsilon_d}{\varepsilon + 2\varepsilon_d} a^3 E_0 \frac{\cos(\theta)}{r^2} \qquad (r > a). \tag{2.82b}$$

By comparing the second term in equation (2.82b) to the generic potential of a dipole in z direction [56]

$$\Phi(r,\theta) = -\frac{1}{4\pi\varepsilon_0\varepsilon_d}\frac{p\cos(\theta)}{r^2} \tag{2.83}$$

we can identify

$$\mathbf{p} = 4\pi\varepsilon_0\varepsilon_d \frac{\varepsilon - \varepsilon_d}{\varepsilon + 2\varepsilon_d} a^3 \mathbf{E}_0. \tag{2.84}$$

Furthermore, by using $\mathbf{E}_0 = E_0\mathbf{e}_z$ and $\mathbf{r} = r\mathbf{e}_r$ we can express the equations (2.82) in the form

$$\Phi(\mathbf{r}) = -\frac{3\varepsilon_d}{\varepsilon + 2\varepsilon_d}\mathbf{E}_0 \cdot \mathbf{r} \qquad (r < a) \tag{2.85a}$$

$$\Phi(\mathbf{r}) = -\mathbf{E}_0 \cdot r + \frac{\varepsilon - \varepsilon_d}{\varepsilon + 2\varepsilon_d} a^3 \frac{\mathbf{p} \cdot \mathbf{r}}{r^3} \qquad (r > a) \tag{2.85b}$$

which is also valid for *any* direction of the electric field $\mathbf{E}_0$. So far, we see from equation (2.84) that the metal particle produces a static dipole field proportional to the applied electric field. Hence, by introducing the polarizability $\alpha(\omega)$ via the relation $\mathbf{p} = \varepsilon_0\varepsilon_d\alpha(\omega)\mathbf{E}_0$, equation (2.84) yields the important result

$$\alpha(\omega) = 4\pi a^3 \frac{\varepsilon(\omega) - \varepsilon_d}{\varepsilon(\omega) + 2\varepsilon_d}. \tag{2.86}$$

We see immediately that when $\varepsilon(\omega)$ approaches $-2\varepsilon_d$ the polarizability exhibits a resonant behavior. In the case of an approximately constant $\mathrm{Im}[\varepsilon(\omega)]$ around that resonance, the resonance condition becomes

$$\mathrm{Re}\left[\varepsilon(\omega)\right] = -2\varepsilon_d, \tag{2.87}$$

which is known as the *Fröhlich condition*. For a nanoparticle consisting of an ideal Drude metal without damping (with a dielectric function (2.67)) the Fröhlich condition is met at the resonance frequency

$$\omega_{\mathrm{SPR}} = \frac{\omega_p}{\sqrt{1 + 2\varepsilon_d}}. \tag{2.88}$$

From this we see that an increase of the refractive index around the metal particle causes a red-shift of the resonance. This behavior is utilized in refractive index sensing [73]. With the resonantly increased polarizability (and thus light absorption) also comes a

field enhancement inside and in the vicinity of the nanoparticle. This can be immediately recognized by deriving the electric fields $\mathbf{E} = -\boldsymbol{\nabla}\Phi$ associated with the potentials (2.85):

$$\mathbf{E}(\mathbf{r}) = \frac{3\varepsilon_d}{\varepsilon + 2\varepsilon_d}\mathbf{E}_0 \qquad (r < a) \tag{2.89a}$$

$$\mathbf{E}(\mathbf{r}) = \mathbf{E}_0 + \frac{1}{4\pi\varepsilon_0\varepsilon_d}\frac{3(\mathbf{e}_r \cdot \mathbf{p})\mathbf{e}_r - \mathbf{p}}{r^3} \qquad (r > a). \tag{2.89b}$$

The results we have obtained by using the quasistatic approximation are independent of the actual particle size and provide very good accuracy for nanoparticles with sizes below 100 nm. For an increasing particle size the exact derivation of the optical response is still possible for spheres (Gustav Mie 1908 [74]) but it is much more complicated. For most complex particle shapes the derivation of the field distribution and resonance condition needs to be performed numerically.

However, as a rule of thumb, for Drude metals as well as for real gold and silver an increase of the particle size in the direction of the light polarization results in a red-shift of the resonance wavelength and a broader absorption line [72]. Furthermore, as we will see in chapter 3, LSPRs also occur in less confined geometries, such as metal wires, if the light polarization is perpendicular to the wire, i.e., in the direction of the metal confinement. In analogy to the case of spheres, a plasmon resonance in a gold wire also red-shifts for increasing wire width.

2.6 RESONANCES IN GRATING-WAVEGUIDE STRUCTURES

The Faraday rotation enhancement mechanisms utilized in the chapters 3, 4 and 5 are based on modifying magneto-optic thin films such that they provide both localized surface plasmon resonances, as well as quasiguided waveguide resonances. While the origin of the first resonance type was analyzed in section 2.5, in this section the concept of quasiguided waveguide modes is discussed. The basic dispersion properties of these modes is motivated by first discussing the properties of guided modes and subsequently making the transition to periodically perturbed waveguide slabs via the *empty lattice approximation*. Since this approach is based on highly idealized assumptions, it does not allow to accurately calculate the optical response of the structures introduced in later chapters. However, it gives a basic understanding of the most important properties of quasiguided waveguide modes and their origin. This section is based on the discussions in [57, 75–77].

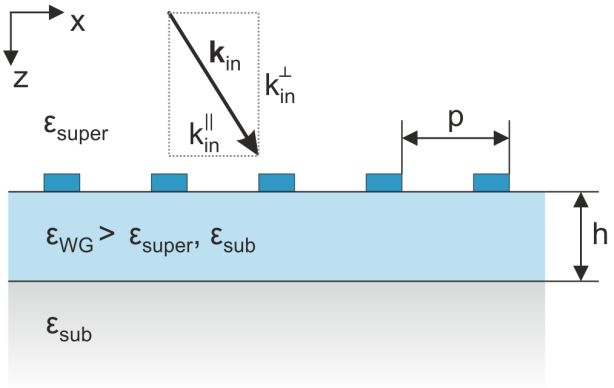

Figure 2.14: Schematic drawing of a dielectric slab waveguide (light blue) on top of a substrate (grey). The superstrate above the waveguide is drawn as empty white space. The dark blue features indicate a periodic perturbation that is assumed to involve only non-metallic elements. Furthermore, the perturbation is assumed to be so small that the influence on the effective refractive index of the slab waveguide is negligible.

Figure 2.14 shows a schematic drawing of a dielectric slab waveguide. It consists of a thin waveguide (WG) layer with thickness h and permittivity $\varepsilon_{\mathrm{WG}}$ on top of a substrate with permittivity $\varepsilon_{\mathrm{sub}}$. The superstrate, i.e., the half-space above the waveguide layer (usually air), is assumed to possess the dielectric function $\varepsilon_{\mathrm{super}}$. In order to allow light to be guided inside the center slab, the dielectric functions have to fulfill the condition $\varepsilon_{\mathrm{WG}} > \varepsilon_{\mathrm{sub}}, \varepsilon_{\mathrm{super}}$. The whole structure is assumed to be extended infinitely in y-direction. The dark blue markings indicate a periodic perturbation of the waveguide layer with periodicity p. For example, this could be a corrugated upper surface of the waveguide film or a dielectric grating with a small extension in z-direction. In later chapters, it is shown that in the case of a metallic grating, additional plasmonic resonances are introduced to the system. However, in this section only the case of purely dielectric perturbations is considered.

Guided modes

At first, let us consider the situation without any periodic corrugation. In this case the waveguide consists of three flat and homogenous layers. The corresponding optical eigenmodes are obtained by solving the Helmholtz wave equations

$$\boldsymbol{\Delta}\mathbf{E}(\mathbf{r}) + k_0^2 \varepsilon \mathbf{E}(\mathbf{r}) = 0 \tag{2.90}$$

$$\boldsymbol{\Delta}\mathbf{H}(\mathbf{r}) + k_0^2 \varepsilon \mathbf{H}(\mathbf{r}) = 0. \tag{2.91}$$

A comparison with (2.17) shows that the substitution $k_0 = \omega/c_0$ was used. It can be shown that for the considered geometry there are two types of solutions [57]: Transverse electric (TE) modes (with $\mathbf{E} = E_y \mathbf{e}_y$, $\mathbf{H} = H_x \mathbf{e}_x + H_z \mathbf{e}_z$) and transverse magnetic

(TM) modes (with $\mathbf{H} = H_y \mathbf{e}_y$, $\mathbf{E} = E_x \mathbf{e}_x + E_z \mathbf{e}_z$). For the TE modes the following ansatz can be made:

$$E_y(x,z) = Ae^{az}e^{i(k_x x - \omega t)} \quad \text{(superstrate)} \tag{2.92}$$

$$E_y(x,z) = (Be^{ik_z z} + Ce^{-ik_z z})e^{i(k_x x - \omega t)} \quad \text{(WG slab)} \tag{2.93}$$

$$E_y(x,z) = De^{-bz}e^{i(k_x x - \omega t)} \quad \text{(substrate)} \tag{2.94}$$

The ansatz for H_y in the case of TM modes (not shown here) is very similar. By applying the correct boundary conditions for the material interfaces, the following dispersion relation for TE modes is obtained [57, 77]:

$$\begin{aligned} h\sqrt{k_0^2\varepsilon_{\mathrm{WG}} - k_x^2} = \arctan &\left[\sqrt{\frac{k_0^2(\varepsilon_{\mathrm{WG}} - \varepsilon_{\mathrm{super}})}{k_0^2\varepsilon_{\mathrm{WG}} - k_x^2} - 1}\right] + \\ \arctan &\left[\sqrt{\frac{k_0^2(\varepsilon_{\mathrm{WG}} - \varepsilon_{\mathrm{sub}})}{k_0^2\varepsilon_{\mathrm{WG}} - k_x^2} - 1}\right] + m\pi. \end{aligned} \tag{2.95}$$

For TM modes the dispersion relation is given by

$$\begin{aligned} h\sqrt{k_0^2\varepsilon_{\mathrm{WG}} - k_x^2} = \arctan &\left[\frac{\varepsilon_{\mathrm{WG}}}{\varepsilon_{\mathrm{super}}}\sqrt{\frac{k_0^2(\varepsilon_{\mathrm{WG}} - \varepsilon_{\mathrm{super}})}{k_0^2\varepsilon_{\mathrm{WG}} - k_x^2} - 1}\right] + \\ \arctan &\left[\frac{\varepsilon_{\mathrm{WG}}}{\varepsilon_{\mathrm{sub}}}\sqrt{\frac{k_0^2(\varepsilon_{\mathrm{WG}} - \varepsilon_{\mathrm{sub}})}{k_0^2\varepsilon_{\mathrm{WG}} - k_x^2} - 1}\right] + m\pi. \end{aligned} \tag{2.96}$$

The equations (2.95) and (2.96) are transcendental equations, which connect the frequency of the light $\omega = c_0 k_0$ with the propagation constant k_x. The integer $(m = 0, 1, 2, 3...)$ denotes the mode order. For $\varepsilon_{\mathrm{super}} \neq \varepsilon_{\mathrm{sub}}$ the dispersion relations only possess solutions for photon energies $E = c_0 \hbar k_0$ above the cut-off energy E_{cut}. These cut-off energies are

$$E_{\mathrm{cut,TE}} = \frac{\hbar c_0}{h\sqrt{\varepsilon_{\mathrm{WG}} - \varepsilon_{\mathrm{sub}}}}\left[\arctan\left(\sqrt{\frac{\varepsilon_{\mathrm{sub}} - \varepsilon_{\mathrm{super}}}{\varepsilon_{\mathrm{WG}} - \varepsilon_{\mathrm{sub}}}}\right) + m\pi\right] \tag{2.97}$$

for TE modes and

$$E_{\text{cut,TM}} = \frac{\hbar c_0}{h\sqrt{\varepsilon_{\text{WG}} - \varepsilon_{\text{sub}}}} \left[\arctan\left(\frac{\varepsilon_{\text{sub}}}{\varepsilon_{\text{super}}} \sqrt{\frac{\varepsilon_{\text{sub}} - \varepsilon_{\text{super}}}{\varepsilon_{\text{WG}} - \varepsilon_{\text{sub}}}} \right) + m\pi \right] \tag{2.98}$$

for TM modes. Figure 2.15 displays an exemplary dispersion plot obtained by numerically solving the transcendental equations (2.95) and (2.96) for $m = 0$. The assumed structure parameters are $\varepsilon_{\text{WG}} = 3.61$, $\varepsilon_{\text{super}} = 1$, and $\varepsilon_{\text{sub}} = 2.1$, as well as $h = 140\,\text{nm}$. The energies of the TE and TM waveguide modes are plotted with blue and orange solid lines, respectively. The corresponding cut-off energies are marked with dotted lines. The light cones of air, waveguide material, and substrate are drawn as black lines. From the plot it can be seen that the modes are always above the light cone of the waveguide material. This means that for a given light frequency, the effective wavelength inside the waveguide slab is always longer than for an infinitely thick waveguide slab (i.e., bulk).

In order to realize the excitation of guided modes by incident light, the following three requirements have to be met: 1.) The polarization of the incoming light has to match the polarization of the waveguide modes. This means that TE_0 and TM_0 waveguide modes can only be excited by s-polarized and p-polarized light respectively. 2.) Energy conservation requires that the incoming light and the guided light have to have the same frequency ω. 3.) Momentum conservation requires that the component of the incoming wave vector (see figure 2.14) matches the wavenumber inside the slab, i.e.,

$$k_x = k_{\text{in}}^{||}. \tag{2.99}$$

The latter two conditions implicate that guided modes cannot be excited by incident plane waves: Looking at figure 2.15 reveals that for a given light frequency (energy), the propagation constant k_x is always larger than the wavenumber of the light cones of air and the substrate. This means that even for incident light with $k_{\text{in}}^{||} \to |\mathbf{k}_{\text{in}}|$, the equation (2.99) cannot be fulfilled.

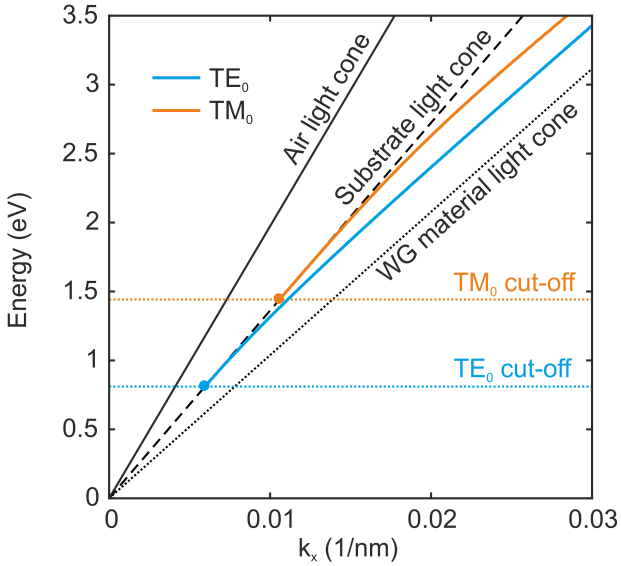

Figure 2.15: Dispersion of guided modes in a 140 nm thick waveguide. The blue curve corresponds to the TE polarized mode, wheras the orange curve denotes the TM waveguide mode dispersion. The black lines mark the light cones of air, substrate and the waveguide material.

One way to overcome the problem of simultaneous energy and momentum conservation is by utilizing prism couplers [78, 79]. This technique employs a prism with a refractive index larger than that of the waveguide slab. This prism is brought in contact with the waveguide slab and light is sent through the prism such that it is reflected at the contact interface. Due to photon tunneling, an evanescent wave is then leaking into the waveguide slab. The x component of this evanescent wave can be matched with k_x by adjusting the incident angle into the prism.

Quasiguided modes

Another way of coupling the waveguide modes to external plane waves can be realized by introducing periodic perturbations of

the waveguide surface, e.g., by attaching a grating on top of the waveguide [57, 76]. In figure 2.14 such a perturbation is indicated by the dark blue features. If this perturbation is small and the change of the effective refractive index of the waveguide slab is negligible, the modal dispersion can be assumed to be the same as in the non-disturbed case, with the only difference that the range of k_x can now be reduced to the first Brillouin zone ($-\pi/p \leq k_x \leq \pi/p$) by treating every wavenumber k_x to be equivalent to $k_x \pm l\,2\pi/p$, with ($l = 0, 1, 2, 3...$) [57]. As a result, the condition (2.99) relaxes to

$$k_x = k_{\text{in}}^{||} \pm l\frac{2\pi}{p}, \quad (l = 0, 1, 2, 3...). \tag{2.100}$$

This means that the dispersion line is folded back at the borders of the first Brillouin zone ($k_x = \pm\pi/p$). This description is called *empty lattice approximation* [75]. Exemplary results of this approximation are displayed in figure 2.16. The two plots show the modal dispersion of the same slab waveguide as discussed in figure 2.15 but with an additional periodic perturbation with $p = 300\,\text{nm}$ and $p = 550\,\text{nm}$. For better readability, only the TE_0 waveguide mode is plotted. The most notable feature of these plots is that as a consequence of the folding of the dispersion line, the TE modes now reach regions above the air and substrate light cones. In this region the corresponding TE waveguide modes no longer possess an infinite lifetime and can couple to incoming and outgoing plane waves, i.e., the modes become *quasiguided*. Of special relevance for chapter 3 are the points where the dispersion lines intersect with the line of $k_x = 0$. These points correspond to the case of normal incidence ($k_{\text{in}}^{||} = 0$ and $l = \pm1, \pm2, ...$). For example, in the case of $p = 300\,\text{nm}$ the first mode accessible for normal incidence has an energy of $E_1 = 2.5\,\text{eV}$. On the other hand, in the case of $p = 550\,\text{nm}$ the first intersection with the energy axis already happens at lower energies such that also the second intersection at E_2 lies within the plotting range. At this point we note the important result that a larger grating period leads to a lower resonance frequency.

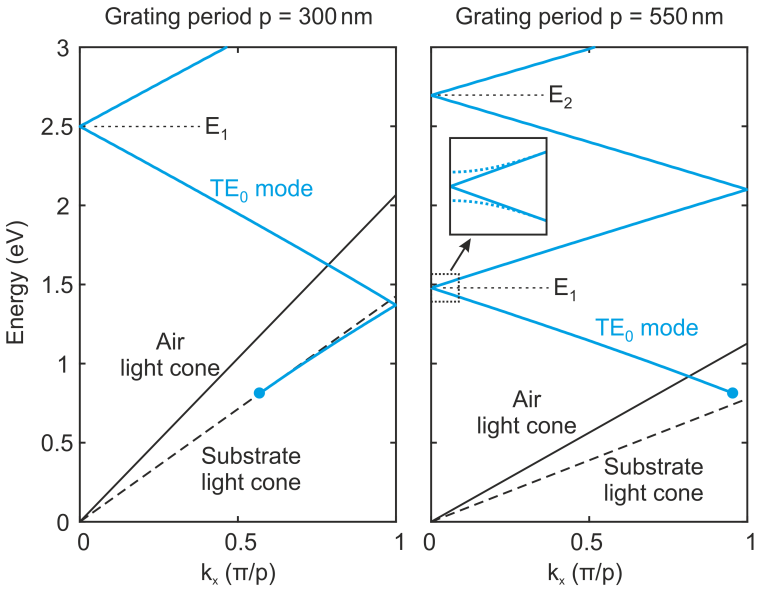

Figure 2.16: Illustration of the empty lattice approximation for the TE_0 waveguide mode in the slab waveguide structure corresponding to figure 2.15, but with an additional periodic perturbation.

Both at the center ($k_x = 0$) and at the edge of the first Brillouin zone ($k_x = \pi/p$) the modes are twofold degenerated due to the line folding. At these points the periodic structure supports two modes with the same energy, but with different symmetry of the electric field distribution with respect to the unit cell of the periodic waveguide. In the simplest case, one of the two modes shows a sinusoidal behavior with respect to the x direction, whereas the other one shows a cosinusoidal behavior. For normal incidence and systems with high symmetry, usually one of the two eigenmodes is dark, i.e., it possesses a line width of zero, and only the other mode can be excited efficiently. For an increasing incident angle, the line width of the dark mode increases and the mode becomes bright (see also section 3.3). Furthermore, when the periodic corrugation of the waveguide becomes stronger, the degeneracy of the eigenmodes at the center

and the edges of the first Brillouin zone is lifted. This is in analogy to the case of electronic Bloch wavefunctions in solids [80] and is indicated by the magnified crop next to E_1 in the right plot of figure 2.16.

The simple concept of the empty lattice approximation gives a good flavor of the nature of quasiguided modes in corrugated slab waveguides. However, in most real world grating-waveguide systems, the periodic corrugation cannot be treated as a small perturbation anymore. This is also the case for the structures investigated in chapters 3, 4, and 5. Hence, full numerical simulations are required to solve Maxwell's equations in order to accurately predict the modal dispersion and the optical response of such systems. In chapter 3 we will see that especially the introduction of metallic wire gratings dramatically influences the waveguide dispersion. As the individual grating wires provide an additional localized surface plasmon resonance, which can couple to the quasiguided waveguide modes, a new hybrid excitation emerges: The so-called *waveguide-plasmon-polariton*.

2.7 MEASURING FARADAY ROTATION OF NANOSTRUCTURES

The magneto-plasmonic systems experimentally studied in the chapters 3 and 5 are based on the magneto-optic materials EuSe and EuS, which require temperatures well below the nitrogen boiling point. Therefore, the samples are placed inside a helium cryostat system during the Faraday rotation measurement. In this section the experimental and technical details of the self-built low-temperature polarimeter are summarized.

Typical sample layout

Before the utilized experimental setup is examined as a whole, at first, the size and layout of the utilized samples should be considered. Typically, the samples were fabricated on Suprasil substrates with dimensions $10 \times 10 \times 0.5\,\mathrm{mm}$ as illustrated in figure figure 2.17. The purple color cast is due to an evaporated MO thin film (in this case it is EuS). The patches in the center of the film contain periodic arrays of plasmonic nanostructures fabricated by electron beam lithography. The patch size and thus also the maximal spot size of the measurement beam is $200 \times 200\,\mu\mathrm{m}$.

Measurement setup

The photograph in figure 2.18a gives an overview of the whole measurement arrangement. In the middle of the image one can see the blue cryostat, which contains the measured sample. The utilized *Oxford Instruments Microstat MO* is a helium flow cryostat incorporating a superconducting magnet, which produces magnetic fields of up to 5 T perpendicular to the sample surface. Furthermore, the cryostat contains two windows in the front and back side to allow light to be sent through the sample along the direction of the magnetic field. In order to position the focus spot of the measurement beam on a specific patch on the sample, the whole cryostat can be translated with $10\,\mu\mathrm{m}$ accuracy by means of the highlighted XYZ stage. On the right-hand side of the cryo-

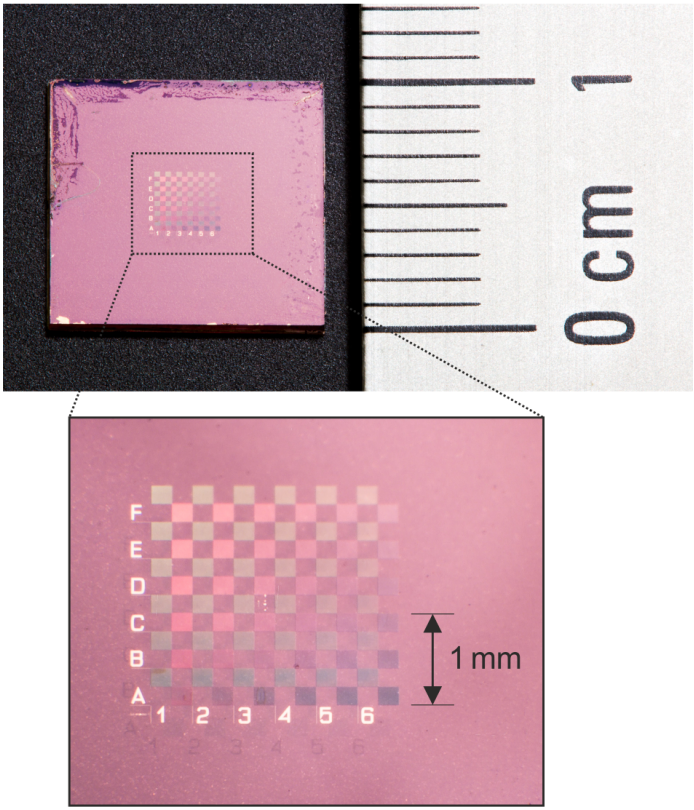

Figure 2.17: Photograph of a typical hybrid magnetoplasmonic sample as utilized in the chapters 3 and 5. The square patches are nanostructured areas with a size of $200 \times 200\,\mu$m.

stat, the incident light beam is prepared and focused onto the sample inside the cryostat. The devices on the left of the cryostat are for analyzing the polarization of the outgoing light beam.

A more detailed sketch of the setup is displayed in figure 2.18b. To understand the working principle of the setup, we now follow the light beam, starting at the laser driven plasma light source in the top part. This fiber coupled lamp is a very bright light source, which provides a small effective light emission volume. This means that the light emitted by the lamp can be focused

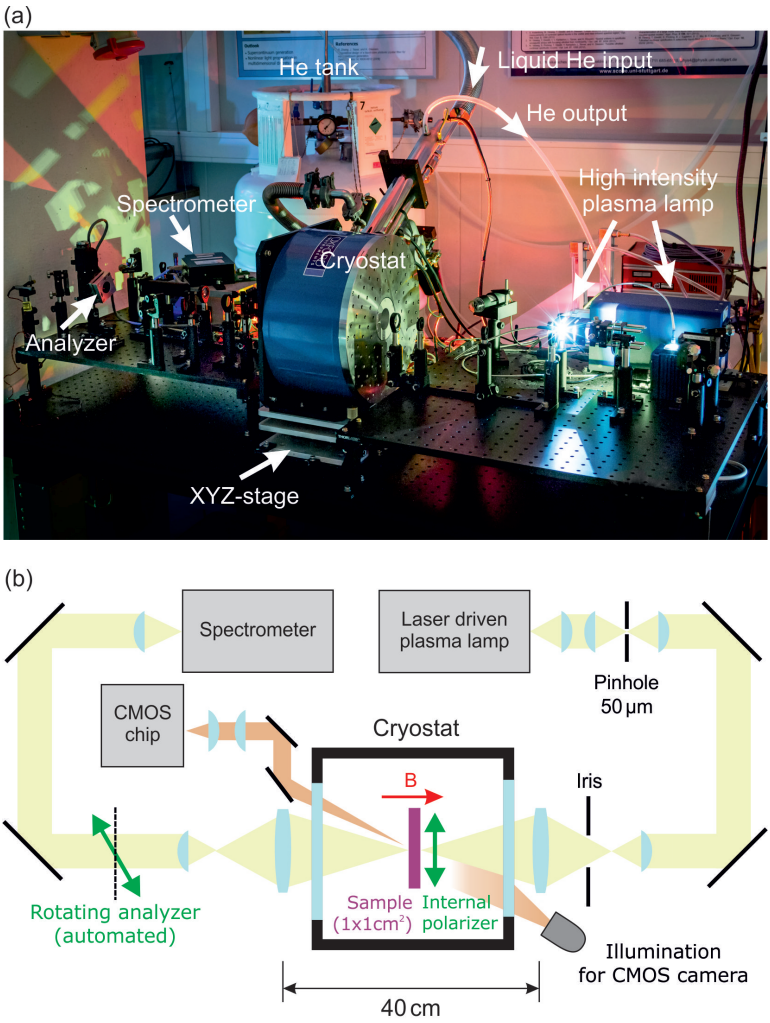

Figure 2.18: (a) Photograph of the measurement setup. (b) Schematic drawing of the light path and the utilized optical elements.

down to relatively small spot sizes. Right next to the lamp is a beam conditioning unit that produces a collimated light beam. Before this beam hits the sample in the cryostat, it is focused

down using two lenses. Their relative distance can be changed to fine tune the exact focus position. Directly in front of the sample, inside the cryostat, is a polarizer to define the polarization of the incident light. The reason for not positioning it in front of the cryostat is the following: Since the cryostat windows themselves induce a significant amount of Faraday rotation, the incident polarization would change with the applied magnetic field. However, this would be very inconvenient as a the defined incident polarization is very critical for measuring anisotropic magneto-optic samples. The utilized polarizer is a custom made variant of a *ColorPol* polarizer by the company *Codixx*. This polarizer provides an extinction ratio of $10,000 : 1$ in the wavelength range between 550 nm and 900 nm. The working principle of the polarizer relies on nanoparticles incorporated just below the surface of the plate. To avoid any Faraday rotation within the polarizer plate itself, the plate is mounted in front of the sample such that the polarizing side (where the nanoparticles are concentrated) is facing the sample. This way, the unpolarized light emitted by the lamp is only polarized just in front of the sample and the polarization state is well-controlled.

After the light passes through the sample, it exits the cryostat and is recollimated by another zoom lens system. Now the polarization state of the light beam is measured by means of a rotating (circular) polarizer, acting as analyzer. The principle behind this rotating analyzer can be explained as follows: If the polarization of the light is not altered between the polarizer inside the cryostat and the analyzer, the resulting intensity detected at the spectrometer is proportional to $\cos^2(\phi)$, where ϕ is the angle between the analyzer and the polarizer. Furthermore, if the polarization of the light is altered after the polarizer (for example due to the Faraday effect of the sample), the intensity recorded by the spectrometer can be written as

$$I(\phi) \propto \left[\cos^2(\phi - \Delta\phi) + \Delta I\right], \tag{2.101}$$

where $\Delta\phi$ is equal to the polarization rotation of the light beam. The quantity ΔI depends on the induced ellipticity, as well as on

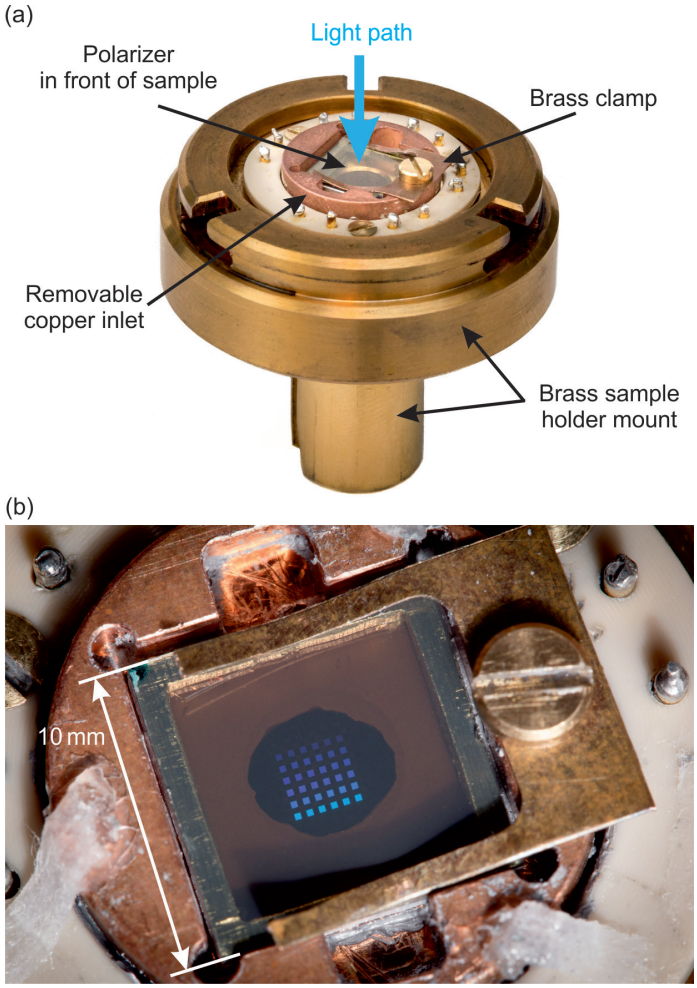

Figure 2.19: (a) Brass sample holder mount of the cryostat. (b) Detailed view on the removable copper inlet containing the sample, a spacing frame, and the polarizer plate.

the absolute Intensity and the degree of polarization of the measurement light beam. In the actual measurement the analyzer does not rotate continuously but step-wise and stands still while the spectrometer at the end of the light path records the inten-

sity $I(\phi)$ for each analyzer angle and wavelength. After that, the polarization rotation $\Delta\phi$ is obtained by fitting the recorded intensities to the relation (2.101) for each wavelength. To minimize fitting errors due to the noise in the individual intensity spectra, a sufficiently large number of rotation steps has to be recorded. For the measurements in the chapters 3 and 5 the polarizer angle ϕ was varied from -180° to $+180^\circ$ with a stepsize of 1°.

The reason for not utilizing a linear polarizer as analyzer is the following: The utilized spectrometer (HR4000 by Ocean Optics) exhibits a slightly different sensitivity for different linear polarizations. This can result in a systematic error of the measured $I(\phi)$ function. To suppress such errors, a circular polarizer was used as analyzer (with the side of the quarter-wave plate facing in the direction of the spectrometer). This causes the light coupled into the spectrometer to be circularly polarized and results in much cleaner measurements as compared to the case of a rotating linear polarizer.

Sample holder

As already pointed out, it is crucial to mount the polarizer together with the sample inside the cryostat. This is done by means of the sample holder displayed in figure 2.19a. It mainly consists of a brass mount, which is connected to the heat sink of the cryostat. The sample is situated inside a removable copper inlet, which is connected to the brass mount via heat conducting silver paste.

The copper inlet also contains the polarizer plate, as can be seen in the more detailed image in figure 2.19b. To provide a good heat transfer to the brass mount, only in the middle of the inlet there is a 5 mm aperture to allow light transmission. The sample with the nanostructures facing upwards is directly connected to the copper inlet via heat conducting silver paste. Between the sample and the polarizer plate there is a 1 mm thick aluminum frame to prevent direct contact. The stack of sample, aluminum frame and polarizer is fixed by means of a brass

clamp. The transmission axis of the polarizer plate is parallel to its edges. Furthermore, the symmetry axes of the nanostructures are also aligned with the sample substrate. This allows to easily align the polarizer with the nanostructures.

Since the polarizer is mounted to the sample holder, the incident polarization cannot be changed without opening the cryostat. Hence, in order to perform measurements with different incident polarizations, it can be useful to fabricate several versions of each nanostructure which are rotated relatively to each other.

Faraday rotation of cryostat windows

It is important to realize that the static magnetic field of the cryostat also induces significant Faraday rotation in the exit window of the cryostat and in the glass substrate of the sample. Hence, in every measurement these contributions are superimposed on the Faraday rotation of the sample. Figure 2.20 shows the Faraday rotation spectra of the mentioned glass elements for different magnetic fields. It can be seen that in the wavelength range between 500 and 800 nm the glass elements produce a considerable

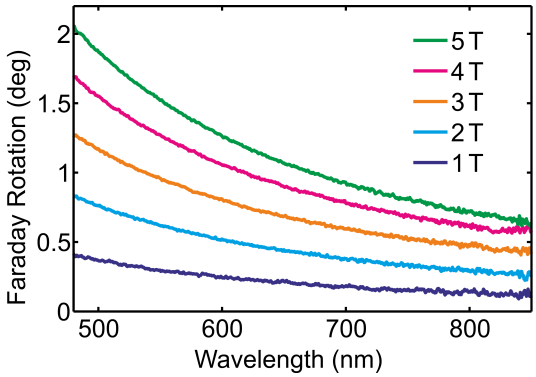

Figure 2.20: Faraday rotation of the cryostat exit window and the glass substrate of the sample for different magnetic field strengths.

rotation on the order of 1° for 5 T. This is a magnitude comparable to spectral features found in the Faraday rotation spectra of typical EuSe and EuS based nanostructures. Hence, it is important to subtract the glass contributions from all measured Faraday rotation spectra.

3

GIANT FARADAY EFFECT IN EuSe-Au STRUCTURES

In this chapter[1], the realization of an ultra-thin plasmonic Faraday rotator for the visible wavelength regime will be demonstrated. The rotator is a magneto-plasmonic hybrid structure consisting of an EuSe slab and a 1D plasmonic gold grating. At low temperatures, EuSe possesses a large Verdet constant and exhibits Faraday rotation, which does not saturate over a regime of several Tesla. By combining these properties with plasmonic Faraday rotation enhancement, as introduced by Chin *et al.* [47], giant Faraday rotation of up to 4.2° for a film thickness of only 220 nm is achieved. This magneto-optic response is five times stronger than in previously reported experiments. Furthermore, by varying the magnetic field from -5 to $+5$ T, the polarization of the transmitted light can be continuously tuned over a range of 8.4°. Through experiments and simulations, it will be demonstrated for the first time that the unique dispersion properties of such a Faraday rotator allow to tailor its working wavelength to arbitrary spectral positions within the transparency window of the magneto-optical slab. The demonstrated concept might lead to important, highly integrated, nonreciprocal, photonic devices for light modulation, optical isolation, and optical magnetic field sensing. Moreover, the simple fabrication of EuSe nanostructures by physical vapor deposition opens the way for many interesting magneto-plasmonic systems and 3D magneto-optical metamaterials.

At first, in section 3.1, the working principle of the utilized EuSe-Au nanostructures will be discussed by means of numerical

1 Major parts of this chapter were published in the article [53] under a Creative Commons Attribution-NonCommercial-ShareAlike 3.0 Unported License. The author of this dissertation is also first author of the referenced article.

simulations. After that, the experimental results are presented in section 3.2. In section 3.3 it will be elaborated on how the magneto-optic properties of the Faraday rotators depend on the angle of incidence and on the thickness of the incorporated EuSe films.

3.1 THE WAVEGUIDE-PLASMON-POLARITONIC APPROACH

From the discussion of the Faraday effect in section 2.2.3, we have seen that, in first approximation, the Faraday rotation angle scales linearly with the applied magnetic field, the material specific Verdet constant and the material thickness. Hence, as the rotation capabilities of a magneto-optic material is usually limited by a small Verdet constant, a thin-film rotator structure might seem contradictory. However, a strong Faraday effect and a low material thickness can be combined by making the rotator structure resonant. As it was also discussed in section 2.2.3, the Faraday effect is non-reciprocal, which allows light to accumulate rotation of the same sign and magnitude for both forward and backward propagation. This behavior implies that when light propagates through a medium and is reflected in the backward direction, the accumulated Faraday rotation is twice the rotation of only one pass. Moreover, the rotation can be enhanced even further by additional round-trips through the medium. This principle is utilized in the magneto-plasmonic structure schematically depicted in Figure 3.1a. The structure consists of an EuSe slab waveguide and a gold wire grating on top. Both the magnetic field and the wave vector of the incident light are assumed be perpendicular to the EuSe film. In the following, the incident polarization parallel and perpendicular to the wires is referred to as TE and TM, respectively. The gold nanowire grating has two functions. First, it acts as a waveguide coupler and allows normally incident light to couple into the slab and excite a waveguide mode (see section 2.6). The wave vectors of these modes possess a significant component in the z-direction. In ray approximation, this scenario can be understood as light bouncing back

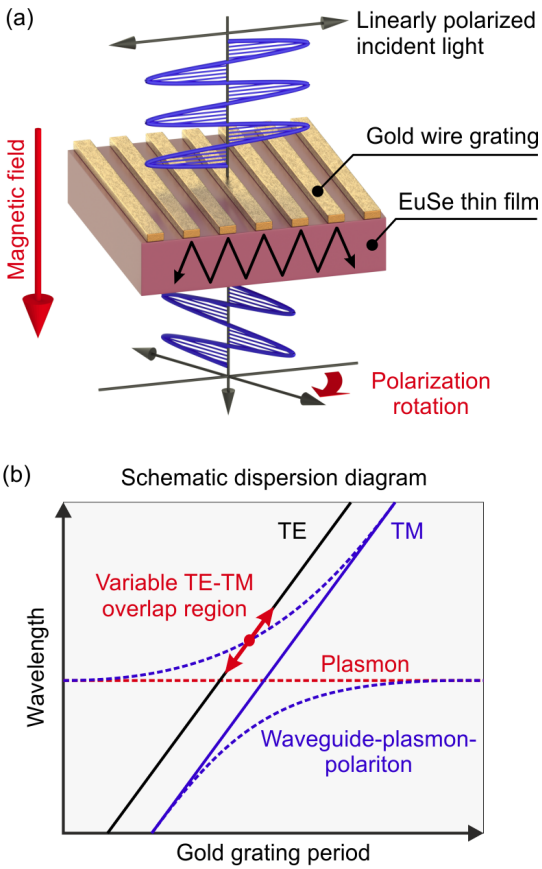

Figure 3.1: (a) Geometry of the EuSe-Au hybrid structure. The applied magnetic field and incident light are normal to the EuSe film. There are two cardinal polarization orientations, namely transverse electric (TE, electric field parallel to the gold wires) and transverse magnetic (TM, electric field perpendicular to the gold wires). (b) Schematic dispersion graph of the hybrid structure. For TM incident polarization, the plasmonic resonance of the gold wires couples strongly to the TM waveguide mode of the EuSe slab and forms a waveguide-plasmon-polariton.

and forth inside the magneto-optical film and accumulating the rotations of multiple round-trips. When light is eventually cou-

pled out of the film, due to a finite lifetime, the effective Faraday rotation is significantly larger than that for a bare film.

Many applications require wavelength-specific device operation. The presented structure design provides the freedom to tune the working wavelength (i.e., the spectral region with largest rotation enhancement) to arbitrary positions within the transparency window of the magneto-optical film. To explain the principle behind the wavelength tunability, we must first consider the connection between Faraday rotation enhancement and the dispersion properties of the hybrid structure. The largest Faraday rotation enhancement occurs at wavelengths at which the structure supports both a TM-polarized and a TE-polarized eigenmode (see section 2.6). In that case, the TM-to-TE conversion (i.e., polarization rotation) can occur most efficiently. This behavior will also be described analytically in chapter 4. Strictly speaking, the modes excited by TE- and TM-polarized incident light are themselves not purely (but mainly) TE- and TM-polarized due to the anisotropic permittivity tensor of the magneto-optical material. However, in the interest of readability, these modes are referred to as TE and TM modes, respectively. To overlap the TE and TM modes in k-space as well as at their energetic position, the second function of the metallic grating comes into play. In TM polarization, the gold wires provide a localized particle plasmon resonance that hybridizes with the TM waveguide mode of the magneto-optical slab and forms a waveguide-plasmon-polariton (WPP) [49]. For the resulting TM-polarized WPP, there will always exist a grating period such that its dispersion curve intersects with a TE waveguide dispersion curve at the same wavelength. This mechanism is illustrated in Figure 3.1b, which schematically displays the dispersion behavior of the magneto-plasmonic hybrid structure. The lines in the diagram trace the resonance frequencies of the TE and TM modes for different grating periods. The solid lines correspond to the case when the grating coupler is made of a dielectric material and thus does not support any plasmonic resonance. As it was discussed in section 2.6, in the empty-lattice approximation, the

waveguide resonance wavelength increases with larger grating periods. Since the exciting light wave is assumed to be impinging normally, the solid lies in the dispersion diagram can be associated with the energy E_1 in figure 2.16. The dispersion for a metallic waveguide coupler is depicted as dotted lines. In the dielectric case, the TE and TM modes never overlap except for the zero grating period or inclined incidence [48], whereas they overlap in the metallic case owing to the formation of the WPP. As a result of the coupling of the localized particle plasmon to the TM waveguide mode, the dispersion curve of the TM mode is bent over the TE waveguide-mode dispersion curve and an intersection is created [48, 49]. The position of this intersection directly depends on the wavelength of the localized particle plasmon in the grating wires. By increasing (decreasing) the wire width of the grating, both the plasmonic resonance and intersection point of the WPP and TE mode shift toward longer (shorter) wavelengths and larger (smaller) periods. By means of this feature, the working wavelength of the system can be tuned via the gold wire width and grating period.

In the experimental realization of the hybrid-plasmonic structure, the waveguide was made of EuSe. Already in the 1960s, in the context of research on computer memories, the group of Europium chalcogenides received attention for their exceptional magnetic properties and strong magneto-optical response at low temperatures [69, 81, 82]. In particular the compound EuSe exhibits extremely large Faraday rotation angles on the order of 1° per Tesla and micrometer thickness in the visible wavelength range at temperatures of 30 K. EuSe also possesses a high saturation magnetic flux density of 2 to 5 T, depending on the wavelength [81–83]. Furthermore, the fabrication of EuSe thin films is very simple and can be carried out by physical vapor deposition [84] (PVD). This feature is a significant advantage over bismuth iron garnet (BIG), which is widely utilized both in magneto-optical devices [85–89] and concept studies [16, 29, 47]. BIG films are typically fabricated by pulsed laser deposition [70] (PLD) followed by high-temperature annealing, which is largely restricted

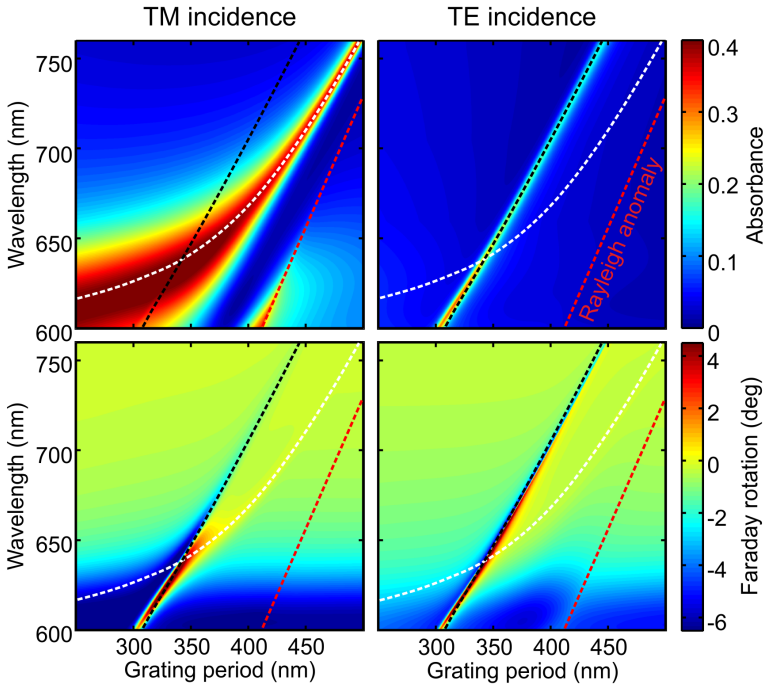

Figure 3.2: Simulation of absorbance and Faraday rotation for a 150 nm thick EuSe slab and 70 nm thick and 70 nm wide periodic gold wires. The assumed conditions are a temperature of 30 K and a magnetic field of 5 T. The black and white dashed lines denote the calculated TE and TM resonance modes. At the point where TM and TE modes overlap, the largest Faraday rotation occurs. The red dashed line indicates the Rayleigh anomaly depending on the grating period.

to homogeneous films and does not allow for the direct incorporation of other materials, such as plasmonic nanostructures, into the film. With the flexibility of PVD, EuSe provides the possibility of fabricating more sophisticated potential future designs, including 3D geometries, where the magneto-optical and plasmonic elements are merged. The gold gratings attached to the EuSe films were fabricated by electron beam lithography [90].

To support the explanation of the Faraday rotation enhancement mechanism, the dispersion behavior of the demonstrated

structures was simulated using the scattering matrix method [91]. The simulation results displayed in figure 3.2 confirm the formation of WPPs in the EuSe-Au hybrid structure for TM incidence and also show that the maximum Faraday rotation enhancement can be expected around the intersection of the TE waveguide mode and the TM-polarized WPP. The upper panels of Figure 3.2 show the simulated absorbance spectra for a 150 nm thick EuSe film with a gold wire grating on top for varying the grating periods. The gold wires are assumed to be 70 nm thick and 70 nm wide. The black and white dashed lines trace the radiating TE- and TM-mode resonance frequencies of the EuSe hybrid structure and have been derived ab initio from the scattering matrix [91]. The diffraction induced Rayleigh anomaly [49] is plotted in red. For small periods, the TM hybrid-mode dispersion is dominated by the plasmonic resonance of the gold wires and is therefore relatively broad with a weak dependence on the grating period. For larger periods, the TM hybrid-mode dispersion becomes more waveguide-like and converges toward a sharp and purely waveguide-induced resonance. Because the localized particle plasmons in the gold wires can be excited only for TM-incident polarization, the TE-mode dispersion shows a distinct feature of a waveguide resonance. The corresponding Faraday rotation spectra are shown in the lower panels of Figure 3.2. The maximum Faraday rotation occurs around the intersection of the TE and TM mode dispersion, as predicted in the previous discussion. For the case when the wave vector of the incident light is tilted, the dispersion behavior changes according to the analysis by Christ *et al.* for non-magneto-optical hybrid structures [48, 49]. However, the criterion for maximum Faraday rotation enhancement remains unchanged: it occurs where the TM waveguide-plasmon-polariton has the strongest overlap with the TE waveguide modes. More discussion on that matter can be found in section 3.3, which will also elaborate on the influence of the waveguide thickness.

In the numerical simulations, the gold has been described by tabulated data by Johnson and Christy [92]. The glass substrate

was assumed to possess a constant relative permittivity of 2.13. The diagonal elements of the permittivity tensor of the EuSe film were modeled using experimental data gained from transmission measurements of different plasmonic gratings on top of an EuSe slab. The off-diagonal elements of the dielectric tensor were obtained from measurements of a blank EuSe film at 30 K and 5 T, which is the condition given in the performed experiments.

3.2 EXPERIMENTAL REALIZATION

The Faraday rotation measurements for the EuSe-Au hybrid structures were performed in a magnet cryostat at 30 K. The polarization rotation was measured with a rotating analyzer between the illuminated sample and a spectrometer. Because the presented structures are anisotropic, for rotation measurements it is crucial that the incident light be either purely TE- or TM-polarized. For other incident polarizations, undesired reciprocal rotation contributions occur owing to different transmittance for TE and TM polarization. Wavelength-dependent deviations from the pure TE or TM polarizations can occur due to the Faraday rotation in glass elements within the reach of the magnetic field of the magnet cryostat. For this reason, an intra-cryostat polarizer was placed directly in front of the sample to ensure that the unpolarized measurement light beam is only polarized just before it hits the sample. More details on the measurement procedure can be found in section 2.7.

3.2.1 *Faraday rotation enhancement*

The simulated Faraday rotation of the EuSe-Au structures, presented in section 3.1, was subsequently confirmed experimentally. Figure 3.3a displays the transmittance and Faraday rotation spectra for TM incidence for different grating periods. The utilized EuSe film is 150 nm thick. Both the width and thickness of the gold wires is 70 nm. The corresponding spectra from the simulations are plotted in Figure 3.3b. The black curves represent

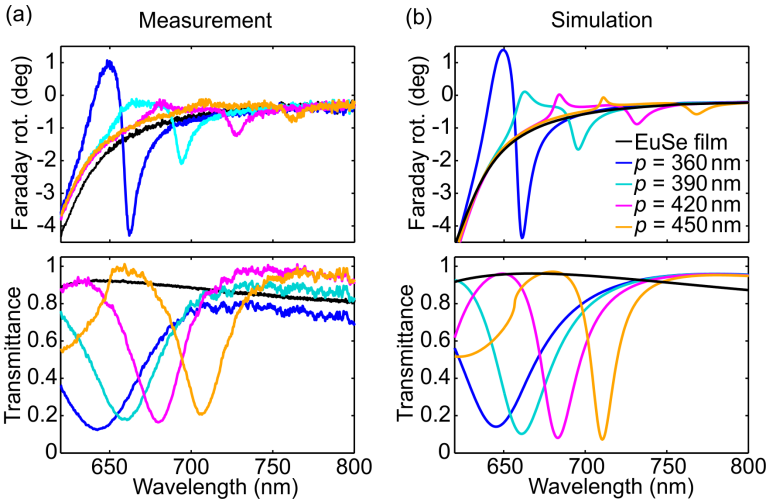

Figure 3.3: Faraday rotation and transmittance spectra for a 150 nm thick EuSe slab and 70 nm thick and 70 nm wide periodic gold wires. By varying the grating period, the overlap of the TM and TE waveguide modes can be successively increased and the Faraday rotation enhanced. (a) Measured data. (b) Simulated data.

the case of a blank EuSe film without grating. The blue curves correspond to a 360 nm grating period and represent the case where the TE- and TM-mode dispersions have the greatest overlap. Hence, the largest Faraday rotation enhancement is achieved. At 662 nm, the structure exhibits a Faraday rotation of 4.2° at reasonably high transmittance of 30 %. The other curves show that when the period is increased, the enhancement of the rotation decreases as the TE and TM modes move farther apart. As in the color-coded absorbance diagram in Figure 3.2, the resonance features of the TE mode (negative rotation contribution) and TM mode (positive rotation contribution) are drifting away from each other with an increasing grating period while simultaneously flattening out. The simulated and experimental data correspond well, although there is a difference in the Faraday rotation base line plotted in black. For small wavelengths, in the simulation, this curve completely overlaps with the colored

rotation spectra of the different gratings. However, in the measurement this is not completely the case. This discrepancy is caused by the limited temperature accuracy of the utilized cryostat system. In principle, this effect can be completely eliminated by using a cryostat that can maintain a temperature below 7 K, which is the Néel temperature of EuSe. Earlier measurements (not shown here) confirmed that in this temperature range, the Faraday rotation of EuSe is even larger and not temperature dependent.

3.2.2 *Tunable working wavelength*

As explained in section 3.1, the Faraday rotation of the waveguide material can be enhanced at selected wavelengths. The only requirement is that the material offers a sufficiently low absorption at the wavelength of interest to achieve a high-quality factor of the waveguide resonator. From the visible to the near infrared, EuSe is transparent at wavelengths larger than 550 nm [93]. Figure 3.4 shows the measured Faraday rotation spectrum

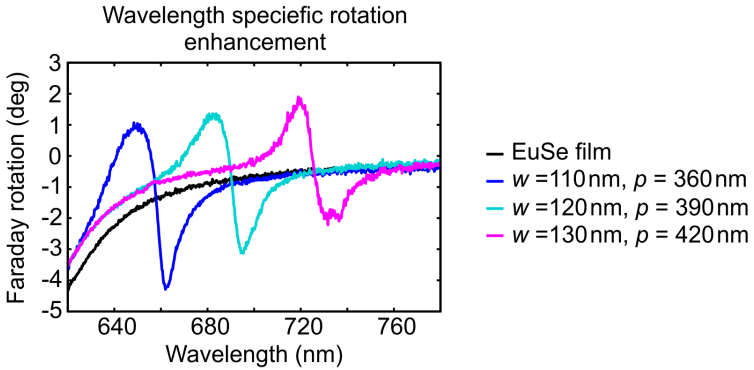

Figure 3.4: Experimental demonstration of sweeping the Faraday rotation enhancement over a range of wavelengths. The graph is showing the Faraday rotation of a 150 nm thick EuSe slab and 70 nm thick periodic gold wires. From left to right, the curves correspond to a wire width w of (70 nm, 80 nm, 90 nm) and a grating period p of (360 nm, 390 nm, 420 nm).

of a 150 nm thick EuSe film at a temperature of 30 K and a magnetic flux density of 5 T. The black curve denotes the Faraday rotation for the case without plasmonic enhancement. By tailoring the plasmonic gratings such that the TE waveguide mode and TM WPP mode dispersions overlap at different wavelengths, the Faraday rotation can be enhanced selectively at these tailored wavelengths. As it was explained in section 3.1, for a given thickness of the magneto-optical slab, the TE-TM overlap can be achieved by tuning the wire width and period of the metal wires. The colored curves in Figure 3.4 correspond to three different plasmonic gratings, which fulfill the TE-TM-matching condition. All gratings share a constant wire thickness of 70 nm. Both the wire width $w = (70\,\text{nm}, 80\,\text{nm}, 90\,\text{nm})$ and the grating period $p = (360\,\text{nm}, 390\,\text{nm}, 420\,\text{nm})$ are increasing from left to right. The resulting maximum absolute values of Faraday rotation occur at the wavelengths $\lambda = (662\,\text{nm}, 695\,\text{nm}, 736\,\text{nm})$. For longer wavelengths, both the intrinsic Faraday rotation of the film and the enhanced rotation are decreasing. This finding is in agreement with the assumption that the enhanced Faraday rotation and the intrinsic Faraday rotation of a film are approximately proportional to each other for constant absorption, a constant waveguide coupling efficiency, and thus a constant quality factor.

3.2.3 *Magnetically tunable polarization rotation*

The magnetic field dependence of the Faraday rotation was measured to demonstrate the polarization tuning capability of the demonstrated EuSe-Au structures. Figure 3.5a shows the Faraday rotation of the structure with a 360 nm grating period, 70 nm wire thickness, and 70 nm wire width for TM incidence. The magnetic field was varied from -5 T to +5 T. The structure geometry yields largest Faraday rotation at 663 nm. For this wavelength, a polarization rotation tuning range from -4.2° to +4.2° is obtained. The tuning behavior is nearly linear in the magnetic field, as can be extracted from Figure 3.5b. The polarization rotation measurement for inverted magnetic fields also acts as a control ex-

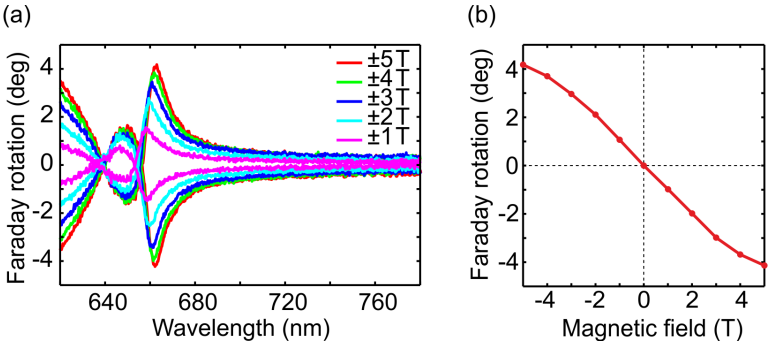

Figure 3.5: Magnetic tuning of the polarization rotation. (a) Faraday rotation of a 150 nm thick EuSe slab and 70 nm thick and 70 nm wide periodic gold wires for different applied magnetic fields. (b) Magnetic field dependence of the Faraday rotation at 663 nm.

periment to reveal potential spurious non-magnetically induced contributions. Since the measured samples are anisotropic, such effects can occur when the incident polarization deviates from an exactly TE or TM polarized state, for instance, as a result of the Faraday rotation of the cryostat windows. The highly mirror symmetric behavior of the measured rotation spectra in Figure 3.5a clearly shows that polarization errors of the incident light are well under control.

3.3 ON THE INCIDENT ANGLE AND FILM THICKNESS

The simulations and measurements presented in the sections 3.1 and 3.2 were performed for normal incidence. Here, the case of tilted incidence will be discussed by means of numerical simulations. As in the previous sections, the hybrid structure is assumed to consist of a 150 nm thick EuSe slab with 70 nm thick and wide gold wires on top. Furthermore, also a magnetic Field of 5 T and a temperature of 30 K are assumed.

The optical path length through a magneto-optical film can be increased by tilting the incident beam. However, the Faraday rotation is proportional to the component of the optical path in the

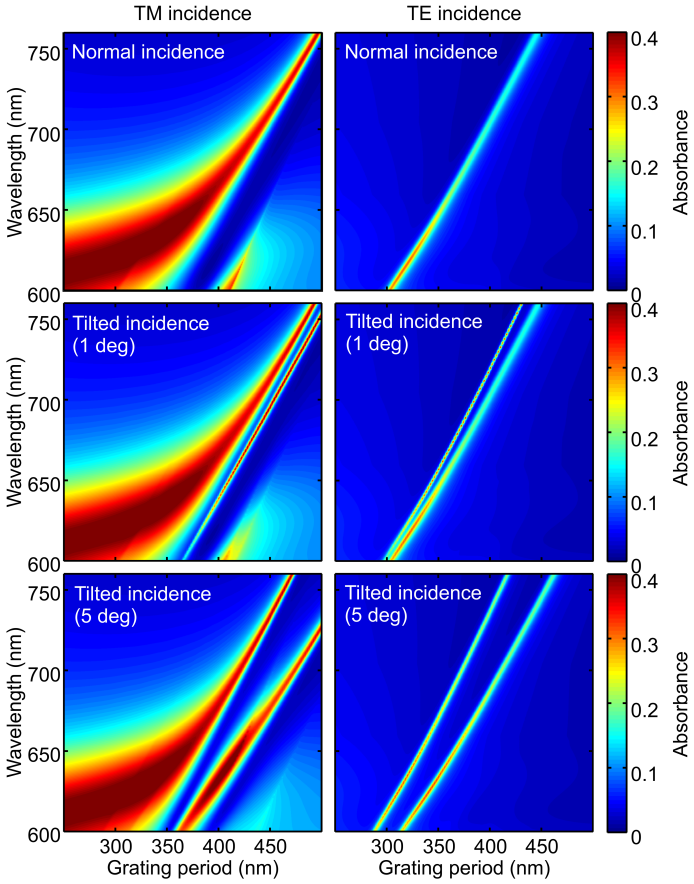

Figure 3.6: Dispersion of the absorbance for different angles of incidence.

direction of the magnetization of the material, which is perpendicular to the EuSe film. Therefore, a small tilting angle does not affect the polarization rotation in a bare film. However, a different behavior is exhibited by the presented magnetoplasmonic hybrid structures. Their WPP dispersion, and thus, also the Faraday rotation response critically depends on the incident angle. This is illustrated by the absorbance plots in figure 3.6 for both TM and TE polarized incident light, as well as for different angles of the

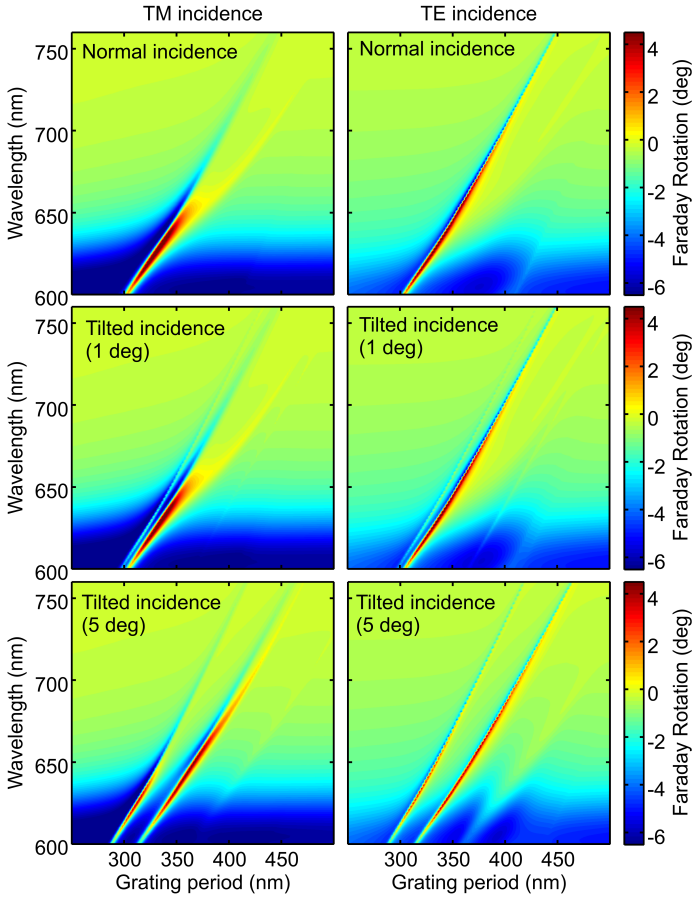

Figure 3.7: Dispersion of the Faraday rotation for different angles of incidence.

wavevector in the plane perpendicular to the gold wires. It can be clearly seen that for an increasing tilting angle, there emerges a second resonance feature both for TM and TE incidence. This is in agreement with the analysis of non-magneto-optic WPP systems by Christ *et al.* [48, 49], showing that for normal incidence there are two TE and TM polarized waveguide modes with similar frequency, where one of them is symmetry-forbidden and thus possesses zero line-width. However, by deviating from nor-

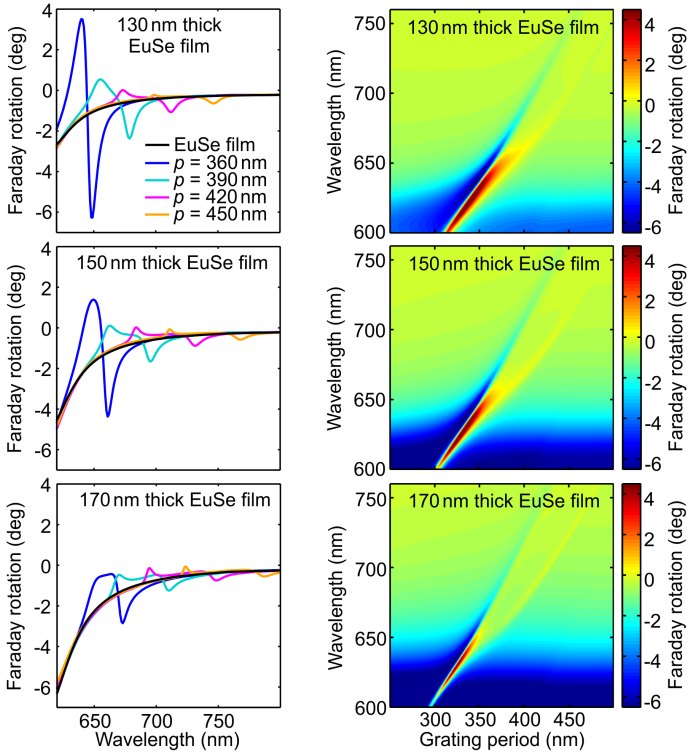

Figure 3.8: Dispersion of the Faraday rotation for different EuSe film thicknesses. The incident light is TM polarized.

mal incidence the dark waveguide modes become bright. Furthermore, with an increasing tilting angle, the two resonances move further away from each other. This behavior is also in qualitative agreement with the dispersion of a waveguide in the empty lattice approximation, as discussed in section 2.6.

Comparing the modal dispersion in figure 3.6 with the corresponding Faraday rotation plots in figure 3.7 reveals that, regardless of the more complex spectra for tilted incidence, the criterion for maximum Faraday rotation enhancement is still the same. It occurs where the TM WPP has the strongest overlap with the TE waveguide modes.

It is also interesting to investigate the influence of the thickness of the magneto-optical EuSe slab. Since the Faraday rotation of a bulk piece of material scales with its thickness, it might seem reasonable that a thicker EuSe film also leads to larger Faraday rotation. However, this is not generally the case, especially when the grating period and the wire dimensions are kept the same. To illustrate this, let us consider the dispersion diagram in figure 3.1b: Increasing the film thickness induces a redshift of the waveguide modes, whereas the plasmonic resonance remains at the same spectral position (in first approximation). As a result, the TE-TM overlap region shifts to smaller periods. The consequence of this behavior is illustrated in figure 3.8, which shows the simulated Faraday rotation dispersion spectra for different film thicknesses and different periods. The gold wires are assumed to be 70 nm thick and wide. The simulations confirm that the Faraday rotation of the film alone (far away from the TE and TM modes) increases for thicker EuSe films. However, since the TE-TM-overlap region is slightly shifted toward smaller periods, the Faraday rotation decreases for the listed periods. If desired, in principle, the shift of the TE-TM overlap could be compensated by tuning the plasmonic resonance toward longer wavelengths, which can be achieved by increasing the wire width.

3.4 CONCLUSION

An actively tunable thin-film optical rotator with a variable working wavelength was demonstrated both in experiment and in simulation. This was achieved by combining a slab of EuSe, which possesses a large Verdet constant and high saturation magnetic flux density, with a gold nanowire grating. The wavelength range of largest Faraday rotation can be selected by choosing the correct combination of grating period and wire width. The magnitude of optical rotation can be magnetically tuned over a wide angular range. At 30 K for a 220 nm thick structure, a rotation tuning range of up to 8.4° was obtained. For the present structure, this

range can presumably be doubled when cooling down to temperatures below the Néel temperature of EuSe, which is 7 K.

The demonstrated concept can be expected to have applications in highly integrated optics, demanding actively controlled optical modulation [22], magnetic field sensing [20, 21] and optical isolation [14–19]. Furthermore, the presented structure geometry is suitable for large-area fabrication [94, 95], which makes it a promising design for non-reciprocal coatings of optical elements, such as lenses, with active external control at specific wavelengths. In addition, the direct attachment onto optical fiber ends [96–98] or onto laser diodes could yield devices with extremely small volumes for a highly integrated environment.

The working principle of the presented structures is not restricted to EuSe as a waveguide material. It can be directly transferred to other magneto-optical materials. The only requirement is that the magneto-optical material provides a transparency window near the wavelength region of interest and a sufficiently high surface quality to ensure a high Q-factor. These requirements can be met by commonly used room temperature magneto-optical materials, such as BIG [70], YIG [70] or TGG [99]. For the low-temperature regime, there are also other chalcogenides, such as EuS [81], EuTe [82], EuO [100], which have similar magneto-optical properties as EuSe. The temperature at which these materials show the largest Faraday rotation can possibly be increased by doping with Gd. For example, doping EuO with Gd can raise the Curie temperature from 69 K to 135 K [67, 101]. EuSe and EuS combine large magneto-optical response, high saturation magnetic flux density, and simple thin-film fabrication via PVD. Thus, they are promising materials for further magneto-plasmonic studies with structures that are not restricted to designs including strictly continuous magneto-optical films. For example, in chapter 5, EuS will be utilized for a less than 200 nm thick structure design, that relies on an EuS thin film with an incorporated gold grating and produces Faraday rotation of up to 14°, corresponding to a tuning range of over 25°.

4

LORENTZ FORCE MODEL FOR MAGNETOPLASMONICS

It was shown recently that the Faraday rotation [47] and also the transverse magneto-optic Kerr effect [45] of a dielectric film can be enhanced considerably by attaching a resonant plasmonic grating. As it is demonstrated in chapter 3, by varying the grating and nanowire geometry, the maximal polarization rotation enhancement can be tuned to arbitrary spectral positions [53]. Such structures exhibit Faraday rotation of up to 4.2° for a thickness of 220 nm [53]. Hence, they are very relevant for future devices, such as thin-film Faraday rotators and isolators as their performance exceeds other approaches considerably.

While the experimental realization and numerical simulation of such systems received considerable attention, so far, there has not been an analytical theoretical description. In this chapter[1], a simple coupled oscillator model will be presented, that reveals the underlying physics inside hybrid magnetoplasmonic systems and yields analytical expressions for the resonantly enhanced magneto-optical response. The Lorentz nonreciprocity of the oscillator model is intrinsically incorporated via the Lorentz force, which is proportional to $\mathbf{v} \times \mathbf{B}$. Moreover, the predictions of the model are in good agreement with rigorous numerical solutions of Maxwell's equations for typical sample geometries. The demonstrated ansatz is transferable to other complex and hybrid nanooptical systems and will significantly facilitate device design.

In section 4.1 the model will be introduced and applied to the EuSe-Au structures discussed in the previous chapter. Next, the

1 Major parts of this chapter were published as an article [102] in Phyiscal Review Letters, As the author of this dissertation is also first author of the referenced article, the American Physical Society gave permission to include the text and figures of the article in this dissertation.

model will be assessed by comparing its predictions to full numerical simulations based on Maxwell's equations. In order to maintain good readability, some of the mathematical details of the model are presented separately in the sections 4.2 and 4.3.

4.1 APPLICATION TO EuSe-Au HYBRID STRUCTURES

The geometry of the investigated magneto-optical system is depicted in figure 4.1a. It consists of a dielectric magneto-optic (MO) thin film with an attached one-dimensional gold grating on top. The incident light is assumed to be linearly polarized and impinges on the sample along the z-direction. The polarization direction with electric field perpendicular (parallel) to the gold wires will be referred to as x- (y-) polarized. Figure 4.1b depicts the corresponding mechanical analog of the optical system, where each relevant optical excitation is represented by a mass suspended by a linear spring. The coupling between the different excitations is modeled by interconnecting springs. All masses are assumed to be charged and driven by the external light field. Due to its periodicity, the gold grating acts primarily as a waveguide coupler and allows for the far-field excitation of transverse electric (TE) and transverse magnetic (TM) polarized quasi-guided waveguide modes inside the MO film. In the absence of the magnetic field, the TE (TM) waveguide modes can only be excited by y- (x-) polarized incident light. Thus, the waveguide modes are modeled by one mass each, which is restricted to move only along the x- or y-direction.

The second purpose of the gold wires is to provide a localized plasmon resonance, which can be excited by x-polarized light. This plasmonic resonance is taken into account by an oscillator moving in x-direction (labeled P). Due to the field overlap, the plasmonic resonance is coupled to the TM waveguide mode [48, 49]. The dielectric response of the MO material itself is modeled by the red mass, which can move within the xy-plane and is subjected to a Lorentz force [60] in the xy-plane due to a static magnetic field $\mathbf{B}$ oriented along z-direction.

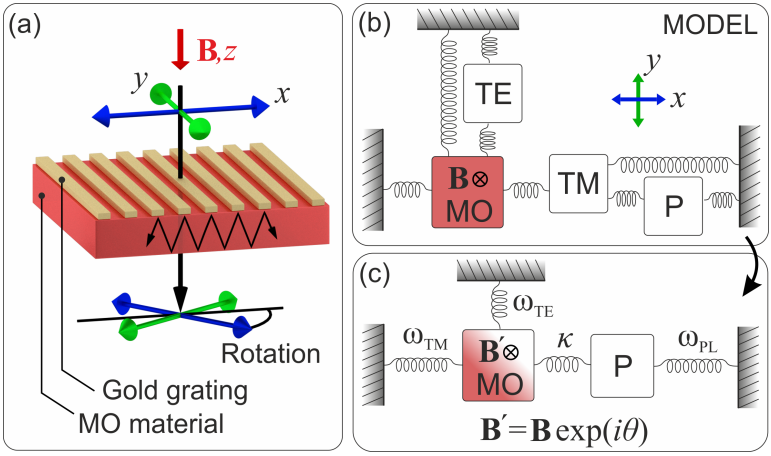

Figure 4.1: (a) Schematic drawing of the hybrid magnetoplasmonic nanostructure. (b) Mechanical analog that represents the coupling of the relevant optical excitations. (c) Simplified oscillator model providing analytical solutions.

The oscillator system in figure 4.1b possesses five degrees of freedom. Its motion is described by five coupled second order linear differential equations. While these equations can be solved exactly, it is impossible to derive closed expressions for its eigenmode frequencies. To simplify the model and allow for the analytical calculation of the eigenmode frequencies, a series of proper approximations can be applied.

First of all, neglecting the dispersion effects by the MO material itself yields significant simplification. This is achieved by assuming the driving frequency to be far away from the MO oscillator resonance and the impact of the driving force on the MO oscillator (i.e., the associated coupling constant) to be small, resulting in a reduced system of three coupled second order equations. Furthermore, in a rotating wave approximation, which is valid when the driving frequency ω is close to the eigenfrequencies Ω_j, $(j = \mathrm{TE}, \mathrm{TM}, \mathrm{P})$ of the individual oscillators, the second order equations are reduced to first order. The mathematical details of the model reduction are provided in section 4.2 and the limi-

tations of the applied approximations are discussed later in this section.

The simplified oscillator scheme is depicted in figure 4.1c. The three masses of the TE, TM and material oscillator are now merged into one waveguide oscillator. Assuming a time-harmonic oscillator displacement that is proportional to $\exp(-i\omega t)$, the governing equations in the rotating wave approximation are given by the matrix equation

$$(M_0 + \Delta M - I\omega)\mathbf{x} = \eta R\, \mathbf{E}_{||}, \tag{4.1}$$

where I is the 3×3 identity matrix, and η is a residue of the rotating wave approximation that is inversely proportional to the effective mass and the density of our oscillators (see section 4.2). The vector $\mathbf{x} = (x_{\mathrm{TM}}, x_{\mathrm{P}}, y_{\mathrm{TE}})^{\mathrm{T}}$ contains the displacements of the corresponding oscillators in the xy-plane, while $\mathbf{E}_{||} = (E_x, E_y)^{\mathrm{T}}$ denotes the driving electric field. The forces acting on each oscillator are proportional to $R\,\mathbf{E}_{||}$, with the charge density matrix

$$R = \begin{pmatrix} \rho_{\mathrm{TM}} & 0 \\ \rho_{\mathrm{P}} & 0 \\ 0 & \rho_{\mathrm{TE}} \end{pmatrix}. \tag{4.2}$$

Furthermore, M_0 accounts for the coupling of the TM waveguide mode and the plasmon [48], with

$$M_0 = \begin{pmatrix} \omega_{\mathrm{TM}} & -\kappa & 0 \\ -\kappa & \omega_{\mathrm{P}} & 0 \\ 0 & 0 & \omega_{\mathrm{TE}} \end{pmatrix}. \tag{4.3}$$

The corresponding coupling constant κ is assumed to be purely real, while $\omega_j = \Omega_j - i\Gamma_j$, $(j = \mathrm{TE}, \mathrm{TM}, \mathrm{P})$ are complex frequencies that consist of the resonance frequencies Ω_j and the damping coefficients Γ_j (due to radiative and absorptive losses) of the different modes. The antisymmetric matrix ΔM denotes the nonreciprocal influence of the magnetic field via the Lorentz force proportional to $\mathbf{v} \times \mathbf{B}$ and is defined as

$$\Delta M = \beta e^{i\theta} \begin{pmatrix} 0 & 0 & -i \\ 0 & 0 & 0 \\ +i & 0 & 0 \end{pmatrix}, \tag{4.4}$$

with the real coupling coefficient β, that is proportional to the static magnetic field. The factor $\exp i\theta$ stems from the four-oscillator model and represents the phase of the MO oscillator in that system. In the sections 4.2.2 and 4.3 it is shown by perturbation theory [103, 104] that this phase corresponds to the phase of the gyration $g = |g| \exp(i\theta)$ of the MO material.

The optical response of the system is obtained by assigning an effective susceptibility to the system. This is done by summing up the effective electronic polarization $\mathbf{P}_{||} = \chi \mathbf{E}_{||}$, which can be identified as $\mathbf{P}_{||} = R^{\mathrm{T}}\mathbf{x}$. Hence, the effective susceptibility can be written as

$$\chi(\omega) = \eta R^{\mathrm{T}} M(\omega)^{-1} R, \tag{4.5}$$

with $M(\omega) = M_0 + \Delta M - I\omega$. Due to the cross product in the Lorentz force, ΔM and thus $M(\omega)$ become antisymmetric for non-zero magnetic fields, reflecting the nonreciprocity of the system [3, 10].

The eigenfrequencies of the coupled oscillator system are obtained by setting the external electric field in equation (4.1) to zero. This results in the following eigenvalue problem

$$(M_0 + \Delta M)\mathbf{x}_n = \omega_n \mathbf{x}_n, \tag{4.6}$$

where ω_n denotes the eigenvalues, and $\mathbf{x}_n$ the eigenvectors for $n = 1, 2, 3$. In the presented model, the Lorentz force is assumed to be weak compared to the restoring forces. Hence, ΔM is regarded as a small perturbation of M_0, resulting in ω_n being close to the eigenfrequencies of M_0. The eigenfrequencies of M_0 are given by

$$\omega_{1/2} = \frac{\omega_{\mathrm{TM}} + \omega_{\mathrm{P}}}{2} \mp \sqrt{\kappa^2 + \left(\frac{\omega_{\mathrm{TM}} - \omega_{\mathrm{P}}}{2}\right)^2}, \tag{4.7}$$

$$\omega_3 = \omega_{\mathrm{TE}}. \tag{4.8}$$

The first two eigenfrequencies correspond to the two branches of a WPP hybrid mode arising from the coupling between the plasmonic mode and the TM waveguide mode [48, 49]. The

third eigenfrequency is simply the frequency of the TE polarized waveguide mode. In chapter 3, it was demonstrated numerically that the largest magneto-optical response occurs for grating periods at which the TE waveguide mode and one of the TM polarized WPP branches possess similar resonance frequencies, i.e., when $\omega_{1/2} = \omega_{\mathrm{TE}}$. This behavior can now be deduced analytically from the presented model by examining the inverse of M for a small perturbation ΔM:

$$M^{-1} \approx (M_0^{-1} - I\omega) - \frac{i\beta e^{i\theta}}{(\omega_1 - \omega)(\omega_2 - \omega)(\omega_{\mathrm{TE}} - \omega)} \times \begin{pmatrix} 0 & 0 & +(\omega - \omega_{\mathrm{P}}) \\ 0 & 0 & -\kappa \\ -(\omega - \omega_{\mathrm{P}}) & +\kappa & 0 \end{pmatrix}. \quad (4.9)$$

This expression reveals that the magnetic terms proportional to β become largest for $\omega = \omega_{\mathrm{TE}} = \omega_{1/2}$, which confirms previous numerical findings.

To obtain the effective susceptibility for a particular nanostructure, the free parameters in M and R have to be deduced by a systematic and rigorous fitting procedure. Our fitting process consists of three steps, in which M_0, R, and ΔM are fitted sequentially. Full numerical simulations based on the scattering matrix method [91, 105] were used as reference. In the following, the three fitting steps are discussed and applied to a sample geometry that consists of a 150 nm thick EuSe film with 70 nm thick and 70 nm wide gold wires on top (see figure 4.1a). The substrate under the film is assumed to be glass with a permittivity $\varepsilon = 2.13$. The applied magnetic field is assumed to be 5 T. The permittivity of the gold grating is modeled using the Drude model function $\varepsilon(\omega) = \varepsilon_\infty - \omega_p^2/(\omega^2 + i\gamma\omega)$, which was introduced in section 2.5.1. The model parameters for gold were ex-

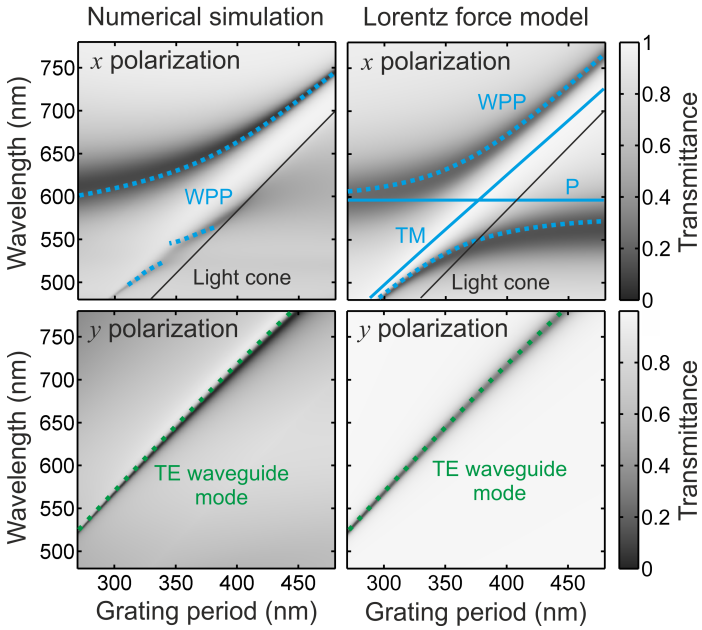

Figure 4.2: Comparison between transmittance spectra and modal dispersion derived from numerical simulations (left panels) and the Lorentz force oscillator model (right panels). TM (TE) polarized modes are plotted as blue (green) dashed lines. Blue solid lines indicate the uncoupled plasmon and TM waveguide frequencies.

tracted from reference [46] and set to $\varepsilon_\infty = 7.9$, $\omega_p = 8.77\,\text{eV}$, and $\gamma = 1.13 \times 10^{14}\,\text{s}^{-1}$. The components of the permittivity tensor

$$\varepsilon_{\text{EuSe}} = \begin{pmatrix} \varepsilon_{11} & \varepsilon_{12} & \varepsilon_{13} \\ -\varepsilon_{12} & \varepsilon_{22} & \varepsilon_{23} \\ -\varepsilon_{13} & -\varepsilon_{23} & \varepsilon_{33} \end{pmatrix} \tag{4.10}$$

of the magneto-optical slab are assumed to be $\varepsilon_{11} = \varepsilon_{22} = 4.95 + 0.007i$, $\varepsilon_{33} = 3.9643 + 0.0126i$, $\varepsilon_{12} = 0.061 + 0.061i$, and $\varepsilon_{13} = \varepsilon_{23} = 0$. These values correspond to a 150 nm thick EuSe thin film at a wavelength of 660 nm and a magnetic field of 5 T in z-direction. These data were obtained by previous magneto-optical measurements [53].

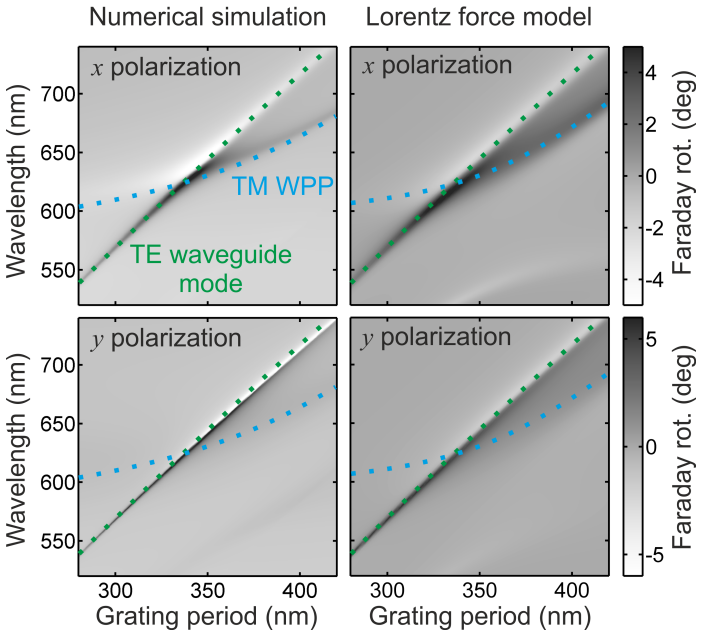

Figure 4.3: Comparison of the Faraday rotation derived from numerical simulations (left panels) and the Lorentz force oscillator model (right panels). The eigenfrequencies corresponding to the upper TM polarized waveguide plasmon polariton (WPP) branch and the TE waveguide mode are drawn as dashed lines.

In the first step, the free parameters in M_0 are fitted such that the eigenfrequencies of the mechanical system match the eigenfrequencies of the actual nanostructure obtained by rigorous numerical solutions of Maxwell's equations. While Eq. (4.8) allows the direct derivation of ω_{TE}, the complex coefficients ω_{TM}, ω_{P}, and the real coefficient κ in Eq. (4.7) cannot be deduced directly from the full numerical simulations. This can be resolved by calculating the real part of ω_{TM} from an empty lattice approximation [75] and assuming $\Gamma_{\mathrm{TM}} \approx \Gamma_{\mathrm{TE}}/10$, as justified by the results by Christ *et al.* [48, 49]. Figure 4.2 shows the comparison between the simulated and fitted eigenmodes of the oscillator model that includes the Lorentz force. The eigenmodes are plotted as blue (TM) and green (TE) dashed lines in units of wavelength. The

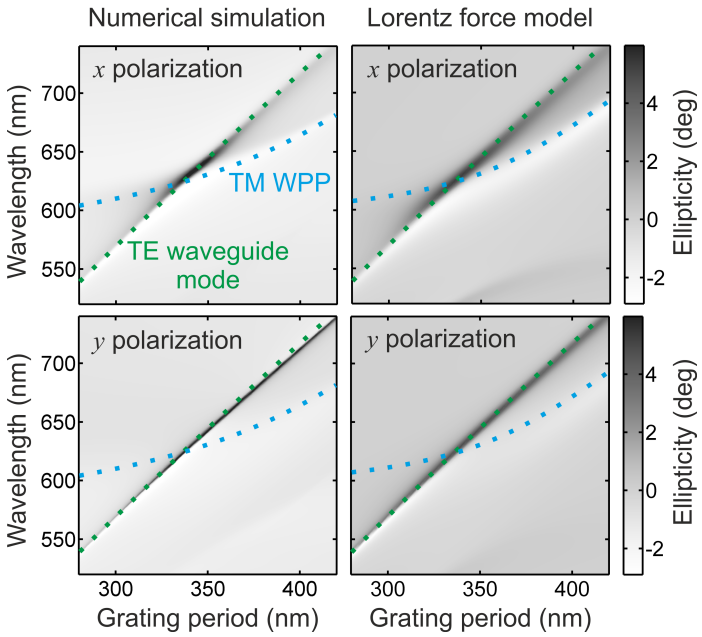

Figure 4.4: Comparison of the ellipticity derived from numerical simulations (left panels) and the Lorentz force oscillator model (right panels). The eigenfrequencies corresponding to the upper TM polarized waveguide plasmon polariton (WPP) branch and the TE waveguide mode are drawn as dashed lines.

solid black lines mark the edge of the light cone (i.e., the Rayleigh anomaly). The blue solid lines correspond to the frequencies of the individual oscillators. Especially in the most relevant region around the intersection of the TE waveguide mode and WPP, the modal dispersion is reproduced very well by the oscillator model. Outside this region, in the simulated TM dispersion at around 530 nm, there is a discontinuity due to the presence of another spectrally close higher-order mode. As expected [106], the eigenmodes of the actual nanostructure exhibit a cut-off at the edge of the light cone (see also section 2.6). Since the model does not take the periodic geometry into account, this discontinuity is missing in the dispersion plot of the model.

In the second part of the fitting sequence, the coefficients in R are derived by the condition that the transmittance of the effective medium has to reproduce that of the actual sample. In analogy to the first fitting step, it is assumed that the magnetic field only has weak influence on the absorption behavior. Hence, the absorption can be derived from the effective susceptibility for zero B-field. This is done by setting $\Delta M = 0$ and solving the Helmholtz equation to obtain the evolution of an x- and y-polarized plane wave over an effective propagation distance (see section 2.2.2). The effective propagation distance was assumed to be the sample thickness of 220 nm. For the sake of simplicity, the coefficients in R were assumed to be constant for all grating periods. By comparing the simulated transmittance in figure 4.2 (left panels) and the modeled transmittance (right panels), it can be seen that, except for the discontinuities outside the region of interest, as discussed above, the line shapes agree very well.

In the last part of the fitting procedure, the remaining magneto-optical coefficients in ΔM are determined. Far away from the MO material resonance, the gyration $g = |g| \exp(i\theta)$ can be assumed to be constant. For bismuth iron garnet [47] and EuSe [53], this assumption is valid for the red and near-IR spectral region, where $\theta \approx -45\,\mathrm{deg}$. This is also the value used for the oscillator model and the numerical simulations. Note that our model will work as well for other materials exhibiting different θ (see section 4.3). The last remaining fitting parameter is β, which is proportional to the magnetic field. For realistic magnetic field strengths, its value only influences the magnitude of the MO response but not its spectral line shape. Thus, β is scaled such that the MO response of the modeled system reaches the values of the full simulation.

Figure 4.3 depicts the comparison of the resulting Faraday rotation spectra from the full numerical simulations and the oscillator model. The green and blue dotted lines trace the eigenmodes. As expected by examining Eq. (4.9), the MO response is largest around the intersection point of the TM polarized WPP and the TE waveguide mode. Furthermore, the qualitative and quantita-

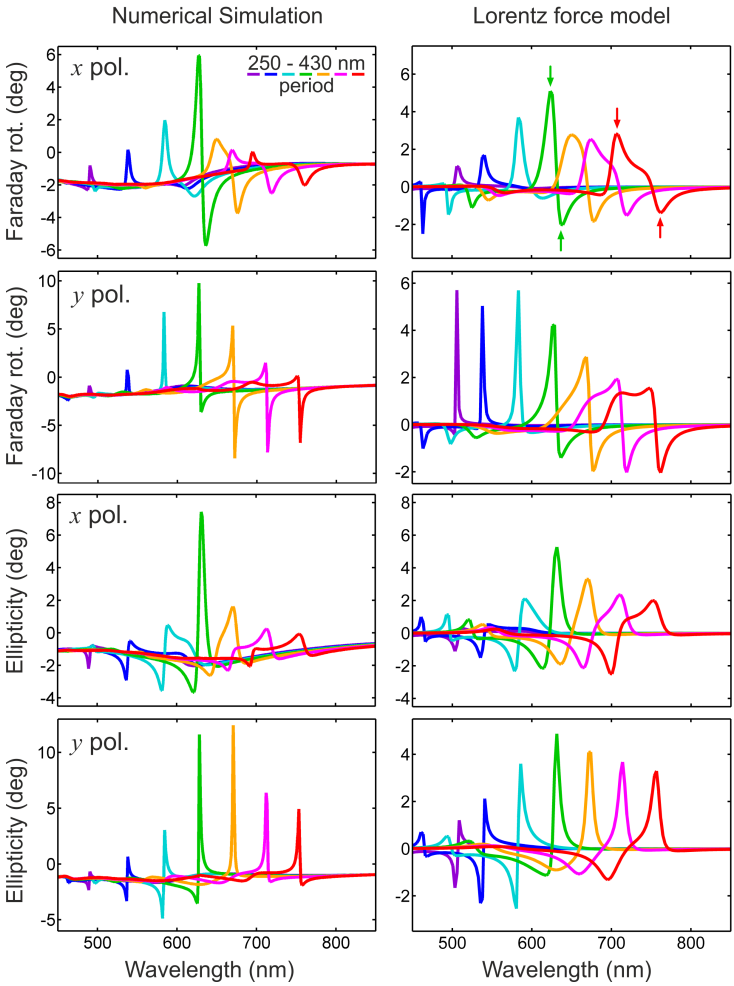

Figure 4.5: Comparision of the Faraday rotation derived from numerical simulations (left panels) and the Lorentz force oscillator model (right panels). The spectra correspond to slice cuts from figure 4.3 at equidistant periods from 250 nm to 430 nm with 30 nm spacing.

tive agreement between model and numerical simulation is excellent.

The corresponding dispersion of the ellipticity response is displayed in figure 4.4. It can be seen, that the ellipticity predicted by the model is also in good agreement with numerical simulation. As in the case of the Faraday rotation dispersion, it can be seen that the ellipticity response is strongest around the intersection region of the TE waveguide mode and the TM polarized waveguide-plasmon-polariton mode, and lowest far-off resonance.

To compare the exact line shapes of the MO spectra, figure 4.5 displays the corresponding slice cuts of the Faraday rotation and ellipticity spectra. The model reproduces the line shapes very well. This includes the characteristic up-down feature in the Faraday rotation for x-polarization (indicated by arrows), which is successively spreading for periods larger than the period of the TE-WPP intersection (green line) as it was also described in chapter 3. On the other hand, the modeled MO spectra do not reproduce the offset in the numerically simulated spectra. This is a result of the approximations required for the reduction of the four-oscillators-model to the two-oscillators model. There, the oscillator strength of the MO material was assumed to be much smaller than the oscillator strength of the waveguide modes and the plasmon. As a result, only the resonant contributions to the MO response are taken into account. The slightly broader MO features result from fitting the resonance linewidths to the values from numerical simulations. A better qualitative agreement in Faraday rotation could be obtained when adjusting the losses in our model independently of the calculated resonance line widths. In summary, it is evident that even the simplified oscillator model correctly predicts the overall shape of the MO spectra very well.

4.2 SIMPLIFICATIONS AND APPROXIMATIONS

In this section, the equation of motion (4.1) of the simplified oscillator model will be derived explicitly. The discussion will start from the equations of motions of the extended oscillator model with five degrees of freedom (figure 4.1b) described by five cou-

pled second order linear differential equations. By applying appropriate simplifications the system of five equations can be reduced to three coupled quadratic equations, which describe the motion of effectively three oscillators. Furthermore, in order to obtain an analytical solution of the three-oscillator problem, a rotating wave approximation will be applied.

4.2.1 *Extended model (5 degrees of freedom)*

For light propagating in z direction ($E_z = 0$), the equations of motion for the four-oscillators model in figure 4.1b are given by

$$X_{\mathrm{MO}} - k_{\mathrm{MO,TM}} x_{\mathrm{TM}} - k_m \dot{y}_{\mathrm{MO}} = \frac{q_{\mathrm{MO}}}{m} E_x e^{-iwt} \quad (4.11a)$$

$$Y_{\mathrm{MO}} - k_{\mathrm{MO,TE}} y_{\mathrm{TE}} + k_m \dot{x}_{\mathrm{MO}} = \frac{q_{\mathrm{MO}}}{m} E_y e^{-iwt} \quad (4.11b)$$

$$X_{\mathrm{TM}} - k_{\mathrm{MO,TM}} x_{\mathrm{MO}} - k_{\mathrm{P,TM}} x_{\mathrm{P}} = \frac{q_{\mathrm{TM}}}{m} E_x e^{-iwt} \quad (4.11c)$$

$$Y_{\mathrm{TE}} - k_{\mathrm{MO,TE}} y_{\mathrm{MO}} = \frac{q_{\mathrm{TE}}}{m} E_x e^{-iwt} \quad (4.11d)$$

$$X_{\mathrm{P}} - k_{\mathrm{P,TM}} x_{\mathrm{TM}} = \frac{q_{\mathrm{P}}}{m} E_x e^{-iwt}, \quad (4.11e)$$

where the lower case variables x_j and y_j with (j = MO, P, TE, TM) denote the displacements of the oscillators associated with the magneto-optical (MO) material, the plasmon mode (P), as well as the TE and TM waveguide modes in x and y direction. The upper case symbols X_j and Y_j denote terms of the form

$$X_j = \ddot{x}_{\mathrm{j}} + \Omega_{\mathrm{j}}^2 x_{\mathrm{j}} + 2\Gamma_{\mathrm{j}} \dot{x}_{\mathrm{j}} \quad (4.12a)$$

$$Y_j = \ddot{y}_{\mathrm{j}} + \Omega_{\mathrm{j}}^2 y_{\mathrm{j}} + 2\Gamma_{\mathrm{j}} \dot{y}_{\mathrm{j}} \quad (4.12b)$$

with (j = MO, P, TE, TM). Dots indicate a time derivative. The coefficient k_m is proportional to the magnetic field. Due to the cross product in the Lorentz force $\propto (\mathbf{v} \times \mathbf{B})$, it occurs in the first two equations with opposite signs. In order to reduce the number of parameters in the model, the oscillator masses m are

assumed to be equal for all oscillators. The time harmonic ansatz $\exp(-i\omega t)$ for the displacements leads to

$$W_{\mathrm{MO}}(\omega)x_{\mathrm{MO}} - k_{\mathrm{MO,TM}}x_{\mathrm{TM}} + i\omega k_m y_{\mathrm{MO}} = \frac{q_{\mathrm{MO}}}{m}E_x \tag{4.13a}$$

$$W_{\mathrm{MO}}(\omega)y_{\mathrm{MO}} - k_{\mathrm{MO,TE}}y_{\mathrm{TE}} - i\omega k_m x_{\mathrm{MO}} = \frac{q_{\mathrm{MO}}}{m}E_y \tag{4.13b}$$

$$W_{\mathrm{TM}}(\omega)x_{\mathrm{TM}} - k_{\mathrm{MO,TM}}x_{\mathrm{MO}} - k_{\mathrm{P,TM}}x_{\mathrm{P}} = \frac{q_{\mathrm{TM}}}{m}E_x \tag{4.13c}$$

$$W_{\mathrm{TE}}(\omega)y_{\mathrm{TE}} - k_{\mathrm{MO,TE}}y_{\mathrm{MO}} = \frac{q_{\mathrm{TE}}}{m}E_y \tag{4.13d}$$

$$W_{\mathrm{P}}(\omega)x_{\mathrm{P}} - k_{\mathrm{P,TM}}x_{\mathrm{TM}} = \frac{q_{\mathrm{P}}}{m}E_x, \tag{4.13e}$$

where $W_j(\omega) = -\omega^2 + \Omega_j^2 - 2i\Gamma_j\omega$, $(j = \mathrm{MO, TM, TE, P})$. In matrix form, equation (4.13e) reads

$$M(\omega)\,\mathbf{x} = \frac{1}{m}Q\,\mathbf{E}_{||}. \tag{4.14}$$

Here, we introduced the vectors $\mathbf{x} = (x_{\mathrm{MO}}, y_{\mathrm{MO}}, x_{\mathrm{TM}}, y_{\mathrm{TE}}, x_{\mathrm{P}})^{\mathrm{T}}$ as well as $\mathbf{E}_{||} = (E_{\mathrm{x}}, E_{\mathrm{y}})^{\mathrm{T}}$ and the matrices

$$M(\omega) = \begin{bmatrix} W_{\mathrm{MO}}(\omega) & +i\omega k_m & -k_{\mathrm{MO,TM}} & 0 & 0 \\ -i\omega k_m & W_{\mathrm{MO}}(\omega) & 0 & -k_{\mathrm{MO,TE}} & 0 \\ -k_{\mathrm{MO,TM}} & 0 & W_{\mathrm{TM}}(\omega) & 0 & -k_{\mathrm{P,TM}} \\ 0 & -k_{\mathrm{MO,TE}} & 0 & W_{\mathrm{TE}}(\omega) & 0 \\ 0 & 0 & -k_{\mathrm{P,TM}} & 0 & W_{\mathrm{P}}(\omega) \end{bmatrix} \tag{4.15}$$

and

$$Q = \begin{pmatrix} q_{\mathrm{MO}} & 0 \\ 0 & q_{\mathrm{MO}} \\ q_{\mathrm{TM}} & 0 \\ 0 & q_{\mathrm{TE}} \\ q_{\mathrm{P}} & 0 \end{pmatrix}. \tag{4.16}$$

The optical response of the system is obtained by assigning an effective susceptibility to the system. This is done by summing up the effective electronic polarization $\mathbf{P}_{||} = \chi \mathbf{E}_{||}$, which is given by $\mathbf{P}_{||} = nQ^{\mathrm{T}}\mathbf{x}$, where n denotes the effective oscillator density. Hence, the effective susceptibility can be written as

$$\chi(\omega) = \frac{n}{m} Q^{\mathrm{T}} M(\omega)^{-1} Q. \tag{4.17}$$

4.2.2 *Identifying the gyration of the waveguide*

The following auxiliary calculation will establish a relation between the gyration of the MO film and the model parameters. The special case of a bare magneto-optical slab is described by equations (4.13a) and (4.13b) for $k_{\mathrm{MO,TM}} = k_{\mathrm{MO,TE}} = 0$. In analogy to equation (4.14), the corresponding matrix form is

$$\begin{bmatrix} W_{\mathrm{MO}}(\omega) & +i\omega k_m \\ -i\omega k_m & W_{\mathrm{MO}}(\omega) \end{bmatrix} \begin{pmatrix} x_{\mathrm{MO}} \\ y_{\mathrm{MO}} \end{pmatrix} = \frac{q_{\mathrm{MO}}}{m} \begin{pmatrix} E_x \\ E_y \end{pmatrix}. \tag{4.18}$$

For small k_m, i.e., for small magnetic fields, the resulting susceptibility is then given by

$$\chi(\omega) = \frac{n\, q_{\mathrm{MO}}^2}{m\, W_{\mathrm{MO}}(\omega)} \begin{pmatrix} 1 & \frac{-ik_m\omega}{W_{\mathrm{MO}}(\omega)} \\ \frac{+ik_m\omega}{W_{\mathrm{MO}}(\omega)} & 1 \end{pmatrix}. \tag{4.19}$$

As discussed in section 2.2.2, for light propagating in z direction, the susceptibility tensor $\chi = \varepsilon - I$ of a MO material can be written as

$$\chi = \begin{pmatrix} \chi_{xx} & +ig \\ -ig & \chi_{yy} \end{pmatrix}, \tag{4.20}$$

where g is the complex magnetic field induced gyration of the material. By comparing the equations (4.19) and (4.20) g can be identified to be

$$g = |g|e^{i\theta} = -\frac{n\omega k_m q_{\mathrm{MO}}^2}{m W_{\mathrm{MO}}(\omega)^2}. \tag{4.21}$$

4.2.3 *Simplified model (3 degrees of freedom)*

Solving equations (4.13a) and (4.13b) for x_{MO} and y_{MO} yields in the limit of a small magnetic influence (i.e., $k_m \ll W_{\mathrm{MO}}$)

$$\begin{aligned} x_{\mathrm{MO}} = &+ \frac{1}{W_{\mathrm{MO}}(\omega)}(m^{-1}q_{\mathrm{MO}}E_x - k_{\mathrm{MO,TM}}x_{\mathrm{TM}}) \\ &- ik_m\frac{\omega}{W_{\mathrm{MO}}(\omega)^2}(m^{-1}q_{\mathrm{MO}}E_y - k_{\mathrm{MO,TE}}y_{\mathrm{TE}}) \end{aligned} \tag{4.22}$$

$$\begin{aligned} y_{\mathrm{MO}} = &+ \frac{1}{W_{\mathrm{MO}}(\omega)}(m^{-1}q_{\mathrm{MO}}E_y - k_{\mathrm{MO,TE}}y_{\mathrm{TE}}) \\ &+ ik_m\frac{\omega}{W_{\mathrm{MO}}(\omega)^2}(m^{-1}q_{\mathrm{MO}}E_x - k_{\mathrm{MO,TM}}x_{\mathrm{TM}}). \end{aligned} \tag{4.23}$$

The equations (4.22) and (4.23) can now be inserted into the equations (4.13c) and (4.13d) to eliminate x_{MO} and y_{MO}. It is reasonable to assume that the MO oscillator couples only weakly to the far field and that the system is mainly driven via the waveguide and the plasmon oscillators. This means that the driving forces of the MO oscillator are assumed to be much weaker than the internal coupling forces ($|m^{-1}q_{\mathrm{MO}}E_x| \ll |k_{\mathrm{MO,TM}}x_{\mathrm{TM}}|$ and $|m^{-1}q_{\mathrm{MO}}E_y| \ll |k_{\mathrm{MO,TE}}y_{\mathrm{TE}}|$). In this limit and by using the equation (4.21), the equations (4.13c) and (4.13d) can be rewritten as

$$\begin{aligned} &(-\omega^2 + \Omega_{\mathrm{TM}}^2 - 2i\Gamma_{\mathrm{TM}}\omega - \frac{k_{\mathrm{MO,TM}}^2}{W_{\mathrm{MO}}(\omega)})x_{\mathrm{TM}} \\ &- ig\frac{mk_{\mathrm{MO,TM}}k_{\mathrm{MO,TE}}}{nq_{\mathrm{MO}}^2}y_{\mathrm{TE}} - k_{\mathrm{P,TM}}x_{\mathrm{P}} = m^{-1}q_{\mathrm{TM}}E_x \end{aligned} \tag{4.24}$$

$$\begin{aligned} &(-\omega^2 + \Omega_{\mathrm{TE}}^2 - 2i\Gamma_{\mathrm{TE}}\omega - \frac{k_{\mathrm{MO,TE}}^2}{W_{\mathrm{MO}}(\omega)})y_{\mathrm{TE}} \\ &+ ig\frac{mk_{\mathrm{MO,TM}}k_{\mathrm{MO,TE}}}{nq_{\mathrm{MO}}^2}x_{\mathrm{TM}} = m^{-1}q_{\mathrm{TE}}E_y. \end{aligned} \tag{4.25}$$

Together with (4.13e), these two equations fully describe the optical system. Hence, the applied approximations led to a reduction to only three equations. Usually, the material resonance of the MO slab is far away from the excitation frequency and the

waveguide frequencies (i.e., $\Omega_{\mathrm{MO}} \gg \Omega_{\mathrm{TM}}, \Omega_{\mathrm{TE}}, \omega$), which means that the terms proportional to $1/W_{\mathrm{MO}}(\omega)$ can be neglected. This results in the following set of equations:

$$(-\omega^2 + \Omega_{\mathrm{TM}}^2 - 2i\Gamma_{\mathrm{TM}}\omega)x_{\mathrm{TM}} - ibe^{i\theta}y_{\mathrm{TE}} \quad - k_{\mathrm{P,TM}}x_{\mathrm{P}} \quad = m^{-1}q_{\mathrm{TM}}E_x \tag{4.26a}$$

$$(-\omega^2 + \Omega_{\mathrm{TE}}^2 - 2i\Gamma_{\mathrm{TE}}\omega)y_{\mathrm{TE}} \quad + ibe^{i\theta}x_{\mathrm{TM}} \qquad\qquad = m^{-1}q_{\mathrm{TE}}E_y \tag{4.26b}$$

$$(-\omega^2 + \Omega_{\mathrm{P}}^2 - 2i\Gamma_{\mathrm{P}}\omega)x_{\mathrm{P}} \qquad\qquad - k_{\mathrm{P,TM}}x_{\mathrm{TM}} = m^{-1}q_{\mathrm{P}}E_x, \tag{4.26c}$$

where $b = |g|\, mk_{\mathrm{MO,TM}}k_{\mathrm{MO,TE}}/nq_{\mathrm{MO}}^2$ and $\theta = \arg(g)$. For an absent driving electrical field, i.e., for $\mathbf{E}_{||} = 0$, the equations above represent a quadratic eigenvalue problem for the eigenfrequencies ω. Obtaining these eigenfrequencies would therefore require to find the roots of a polynomial with degree six, which cannot be accomplished analytically. However, by applying a rotating wave approximation, the quadratic eigenvalue problem can be reduced to a linear eigenvalue problem. This approximation is valid, when the relevant frequencies are in the same range, that is

$$-\omega^2 + \Omega_j^2 \approx (\Omega_j - \omega)2\bar{\Omega}, \qquad j = \mathrm{TM,TE,P}. \tag{4.27}$$

Here, $\bar{\Omega}$ is a constant average frequency close to ω, Ω_{TM} and Ω_{TE}. In this approximation, the equations of motion become

$$(\omega_{\mathrm{TM}} - \omega)x_{\mathrm{TM}} - i\beta e^{i\theta}y_{\mathrm{TE}} \; - \kappa\, x_{\mathrm{P}} \quad = \eta\rho_{\mathrm{TM}}E_x \tag{4.28a}$$

$$(\omega_{\mathrm{TE}} - \omega)y_{\mathrm{TE}} \; + i\beta e^{i\theta}x_{\mathrm{TM}} \qquad\qquad = \eta\rho_{\mathrm{TE}}E_y \tag{4.28b}$$

$$(\omega_{\mathrm{P}} - \omega)x_{\mathrm{P}} \qquad\qquad - \kappa\, x_{\mathrm{TM}} = \eta\rho_{\mathrm{P}}E_x. \tag{4.28c}$$

The following definitions were used: $\beta = b/2\bar{\Omega}$, $\kappa = k_{\mathrm{P,TM}}/2\bar{\Omega}$, $\eta = 1/2m\bar{\Omega}n$, $\rho_j = nq_j$ and $\omega_j = \Omega_j - i\Gamma_j$, with $j = \mathrm{TM,TE,P}$, where n is the oscillator density in the effective medium. When writing the equations above in the matrix form

$$(M_0 + \Delta M - I\omega)\,\mathbf{x} = \eta R\,\mathbf{E}_{||}, \tag{4.29}$$

with $\mathbf{x} = (x_{\mathrm{TM}}, x_{\mathrm{P}}, y_{\mathrm{TE}})^{\mathrm{T}}$ and

$$M_0 = \begin{pmatrix} \omega_{\mathrm{TM}} & -\kappa & 0 \\ -\kappa & \omega_{\mathrm{P}} & 0 \\ 0 & 0 & \omega_{\mathrm{TE}} \end{pmatrix} \tag{4.30}$$

$$\Delta M = \beta e^{i\theta} \begin{pmatrix} 0 & 0 & -i \\ 0 & 0 & 0 \\ +i & 0 & 0 \end{pmatrix} \tag{4.31}$$

$$R = \begin{pmatrix} \rho_{\mathrm{TM}} & 0 \\ \rho_{\mathrm{P}} & 0 \\ 0 & \rho_{\mathrm{TE}} \end{pmatrix}, \tag{4.32}$$

it is evident that we arrived at the equation of motion as utilized in 4.1.

4.3 ON THE PHASE OF THE GYRATION

In section 4.2.3, it was already motivated, that θ is the complex phase of the gyration of the magneto-optical slab. In this section, this interpretation will be supported by electromagnetic perturbation theory [103, 104] based on the assumption that the influence of the magnetic field (represented by ΔM) can be regarded as a small perturbation compared to M_0.

First of all, it is important to note that the presented perturbation theory does not provide the magneto-optical spectra, but only the modifications of the eigenfrequencies due to the applied magnetic field. Since these changes are very small and not of particular interest, they will not be part of further discussion. Instead, the goal is to utilize perturbation theory to link the parameter θ of the oscillator model to the dielectric parameters of the actual nanostructure compounds. For this, the mechanical eigenvalue problem (4.6) will be formulated in the basis of the eigenvectors of the unperturbed matrix M_0. This eigenvalue problem is then compared to the corresponding electromagnetic eigenvalue problem formulated for a given geometry and material composition. The comparison of the two eigenvalue equa-

tions then yields the connection between the phase θ and the material properties of the structure.

Mechanical picture

For zero magnetic field, i.e., in the unperturbed case, equation (4.6) turns into

$$M_0 \mathbf{x}_n^{(0)} = \omega_n^{(0)} \mathbf{x}_n^{(0)}, \tag{4.33}$$

with the eigenfrequencies

$$\omega_{1,2}^{(0)} = \frac{\omega_{\mathrm{TM}} + \omega_{\mathrm{P}}}{2} \mp \sqrt{\kappa^2 + \left(\frac{\omega_{\mathrm{TM}} - \omega_{\mathrm{P}}}{2}\right)^2} \tag{4.34}$$

$$\omega_3^{(0)} = \omega_{\mathrm{TE}} \tag{4.35}$$

and the eigenvectors

$$\mathbf{x}_{1,2}^{(0)} = \begin{Bmatrix} \left[\omega_{\mathrm{P}} - \omega_{\mathrm{TM}} \pm \sqrt{4\kappa^2 + (\omega_{\mathrm{P}} - \omega_{\mathrm{TM}})^2}\right] / 2\kappa \\ 1 \\ 0 \end{Bmatrix}, \qquad \mathbf{x}_3^{(0)} = \begin{pmatrix} 0 \\ 0 \\ 1 \end{pmatrix}. \tag{4.36}$$

The eigenvalue equation of the perturbed case formulated in the basis $A = (\mathbf{x}_1^{(0)}, \mathbf{x}_2^{(0)}, \mathbf{x}_3^{(0)})$ then reads

$$\left[\mathrm{diag}(\omega_1^{(0)}, \omega_2^{(0)}, \omega_3^{(0)}) + \Delta\tilde{M}\right] \mathbf{c}_n = \omega_n \mathbf{c}_n, \tag{4.37}$$

where

$$\Delta\tilde{M} = A^{-1} \Delta M A \tag{4.38}$$

$$\mathbf{c}_n = A^{-1} \mathbf{x}_n. \tag{4.39}$$

Electromagnetic picture

In the electromagnetic picture, the eigenmodes have to fulfill the wave equation

$$\nabla \times \nabla \times \mathbf{E}_n = \frac{\omega_n^2}{c^2} (\varepsilon + \Delta\varepsilon) \mathbf{E}_n. \tag{4.40}$$

Here $\varepsilon(\mathbf{r};\omega)$ is the space dependent material permittivity tensor of the structure for zero magnetic field and $\Delta\varepsilon(\mathbf{r};\omega)$ is a small magnetic field induced perturbation. In the case of a magnetic field pointing in z-direction, within the MO slab this perturbation is given by

$$\Delta\varepsilon = \begin{pmatrix} 0 & ig & 0 \\ -ig & 0 & 0 \\ 0 & 0 & 0 \end{pmatrix}, \tag{4.41}$$

whereas $\Delta\varepsilon$ is zero outside the MO slab. Knowing the eigenfrequencies and eigenvectors for perturbation $\Delta\varepsilon = 0$, we can expand the Green's dyadic of the unperturbed system in terms of its resonances, provided that the fields are normalized correctly [103]. Then, we can consider the contribution in equation (4.40) proportional to $\Delta\varepsilon$ as a source of the unperturbed system. Neglecting the influence of Rayleigh anomalies as well as material dispersions, and assuming that we can decompose the new eigenstates in terms of the unperturbed eigenstates as

$$\mathbf{E}_n(\mathbf{r}) = \sum_m c_{mn}\mathbf{E}_m^{(0)}(\mathbf{r}), \tag{4.42}$$

we can derive the following system of equations for the expansion coefficients:

$$c_{mn}(\omega_n - \omega_m^{(0)}) = \omega_n \sum_k D_{mk}c_{kn}, \tag{4.43}$$

with

$$D_{mk} = \frac{1}{2}\int d^3r\ \mathbf{E}_m^{(0)}(\mathbf{r})\,\Delta\varepsilon\,\mathbf{E}_k^{(0)}(\mathbf{r}). \tag{4.44}$$

After restricting the left part of equation (4.43) to the fundamental plasmon and waveguide modes, it can be written in the compact matrix form

$$\mathbf{c}_n\omega_n - \mathrm{diag}(\omega_1,\omega_2,\omega_3)\mathbf{c}_n = \omega_n D\mathbf{c}_n \tag{4.45}$$

with D being a 3×3 matrix containing the overlap integrals of the fields and the perturbation as defined in equation (4.44). Since

the components of D are small, equation (4.45) can be approximated as

$$(I + D)\mathrm{diag}(\omega_1^{(0)}, \omega_2^{(0)}, \omega_3^{(0)})\ \mathbf{c}_n = \omega_n \mathbf{c}_n. \tag{4.46}$$

The left hand side of this equation simplifies due to the special form of the eigenmodes of the unperturbed system: The TM polarized waveguide-plasmon-polariton modes (low energy branch ω_1 and high energy branch ω_2) have zero electric field in y-direction, whereas the TE waveguide mode (ω_3) only has a y-component [48, 49].

Linking θ to the gyration

If our mechanical model correctly reflects the physical properties of the nanostructure compound, equation (4.46) and (4.37) should be formally equivalent, resulting in the following relation:

$$D\ \mathrm{diag}(\omega_1, \omega_2, \omega_3) = \Delta\tilde{M}. \tag{4.47}$$

Together with equation (4.38), the explicit form of (4.47) reads

$$\begin{pmatrix} 0 & 0 & D_{13}\omega_3 \\ 0 & 0 & D_{23}\omega_3 \\ -D_{13}\omega_1 & -D_{23}\omega_2 & 0 \end{pmatrix} = i\beta e^{i\theta} \times \begin{bmatrix} 0 & 0 & -\kappa/\kappa' \\ 0 & 0 & +\kappa/\kappa' \\ (\omega_\mathrm{P} - \omega_\mathrm{TM} + \kappa')/2\kappa & -(\omega_\mathrm{TM} - \omega_\mathrm{P} + \kappa')/2\kappa & 0 \end{bmatrix}, \tag{4.48}$$

with the abbrevation $\kappa' = \sqrt{4\kappa^2 + (\omega_\mathrm{P} - \omega_\mathrm{TM})}$ and the overlap integrals

$$D_{13} = -D_{31} = ig\frac{1}{2}\int d^3r\ E_x^{(1)} E_y^{(3)} \tag{4.49a}$$

$$D_{23} = -D_{32} = ig\frac{1}{2}\int d^3r\ E_x^{(2)} E_y^{(3)}, \tag{4.49b}$$

where the integration volume is restricted to the slab waveguide.

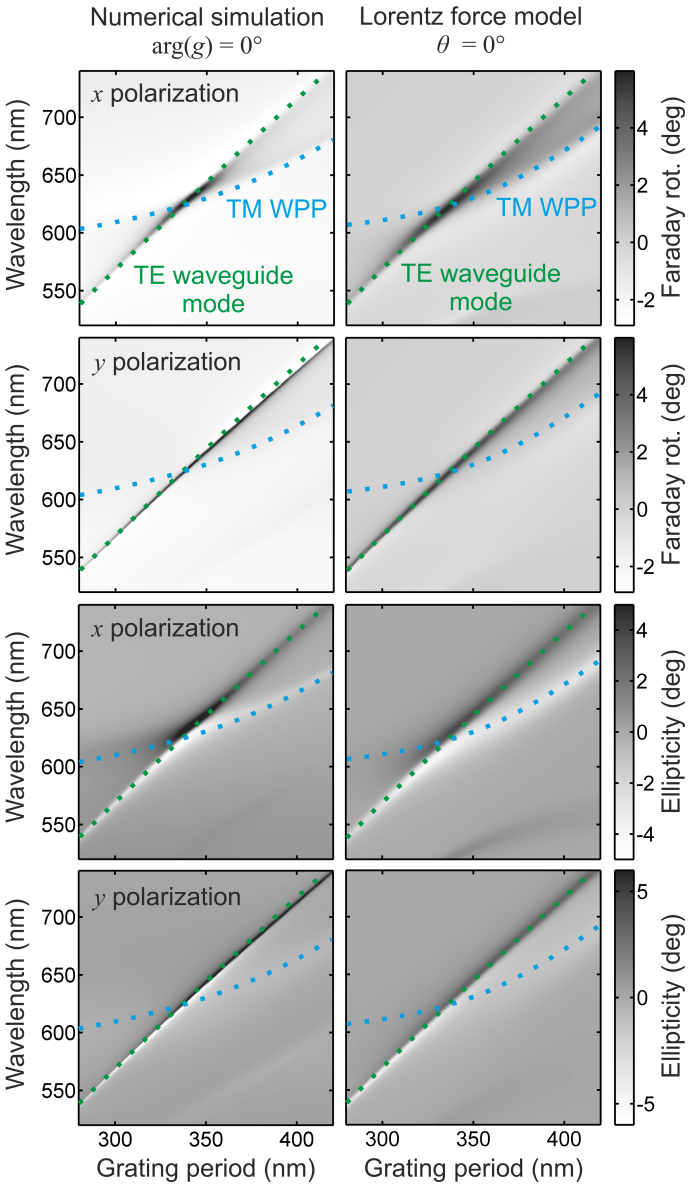

Figure 4.6: Dispersion of MO response obtained by full numerical simulations (left panels) and the presented model (right panels) for $\theta = 0°$.

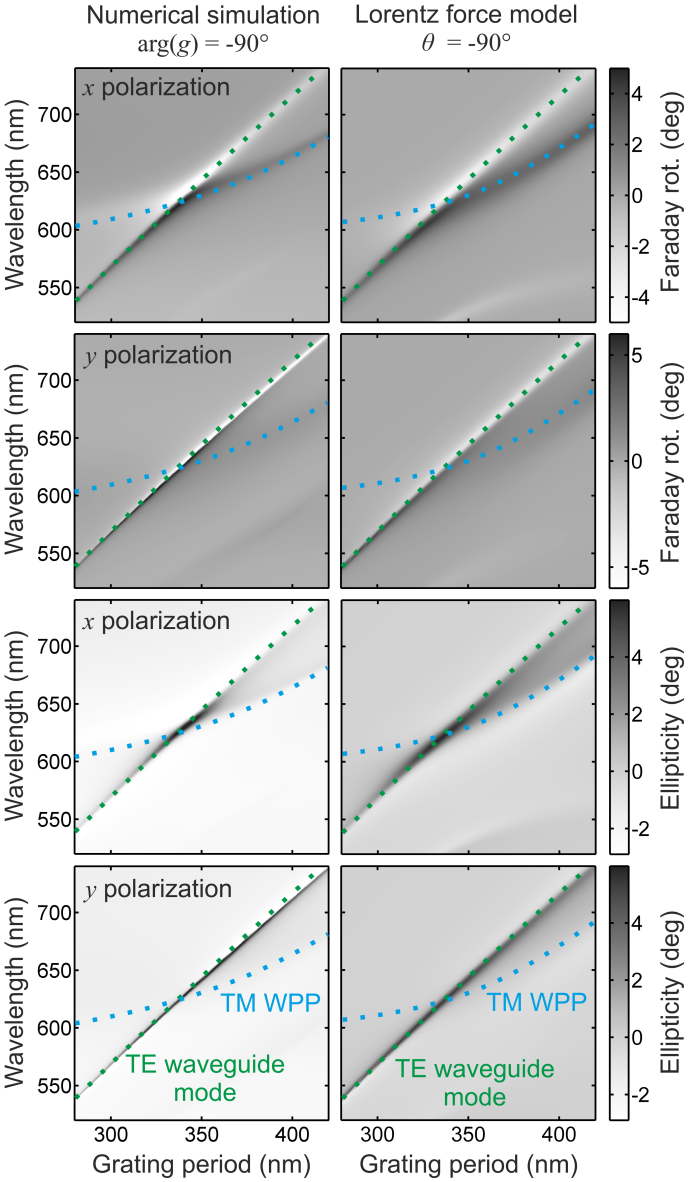

Figure 4.7: Dispersion of MO response obtained by full numerical simulations (left panels) and the presented model (right panels) for $\theta = -90°$.

Since the quantities β and κ are defined to be real, and the complex phase of $\{\omega_{\mathrm{TE}}, \omega_{\mathrm{TM}}, \omega_{\mathrm{P}}\}$ and thus of κ' can be assumed to be small, the phase θ is predominantly determined by the phase of g and the phases of the overlap integrals in equation (4.49). Scattering matrix simulations for grating periods within the range presented in section 4.1 have shown that the contributions of the overlap integrals to the phase θ are also negligible. Hence, as already motivated in sections 4.2.2 and 4.2.3, the model parameter θ can be interpreted as the phase of the gyration of the magneto-optical material:

$$\theta = \arg(g)\,. \tag{4.50}$$

In section 4.1, the MO spectra were simulated and modeled for constant $\theta = \arg(g) = -45\,\mathrm{deg}$, which is a reasonable assumption for typically used MO materials such as EuSe [53] and bismuth iron garnet [47] in the red and near-IR. Here, exemplary results for further values of $\arg(g)$ and θ are provided. In figure 4.6 the simulation and modeling results for $\theta = \arg(g) = 0\,\mathrm{deg}$ are displayed, whereas figure 4.7 shows the corresponding plots for $\theta = \arg(g) = -90\,\mathrm{deg}$. Besides θ, all model parameters were set to the same value as for the structure in section 4.1. The good agreement between numerical simulation and modeling results confirms the connection between θ and the gyration, given by (4.50). It should be noted that increasing or decreasing the parameter θ by 180 deg leads to equal results as flipping the sign of β, which corresponds to the inversion of the magnetic field.

4.4 CONCLUSION

In summary, the dispersion of the MO response of hybrid magnetoplasmonic waveguides can now be understood in the picture of a simple oscillator model including the nonreciprocal Lorentz force. In the case of a weak influence of the Lorentz force, analytical expressions for the optical response were obtained, which confirm previous numerical findings. Importantly, the spectral line shape of the MO response is fully determined by the optical

properties of the system for zero magnetic field. Only the overall magnitude of the MO response is determined by the applied magnetic field.

The theory in this chapter provides the understanding required to further develop hybrid magnetoplasmonic systems in highly integrated optics, demanding actively controlled optical modulation [22], magnetic field sensing [20, 21], refractive index sensing [107], and optical isolation [14–19]. It should also be mentioned that the presented findings can not only help to understand and optimize existing sample geometries, but can also be transferred to other geometries, such as 2D plasmonic gratings. Furthermore, by removing all plasmonic oscillators, the case of a purely dielectric grating-waveguide combination can be realized.

In chapter 5 the presented model will be applied to a system consisting of an EuS thin film and an embedded plasmonic grating. By means of the model, it will be shown, that in the case of weak coupling between the plasmonic and waveguide resonance, the classical optical analog of electromagnetically induced transparency and absorption can be realized. Moreover, the model will be of fundamental importance to understand why the corresponding magneto-optic response in such a system is so exceptionally large.

In prospect of non-linear magnetoplasmonics, the presented model could also be of fundamental relevance. Although the described model is fully linear, a non-linear extension would be straight-forward by adding higher order coupling terms [108].

5

GIANT FARADAY EFFECT VIA INDUCED ABSORPTION

In this chapter[1] a new hybrid magnetoplasmonic thin film structure will be demonstrated, that resembles the classical optical analog of electromagnetically induced absorption. In transmission geometry the gold nanostructure embedded in an EuS film induces giant Faraday rotation of up to 14° for a thickness of less than 200 nm and a magnetic field of 5 T at $T = 20$ K. By varying the magnetic field from -5 T to $+5$ T, a rotation tuning range of over 25° is realized. As this is only a factor of three away from the Faraday isolation requirement, the demonstrated concept could lead to highly integrated, nonreciprocal photonic devices for optical isolation, light modulation, and optical magnetic field sensing.

5.1 REALIZATION WITH EuS-Au HYBRID SYSTEMS

In the last two chapters it was demonstrated how the magneto-optic (MO) response of a dielectric thin film is enhanced by the attachment of a plasmonic grating. This technique also allows the amplified MO response to be spectrally tailored by tuning the grating parameters. However, the MO performance of such a system is limited by the low Q factor of the plasmon resonances in the grating. In the following, it will be shown that this limitation can be lifted elegantly by a novel approach, which is based on a classical optical analog of electromagnetically induced absorption (EIA) [51, 52]. Here, a strongly damped plasmon oscillation is weakly coupled to a narrow linewidth waveguide res-

1 Major parts of this chapter were published in the article [109] under the Creative Commons Attribution 4.0 International license. The author of this dissertation is also first author of the referenced article.

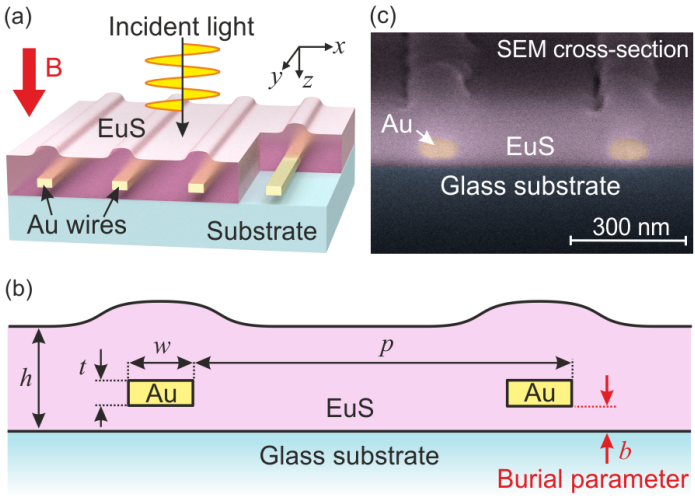

Figure 5.1: (a),(b) Schematic drawing of the sample geometry. p, nanowire period; t, w gold nanowire thickness and width. The wires are buried with a distance b between the glass substrate and their lower edge. The nominal thickness of the EuS magneto-optical waveguide is h, which is increased near the position of the gold nanowires. (c) Colorized scanning electron micrograph of the sample cross section. The samples are measured at $T = 20\,\mathrm{K}$.

onance with a phase delay, leading to constructive interference. By tuning this coupling carefully, a high-Q absorptive hybrid mode is realized, which can be used to resonantly amplify the Faraday rotation response. Furthermore, the EIA mechanism allows to utilize the high oscillator strength of the plasmonic resonance, leading to an efficient coupling of the incident light into the structure without reducing the effective Q factor due to the broad plasmonic resonance as was the case in previous approaches [45, 47, 53]. Although being only less than 200 nm thick, the presented novel structure design exhibits an order of magnitude better rotation capability than previous approaches that only resulted in fractions of degree rotation [35–37, 46, 47].

Furthermore, for low magnetic fields, the presented technique still yields rotation angles that were only achievable with 20 times stronger field strength in previous approaches [53]. The perfor-

mance of the thin film structure is only a factor of 3 away from the 45° that are required for building a Faraday isolator which usually requires MO media with a thickness on the order of centimeters. The first demonstration of plasmonic resemblances of EIA [110, 111] and its related effect, namely electromagnetically induced transparency (EIT) [112–114], triggered significant attention. The special dispersion properties of such systems are known to facilitate plasmonic sensing with narrow linewidths [115–117] as well as slow light [118–120] and delay lines [121, 122]. Furthermore, there have been extensive studies on enhanced nonlinear response [123, 124] in such systems. Here, it will be demonstrated that the EIA-like optical dispersion in the presented system also facilitates a giant MO response. While in EIT the light within a narrow spectral band passes through the sample, in the case of EIA real material polarization is excited within a narrow spectral region.

Another important aspect of the presented approach is the introduction of EuS as a new dielectric material for hybrid magnetoplasmonics. At low temperatures, EuS possesses an exceptionally large Verdet constant in combination with a high saturation magnetic flux density, resulting in a potentially very strong MO response [68, 93]. Furthermore, it is transparent in the visible, qualifying it for the utilization in Faraday geometry. While EuS possesses as similar refractive index and absorption coefficient as EuSe [68, 93], EuS is significantly cheaper and already exhibits a stronger MO response at low magnetic field strengths. Further information about the temperature dependence of the EuS material parameters can be found in section 5.2. Despite the need for low temperatures, EuS is well suited for studying plasmonic MO model systems, as it combines the above-mentioned benefits with simple fabrication by physical vapor deposition. This allows for the realization of complex hybrid magnetoplasmonic structure geometries, which are challenging when fabricated with commonly used magneto-optic materials, such as bismuth iron garnet [70] or yttrium iron garnet [125]. The reason is that the deposition of garnet films is a sophisticated process that usually

involves pulsed laser deposition and high-temperature annealing that could damage any underlying plasmonic structures.

The utilized structure geometry is depicted in the figures 5.1a and 5.1b. It consists of an EuS thin film with an embedded Au nanowire grating. The EuS film is magnetized by an external magnetic field in the z direction, which is also the direction of propagation of the incident light. The structure is fabricated in a three-step process. First, the bottom layer of the EuS film with thickness b is evaporated onto the glass substrate by physical vapor deposition. After that, the gold wire grating with thickness t, width w, and period p is structured via electron beam lithography. In the last step, an EuS film with thickness $(h - b)$ is evaporated. This results in an EuS-Au thin film structure with a slightly corrugated upper surface. Figure 5.1c shows a colored scanning electron micrograph of the cross section of such a structure with geometry parameters $p = 490\,\text{nm}$, $t = 33\,\text{nm}$, $w = 85\,\text{nm}$, $h = 139\,\text{nm}$, and $b = 33\,\text{nm}$. For the case of $b = 0$, the non-MO dispersion properties of such a metal-dielectric hybrid structure have previously been analyzed in detail by Zentgraf *et al.* [126]. Because of the presence of the glass substrate with a higher refractive index than the air above the sample, the x component of the electric field of the TM waveguide mode is concentrated in the upper part of the EuS waveguide. Hence, the coupling between plasmon and TM waveguide mode is weak in comparison to the case where the metal wires are attached on top. In the work by Zentgraf *et al.* it was also demonstrated that this weak coupling can lead to the classical analog of the quantum mechanical effect of electromagnetically induced transparency, resulting in a narrow transmission peak on top of a broad transmission dip for x-polarized incident light.

Exploiting the regime of induced absorption

It will now be demonstrated that by increasing the burial parameter b in the hybrid system, the phase between the plasmonic mode and the TM waveguide mode can be tuned such that the

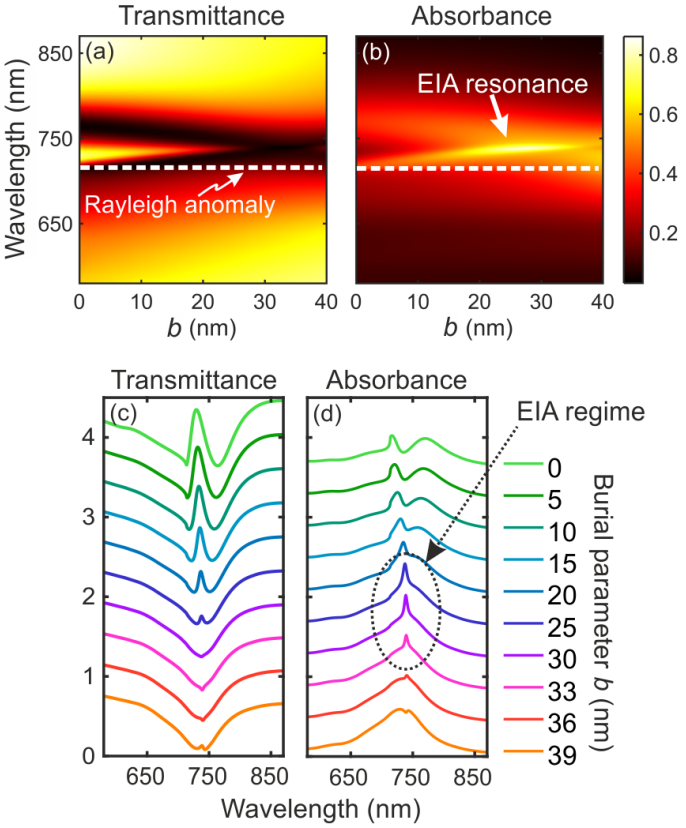

Figure 5.2: (a),(b) Simulated transmittance and absorbance ($1 - T - R$ with T and R denoting transmittance and reflectance, respectively) for x-polarized incident light and different burial parameters b. For increasing b there is a gradual transition from the regime of induced transparency to induced absorption. The white dotted line indicates the Rayleigh anomaly. (c),(d) Slice cuts for a clearer view on the line shapes of the spectra. The oval indicates the EIA regime, characterized by very sharp induced absorption peaks.

system undergoes a transition from EIT-like to EIA-like behavior [110, 111]. Figure 5.2 displays the simulated transmittance and absorbance spectra for x-polarized incident light and different burial parameters b. The simulations have been carried out using the Fourier modal method for anisotropic materials [127]. Our

implementation is based on a scattering matrix algorithm [75], which has been improved by adaptive spatial resolution [105] to enable an efficient derivation of optical properties of metallodielectric systems. The refractive index of the substrate is assumed to be 1.456, and for the gold wires the permittivity data by Johnson and Christy [92] are used. In the investigated wavelength range, the refractive index of EuS is approximately 2. The utilized material model parameters for EuS can be found in section 5.2.1. The geometry parameters were set to $p = 490\,\text{nm}$, $t = 33\,\text{nm}$, $w = 85\,\text{nm}$, and $h = 139\,\text{nm}$. In all simulations the bumps in the EuS film above the Au wires are approximated by a rectangular shape with thickness t and a width of $2w$. As expected [126], for small values of b, the transmittance spectrum exhibits the characteristic EIT line shape with a broad, mainly plasmon-induced dip and a narrow, mainly TM waveguide-induced peak. For increasing values of b, this effect is reversed and the sharp waveguide feature flips around, resulting in a sharp absorbance peak that is characteristic for an EIA-like system. At 715 nm, the spectra are slightly distorted due to the Rayleigh anomaly [49]. The transition of the spectra with increasing b can be understood in the picture of coupled Lorentz oscillators introduced by Taubert *et al.* [111]: Here, a strongly damped Lorentz oscillator (in this case the plasmon) and a less damped Lorentz oscillator (in this case the TM waveguide mode) are coupled via a complex coupling constant that includes an additional phase delay. It was shown that by changing the phase of the coupling constant, the optical response of the system turns from EIT-like to an EIA-like behavior. In the present case, this behavior is particularly pronounced for b between 25 and 36 nm (see figure 5.2d, oval area). Furthermore, by changing the distance between the wire grating and the substrate, the coupling phase can be changed. As in other cases of plasmonic EIT and EIA, the reflection behavior of the system also changes with the coupling phase, which leads to the situation that the EIT coupling regime can be observed most pronounced in the transmittance spectrum, whereas the EIA case can be identified best in the absorbance spectrum [111]. In sec-

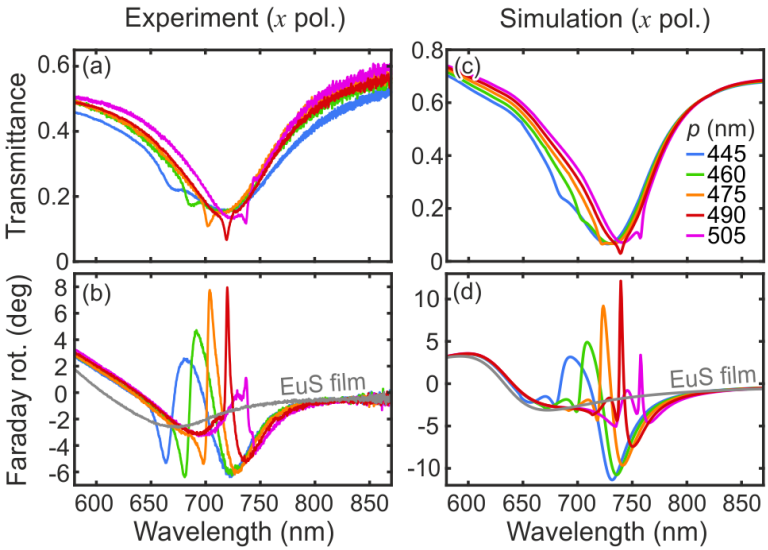

Figure 5.3: The left-hand column displays the measured transmittance (a) and Faraday rotation (b) for x-polarized incident light for a wire width of 85 nm, burial parameter $b = 33$ nm, and different grating periods. The experimental data agree with the performed simulation shown in the right-hand column (c),(d).

tion 5.3, there will be an extended discussion on interpreting the presented magnetoplasmonic system in the picture of coupled oscillators.

For a burial parameter of $b = 33$ nm, the EIA coupling regime manifests itself also in the transmittance spectrum in the form of a small dip (see figure 5.2c). For this case the relation between the EIA-like behavior and the MO response was investigated experimentally. The figures 5.3a and 5.3b display the measured transmittance and Faraday rotation spectra for x-polarized incident light and different grating periods p. The measurements are performed at 20 K and a magnetic field of 5 T in the z direction. The Faraday rotation was measured with a rotating analyzer setup where the incident polarization state was prepared using a polarizer inside the cryostat (see section 2.7). For a period of 490 nm, the sharp EIA feature is best centered with respect to the broad,

mainly plasmonic, transmittance feature. For the same grating period, at the spectral position of the EIA resonance, the Faraday rotation exhibits a sharp maximum of about 8°, which is a substantial rotation enhancement compared to a bare EuS film with thickness $h = 139\,\text{nm}$ (gray curve). This behavior can be understood in the following way: For wavelengths close to the narrow EIA resonance, the system acts as a resonator with a relatively high Q factor, implying multiple vertical round-trips of the light through the MO material before it is coupled out in z direction. Due to Lorentz non-reciprocity, the polarization rotation adds up for each propagation cycle, resulting in an enhanced rotation compared to a single pass through the EuS film. Furthermore, the EIA mechanism allows utilizing the high oscillator strength of the plasmonic resonance, leading to an efficient coupling of the incident light into the structure without reducing the effective Q factor due to the broad plasmonic resonance as was the case in previous approaches [45, 47, 53]. As such, the plasmonic EIA mechanism provides an elegant way to greatly increase the interaction between the incident light and the MO material. In section 5.3 the connection between the EIA dispersion and Faraday rotation enhancement will be discussed in further detail by means of a coupled oscillator model. The measurement is also in good agreement with the full numerical simulation displayed in the figures 5.2c and 5.2d. In the measured wavelength region, the Faraday rotation of EuS shows a notable wavelength dependence due to a material resonance (see gray line). Hence, in order to obtain realistic simulation results, the material dispersion of EuS is modeled with a MO Lorentz oscillator (see section 2.3.1). The free model parameters are fitted such that the measured MO response of a bare EuS film matches the simulated MO response in the wavelength range of interest between 650 and 850 nm. More details on the EuS permittivity model can be found in section 5.2.1. The discrepancy between the measured and simulated Faraday rotation below 650 nm is due to the limited model accuracy in this range. In the transmittance spectra, the grating-induced Rayleigh anomaly is barely visible. For example, for $p = 490\,\text{nm}$

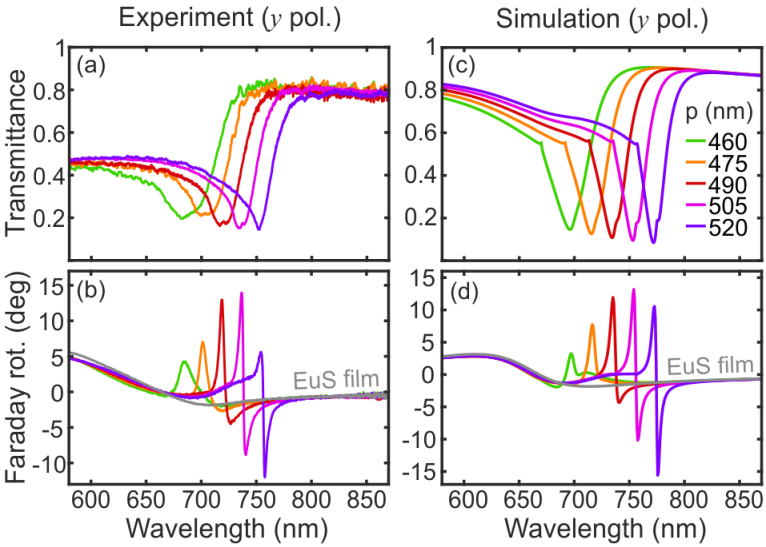

Figure 5.4: The left-hand column displays the measured transmittance (a) and Faraday rotation (b) for y-polarized incident light for a wire width of 75 nm, burial parameter $b = 33$ nm, and different grating periods p. The experimental data agree well with the performed simulation shown in the right-hand column (c),(d). For a period of 505 nm, the Faraday rotation reaches values of up to 14°.

it occurs at 715 nm and is most visible in the simulated Faraday rotation, where it manifests itself as a small kink. However, the Rayleigh anomaly has no major influence on the Faraday rotation enhancement as it is well separated from the enhancement by the EIA resonance.

Also for y-polarized incident light, large Faraday rotation angles can be realized. This is illustrated by the figures 5.4a and 5.4b, which depict the corresponding transmittance and Faraday rotation spectra for a sample geometry with $t = 33$ nm, $w = 75$ nm, $h = 139$ nm, $b = 33$ nm, and different grating periods p. Since a direct excitation of the plasmon resonance and TM waveguide resonance is only possible for x-polarized light, they have no discernable influence on the transmittance line shape. However, as the x- and y-polarized eigenmodes are coupled via

the magnetic field, the Faraday rotation spectrum for y-polarized incidence is strongly influenced by the x-polarized eigenmodes (and vice versa) [102], which results in strongly enhanced Faraday rotation also for y-polarized incidence. Furthermore, this behavior will be discussed in more detail in section 5.3. For a grating period of 505 nm, the Faraday rotation reaches values of up to 14° at a transmittance value of 17%. Given the thin structure profile of below 200 nm, this is a giant Faraday rotation value and only a factor of 3 away from a Faraday isolator. Again, the measurement results are in good agreement with the numerical simulations plotted in the figures 5.4c and 5.4d, except that the Rayleigh anomalies (kinks in the left shoulders of the transmittance spectra) are washed out in the measurement. This happens certainly due to sample roughness and limited fabrication accuracy. As in the case of x-polarized incidence, the Rayleigh anomalies are well separated from the Faraday rotation enhancement feature and have no significant influence on the Faraday rotation spectra.

Influence of magnetic field strength

Furthermore, since the rotation angle scales with the applied magnetic field, the presented structure offers an impressive polarization tuning range of over 25°. This is indicated in figure 5.5a, where the Faraday rotation spectra are plotted for different magnetic field strengths ranging from -5 to $+5$ T. The spectra for inverted magnetic fields exhibit almost perfectly mirror symmetric shapes. Any deviations from absolute mirror symmetry can be explained by a slight misalignment between the gold wires and the incident polarization. Figure 5.5b shows a close-up of the Faraday rotation enhancement feature for lower magnetic field strengths that can be realized easily using standard permanent magnets [128]. Even for magnetic fields as low as 250 mT, the Faraday rotation still reaches values of up to 4.9°. This is a similar rotation performance as was previously realized for a 220-nm thick hybrid structure based on EuSe, however, only with 20

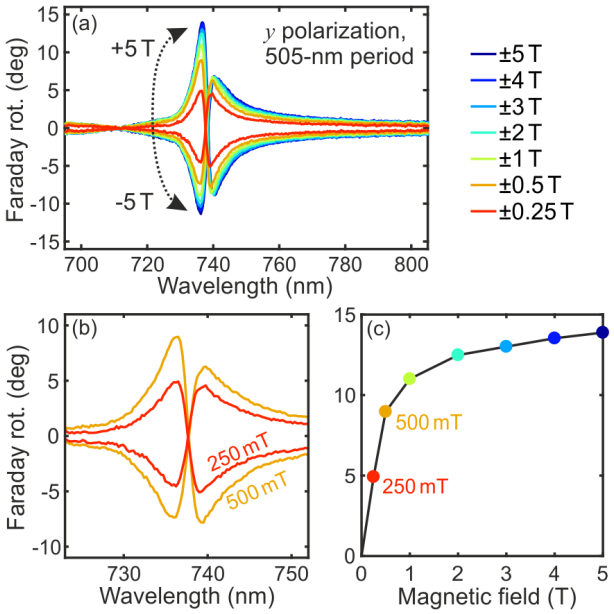

Figure 5.5: (a) Measurement of the magnetic field dependence of the polarization rotation for a period of 505 nm. (b) Closer view on the rotation spectra for weak magnetic fields. Already for 250 mT the Faraday rotation reaches values of over 4°. (c) Saturation behavior of the Faraday rotation at 737 nm.

times larger magnetic fields [53]. Figure 5.5c displays the Faraday rotation at 737 nm as a function of applied magnetic field and illustrates the saturation behavior. Up to 500 mT the rotation angle increases linearly with the applied magnetic field, whereas for larger fields saturation sets in and the response curve flattens out.

Simulation of the ellipticity spectra

As the utilized measurement setup does not allow for measuring the ellipticity spectra, in the following, the numerically simulated ellipticity spectra are provided. Figure 5.6 displays the ellipticity spectra of the sample geometries with 85 and 75 nm wire width.

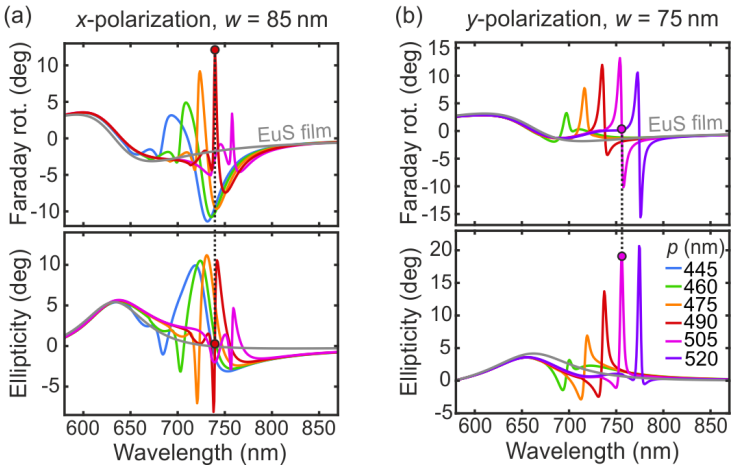

Figure 5.6: Simulated Faraday rotation and ellipticity spectra corresponding to the sample geometries with 85 nm wire width (a) and 75 nm wire width (b).

In the first case, a grating period of 490 nm results in the largest Faraday rotation peak. At its center wavelength, the corresponding ellipticity is close to zero. This behavior is consistent with the following rule of thumb, originating from the Kramers-Kronig relations [54]: A symmetric Faraday rotation peak usually corresponds to asymmetric (s-shaped) ellipticity spectrum with a zero-crossing at the center wavelength of the rotation peak. On the other hand, a symmetric ellipticity peak corresponds to s-shaped Faraday rotation spectrum with the zero crossing at the center wavelength of the ellipticity peak. For example, the latter behavior is exhibited for a wire width of 75 nm, and a period of 505 nm, as illustrated in figure 5.6b.

On the sample anisotropy

Since the utilized magnetoplasmonic structure geometry is anisotropic, in general, the optical response for x- and y-polarized light is different. To illustrate this, figure 5.7 shows a comparison of the transmittance and Faraday rotation for the

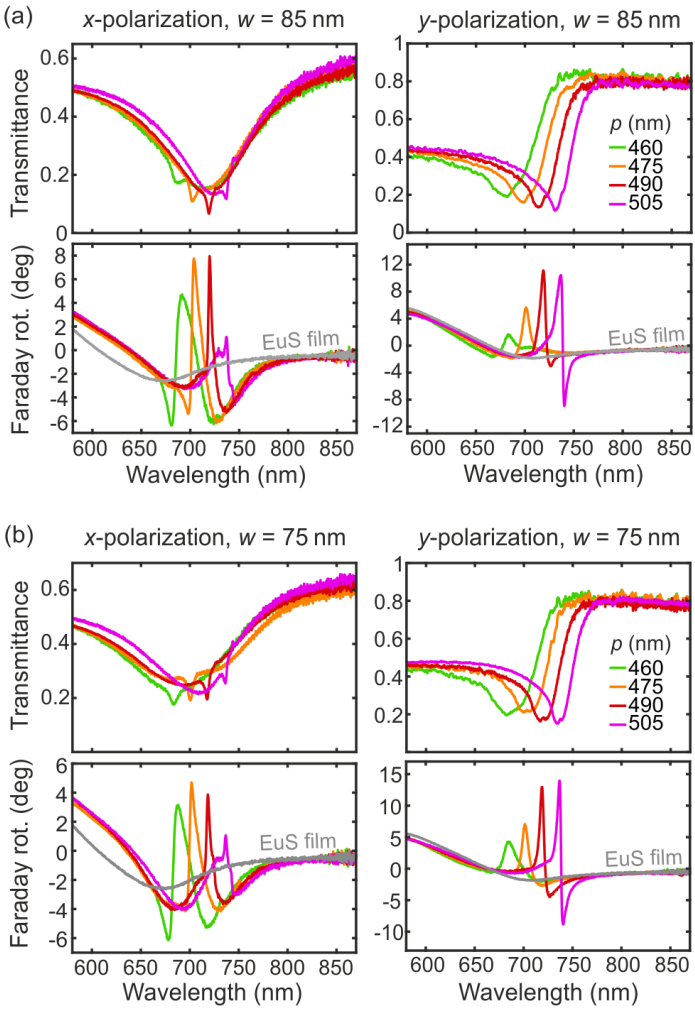

Figure 5.7: Comparison of the transmittance and Faraday rotation spectra for different incident polarizations. (a) 85 nm wire width. (b) 75 nm wire width.

same geometry but different polarizations of the incident light. Figure 5.7a corresponds to a wire width of 85 nm, whereas figure 5.7b shows the spectra for the 75 nm wide gold wires. It can be seen that for the wavelengths of largest Faraday rotation, the

transmittance for the two polarization directions is different. This transmittance difference results in some minor reciprocal contribution to the overall polarization rotation. However, since the Faraday rotation is well below 45°, this effect only has a negligible contribution to the overall polarization rotation.

Furthermore, as already mentioned above, although the EIA-resonance is not visible in the absorbance spectra for y-polarized light, the Faraday rotation rotation enhancement tends to be largest for this polarization direction. This can be understood in the picture of the oscillator model in section 5.3, where it will be shown that the EIA-resonance enters in both off-diagonal elements of the effective susceptibility of the system. The difference in magnitude originates from the different effective refractive indices of the two polarization directions.

5.2 EuS material properties

In this section, the most relevant material properties of EuS are summarized. This includes the material permittivity utilized in the numerical simulations in section 5.1, and a discussion of the temperature dependence of the optical properties.

5.2.1 *EuS permittivity tensor*

In the performed numerical simulations, it was assumed that the EuS film possesses a permittivity of the form

$$\varepsilon = \begin{pmatrix} \varepsilon_{11} & +\varepsilon_{12} & 0 \\ -\varepsilon_{12} & \varepsilon_{11} & 0 \\ 0 & 0 & \varepsilon_{11} \end{pmatrix} \tag{5.1}$$

where the diagonal elements have been modeled using the relation (2.53a):

$$\varepsilon_{11} = \varepsilon_\infty + \frac{\omega_q^2}{\Omega^2 - \omega^2 - 2i\Gamma\omega}. \tag{5.2}$$

The free parameters were fitted to ellipsometry and transmission measurements in the relevant wavelength range between 650 nm

and 850 nm. From this, $\Omega = 2.77 \cdot 10^{15} s^{-1}$, $\Gamma = 2 \cdot 10^{14} s^{-1}$, $\omega_q = 4 \cdot 10^{14} s^{-1}$, and $\varepsilon_\infty = 4.125$ was obtained. This translates to a refractive index ranging from 2.016 to 2.049. The off-diagonal elements of EuS were modeled using the relation

$$\varepsilon_{12} = \frac{i\beta\omega\omega_q^2}{(\Omega^2 - \omega^2 - 2i\Gamma\omega)^2} \,, \tag{5.3}$$

which possesses the same algebraic form as the relation (2.53b). In the standard derivation of this formula, $\beta = be^{i\theta}$ is a parameter proportional to the magnetic field and is assumed to be purely real ($\theta = 0, 180°$). For a bulk magneto-optic material, this leads to a Faraday rotation spectrum of diamagnetic type [54]. However, as it was discussed in section 2.3.2, many magneto-optic materials, such as EuS, rather exhibit a paramagnetic Faraday rotation spectrum, which has a similar form as the ellipticity spectrum corresponding to a diamagnetic Faraday rotation spectrum. It should be noted, that here the terms paramagnetic and diamagnetic are not related to the magnetic susceptibility, but rather to the conventional classification of Faraday rotation mechanisms. The formula above can also be used to model the magneto-optic response of the paramagnetic type phenomenologically, while maintaining consistency with the Kramers-Kronig relations. This is achieved for $\theta = 90°$ and $\theta = 270°$. Furthermore, other values of θ lead to an intermediate situation. The free model parameters in ε_{12} were fitted such that the measured MO response of a bare EuS film at 5 T matches the simulated MO response in the wavelength range of interest between 650 nm and 850 nm. For the EuS film in the structure corresponding to figure 5.3, the following parameter set was obtained: $\Omega = 2.97 \cdot 10^{15} s^{-1}$, $\Gamma = 6 \cdot 10^{14} s^{-1}$, $\omega_p = 9 \cdot 10^{14} s^{-1}$, $\theta = 90°$, and $\beta = 8 \cdot 10^{14} s^{-1}$. The EuS film for the structure corresponding to figures 5.4 and 5.5, showed a slightly different Faraday rotation spectrum resulting in the parameter set $\Omega = 3.11 \cdot 10^{15} s^{-1}$, $\Gamma = 6 \cdot 10^{14} s^{-1}$, $\omega_p = 9 \cdot 10^{14} s^{-1}$, $\theta = 130°$, and $\beta = 9 \cdot 10^{14} s^{-1}$.

5.2.2 *On the influence of temperature*

In general, the optical properties of the materials constituting the presented nanostructures can change with temperature. In previous works, the temperature dependencies of the involved materials have been studied in great detail: Below $T_c = 16.6\,\mathrm{K}$ EuS is in the ferromagnetic phase whereas above T_c it is in the paramagnetic phase [129]. In the measured wavelength range, between T_c and room temperature, the refractive index of EuS changes by less than 1% [68] and also the absorption coefficient of EuS remains almost constant [93]. In this temperature regime also the changes in the optical constants of both Au [130] and the fused silica substrate [131] can be neglected. Furthermore, between 0 K and T_c the gyration of EuS stays constant, whereas at $T = T_c$ it starts to drop inversely proportional with temperature [63]. For example, at 100 K this results in 10% of the Faraday rotation observed at $T = 20\,\mathrm{K}$.

In conclusion, the dispersion of the eigenmodes and, thus, the transmission behavior would not significantly change for an increasing temperature while the Faraday rotation of the nanostructure would decrease proportionally with the Faraday rotation of pure EuS.

5.3 HARMONIC OSCILLATOR MODELING

To obtain further insight into the connection between EIA-like modal coupling and the enhancement of the magneto-optic response, it is useful to view the presented magnetoplasmonic system in the picture of coupled oscillators, as depicted in figure 5.8a. This oscillator scheme was originally introduced in reference [102] and is now modified in analogy to the non-magneto-optic model by Taubert *et al.* to account for EIA [111]. In this very simple model, the magnetoplasmonic system is described using two charged oscillators that are driven by the external light field: The oscillator on the right-hand side represents the plasmonic excitation, and its movement is restricted to the x direction, as

the plasmonic resonance can only be excited for x-polarized light. The second oscillator is associated with the waveguide excitations inside the MO slab. This oscillator can be displaced both in the x and y direction, which corresponds to the excitation of TM and TE polarized waveguide modes respectively. As discussed by Taubert *et al.*, it is crucial for realizing the coupling regime of EIA that the coupling between the two contributing oscillators includes a retardation phase [110]. Hence, the coupling between plasmon and TM waveguide is modeled with a complex coupling constant $\tilde{\kappa} = \kappa \exp(i\phi)$, with ϕ as the phase. The influence of the applied static magnetic field is taken into account via the Lorentz force acting on the 2D waveguide oscillator. The resulting electric susceptibility associated with this oscillator system is given by [102]

$$\chi(\omega) = \begin{pmatrix} \chi_x & +\chi_{xy} \\ -\chi_{xy} & \chi_y \end{pmatrix} = \eta R^T M^{-1} R, \tag{5.4}$$

where the matrices

$$M = \begin{pmatrix} \Omega_{\mathrm{TM}} & -\kappa e^{i\phi} & -i\beta \\ -\kappa e^{i\phi} & \Omega_{\mathrm{P}} & 0 \\ +i\beta & 0 & \Omega_{\mathrm{TE}} \end{pmatrix} \tag{5.5}$$

and

$$R = \begin{pmatrix} \rho_{\mathrm{TM}} & 0 \\ \rho_{\mathrm{P}} & 0 \\ 0 & \rho_{\mathrm{TE}} \end{pmatrix} \tag{5.6}$$

are introduced. Here, the terms $\Omega_i = \omega_i - \omega - i\gamma_i/2$, $(i = \mathrm{TM}, \mathrm{P}, \mathrm{TE})$ contain the eigenfrequencies and damping coefficients of the individual oscillators. The magneto-optic coefficient β is proportional to the gyration of the waveguide material and, thus, to the applied magnetic field. The occurrence with two different signs originates from the cross product in the Lorentz force. The nonzero components ρ_i $(i = \mathrm{TM}, \mathrm{P}, \mathrm{TE})$ in the matrix R are proportional to the charge of the oscillators and relate to the individual oscillator strengths. η is a proportionality constant.

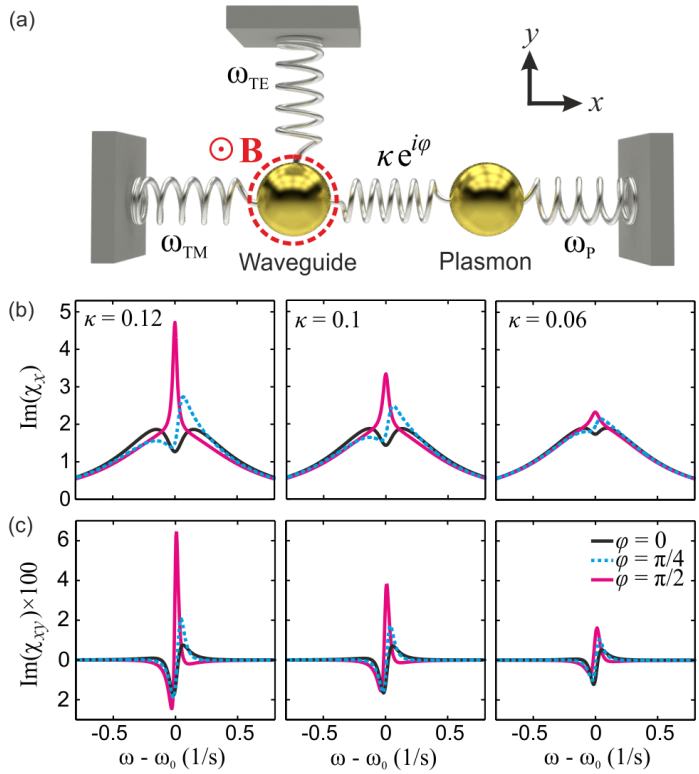

Figure 5.8: (a) Oscillator model representing the magneto-plasmonic nanostructure. A precondition for EIA is that the coupling between the TM waveguide mode and the plasmon mode is weak and includes retardation. This is taken into account by the complex coupling constant $\kappa \exp(i\phi)$ with phase ϕ. (b) Imaginary part of the component χ_x, which is proportional to the absorbance of x-polarized incident light. (c) Imaginary part of χ_{xy}, which induces polarization rotation of both x- and y-polarized incident light.

In the following, this model is used to illustrate the relation between the EIA and EIT coupling regimes as well as their influence on the magneto-optic response. For this, to keep the degrees of freedom to a minimum, the following simple (and dimensionless) parameter constellation is utilized: The individual resonances in the system are spectrally close, while the waveguide modes hav-

ing significantly smaller linewidths than the plasmon. Hence, the eigenfrequencies of the three oscillators are assumed to be equal, i.e., $\omega_{TM} = \omega_{TE} = \omega_P = \omega_0$ and for the damping coefficients it is assumed that $\gamma_P = 1$ and $\gamma_{TM} = \gamma_{TE} = 0.1$. Furthermore, the proportionality constant η is set to 1 and it is assumed that the plasmon oscillator couples much stronger to the external light field than to the TM waveguide mode. Hence, the oscillator strengths are weighted by setting $\rho_{TM} = 0$ and $\rho_P = 1$. Furthermore, the oscillator strength of the TE waveguide oscillator was set to $\rho_{TE} = 0.32$, which represents the case in which χ_x and χ_y (not shown here) are approximately equal.

The plots in figure 5.8b show the resulting frequency dependence of the imaginary part of χ_x, which is proportional to the absorbance of x-polarized incident light. The different line colors correspond to the different coupling phases. Furthermore, from the left to the right column, the coupling amplitude κ is decreased. All spectra of χ_x show a broad, mainly plasmon-induced, background with a sharp modulation on top. For $\phi = 0$ this modulation is a narrow dip at ω_0 and corresponds to the case of EIT. Increasing the coupling phase to $\phi = \pi/2$ turns this modulation into a narrow EIA resonance, while the case of $\phi = \pi/4$ represents an intermediate regime. Furthermore, an increase of κ leads to a more pronounced modulation. However, at some point when κ is increased further (not shown here), the coupling is not weak anymore and a significant mode splitting occurs for $\phi = 0$, and for $\phi = \pi/2$ nonphysical solutions with negative absorption can emerge [111]. In summary, the classical analogs of EIT and EIA are indeed very closely related: Both scenarios occur in the regime of weak coupling where there is no significant spectral repulsion between the narrow linewidth mode (in this case, the TM waveguide mode) and the broad linewidth mode (in this case, the plasmon). The only difference between the two scenarios lies in the coupling phase ϕ. It should be pointed out that the absorption behavior is approximately independent of the magnetic field, as $|\beta|$ can be assumed to be small (her, it is set to 0.001), in

which case it predominantly influences the off-diagonal elements of χ but not the diagonal elements [102].

The corresponding magneto-optic response is encoded in the off-diagonal elements of χ that are proportional to β and, thus, to the magnetic field. In first approximation, the Faraday rotation of the system is proportional to the imaginary part of χ_{xy} (see section 2.2.3), which is plotted in figure 5.8c. It should be noted that the real part of χ_{xy} would correspond to the ellipticity (not plotted here). The graphs nicely illustrate the fundamental working principle of the system: With increasing κ , not only the modulation of χ_x increases (i.e., the EIA or EIT resonances become more pronounced), but also the modulation of χ_{xy} becomes stronger. In other words, due to the magnetic field, the EIA or EIT resonances not only occur in absorption, but also in Faraday rotation. The more pronounced the EIA or EIT resonances are, the larger the Faraday rotation enhancement becomes. Furthermore, for a constant κ this modulation of χ_{xy} is strongest for $\phi = \pi/2$, i.e., for the EIA case. At this point it should be noted that in practice the difference in the MO response obtained by EIA-like and EIT-like coupling can be less pronounced than in the modeled spectra. The reason is that tuning the structure geometry from the EIT to the EIA case usually also slightly influences the other coupling parameters such as κ, which also have a strong influence on χ_{xy}. However, the model correctly reflects the trend that the EIA case produces stronger MO response than the EIT case. Another revealing aspect of this model is that although only the oscillators moving in the x direction contribute to the EIA resonance, this resonance also leads to increased polarization rotation for y-polarized light: This follows from the fact that χ is antisymmetric. Hence, the resonance in χ_{xy} translates to a conversion from x to y polarization as well as to a conversion from y to x polarization. However, in general, the Faraday rotation spectra for x- and y-polarized light are not completely equal since for finite propagation distances also the diagonal components χ_x and χ_y possess an influence [54, 102]. As shown by the measurements in figure 5.4, the Faraday rotation can be even larger for y-polarized

light than for x-polarized light. It should also be pointed out that the line shape of χ_{xy} depends on the complex phase of the magneto optical coupling constant β, which is related to the gyration of the MO material [102]. For the present example, this phase is set to $-45°$. Changing this phase does not affect the average magnitude of the magneto-optic response, but only determines whether the $\mathrm{Im}(\chi_{xy})$ spectra show a down-up line shape (negative phase), an up-down line shape (positive phase), or a peak (zero phase) when plotted over angular frequency [2].

As a final remark, it should be mentioned that the presented oscillator model is the simplest possible approach to illustrate the relation between EIA-like coupling and the enhanced MO response in the system. Of course, this results in neglecting secondary influences observed in the actual measurements, such as material dispersion, background Faraday rotation due to the film, or diffraction effects such as Rayleigh anomalies [102]. Nevertheless, the benefit of this model is that it provides a very intuitive description of the system.

5.4 CONCLUSION

The design flexibility enabled by the use of EuS as magneto-optic material was exploited to realize a hybrid magnetoplasmonic thin film structure that represents the classical optical analog of EIA. Unlike in previous approaches where the low quality factor of localized surface plasmon resonances limited the Faraday rotation enhancement, the coupling regime of EIA allows us to leverage both the high quality factor of the waveguide resonances and the large oscillator strength of the plasmons. Both these aspects result in dramatically increased light-matter interaction and MO response. As a result, the EIA-like system induces giant Faraday rotation of over $14°$ for a thickness of less than 200 nm and a mag-

2 Due to the ω based mathematical structure of the model, the response curves were plotted over angular frequency. This should be kept in mind when the modeled spectra are compared to the measured spectra, which are plotted over wavelength.

netic field of 5 T at $T = 20$ K. By varying the magnetic field from -5 T to $+5$ T, an impressing rotation tuning range of over 25° is realized. This is a MO performance that exceeds any previous approach considerably.

6

CONCLUSION AND OUTLOOK

In this dissertation, the magneto-optic (MO) dispersion properties of different hybrid magnetoplasmonic systems were analyzed both in experiment and theory. The study of the unique dispersion properties of such systems enabled the realization of ultrathin tunable Faraday rotators with designated working wavelength and a magneto-optic response that is unprecedented for such thin structures.

The utilized magnetoplasmonic geometries can be divided into two types: The first type consists of a MO thin film with an attached gold grating on top. The strong coupling between a plasmon resonance in the gold grating and a waveguide mode in the MO film results in the formation of a waveguide-plasmon-polariton (WPP), which facilitates large Faraday rotation of up to 4° for a 220 nm thick EuSe-Au structure. However, even stronger MO response was obtained for the second type: Here, a plasmonic gold grating is embedded into a MO film. It was demonstrated both in experiment and theory that this system can be regarded as a classical optical analog of electromagnetically induced absorption (EIA). The resulting unique dispersion properties of this system allow to compensate for the low Q factor of the plasmonic resonance, which limits the MO response in the WPP-based approach. The presented EIA-like EuS-Au structure induces giant Faraday rotation of up to 14° for a thickness of less than 200 nm and a magnetic field of 5 T at $T = 20$ K. Furthermore, by varying the magnetic field from -5 to $+5$ T, the polarization of the transmitted light can be continuously tuned over an impressively wide range of over 25°. As the realized magneto-optic response is only a factor of three away from the Faraday isolation requirement, the demonstrated concept could lead to highly integrated, nonreciprocal photonic devices for optical isolation,

light modulation, and optical magnetic field sensing. Furthermore, as was demonstrated recently, strong MO dispersion of nanostructured systems can also be leveraged for refractive index sensing, allowing very precise detection of biochemical substances [107]. Here, the exceptionally sharp spectral features in the MO response of EIA systems could also turn out to be a powerful tool.

A fruitful strategy to even further increase the MO response of the EuS-Au structures could be to use a thicker MO slab in combination with grating periods that are comparable to the ones used in chapter 5. This way, higher-order waveguide resonances can be excited, which, in combination with EIA-like dispersion, could lead to Faraday rotation values closer to or even above 45°. Furthermore, some sort of physical or chemical treatment to enhance the surface quality of the EuS film is expected to further increase the resonator performance resulting in larger Faraday rotation. In future designs, the necessity for low temperatures could be significantly relaxed by doping europium compounds with gadolinium. For example, it has been shown that doping EuO with gadolinium can raise the Curie temperature (where the Faraday rotation starts to drop) from 69 to 135 K [67, 101], which is well above liquid nitrogen temperature. Of course, the concept of WPP- and EIA-boosted MO response is not restricted to Eu compounds and can in principle be applied to many materials. The only requirements are a sufficient transparency of the MO material and a suitable procedure for the nanostructure fabrication.

Moreover, it was proven that EuS enables simple fabrication of complex layer-based magneto-optic geometries. This is a very powerful and rare property among transparent magneto-optic materials. Since EuS is much cheaper than EuSe and also provides stronger MO response already at low magnetic fields, EuS could become a trigger for other interesting and potentially very powerful magneto-optic and magnetoplasmonic designs. This could include both 2D and 3D systems, for instance EuS photonic crystals, as well as even magneto-optic metamaterials [24, 132].

Last but not least, the theory presented in this dissertation, now allows to describe the optical response of hybrid magnetoplasmonic systems in the picture of a simple oscillator model based on the Lorentz force. This model provides analytical expressions for the optical response and confirms previous numerical and experimental findings. One important outcome of the model is that the spectral line shape of the MO response is fully determined by the optical properties of the system for zero magnetic field. Only the overall magnitude of the MO response is determined by the applied magnetic field. The presented theory could significantly facilitate the optimization of both existing and also new magnetoplasmonic systems, such as 2D and 3D systems. Furthermore, by removing all plasmonic oscillators, the case of a purely dielectric grating-waveguide combination can be modeled. In prospect of non-linear magnetoplasmonics, the presented model could also be of fundamental relevance. Although the model is fully linear, a non-linear extension would be straight-forward by adding higher order coupling terms [108].

BIBLIOGRAPHY

[1] P. N. Schatz and A. J. McCaffery, "The Faraday Effect," Q. Rev. Chem. Soc. **23**, 552 (1969).

[2] Z. Q. Qui and S. D. Bader, "Surface magneto-optic Kerr effect," Rev. Sci. Instrum. **71**, 1243 (2000).

[3] A. de Hoop, "A reciprocity theorem for the electromagnetic field scattered by an obstacle," Appl. Sci. Res. Sect. B **8**, 135–140 (1960).

[4] I. Tinoco, "Theoretical Aspects of Optical Activity Part Two: Polymers," in *Adv. Chem. Phys.* (John Wiley & Sons, Inc., 2007), pp. 113–160.

[5] M. Soljaic, C. Y. Luo, J. D. Joannopoulos, and S. H. Fan, "Nonlinear photonic microdevices for optical integration," Opt. Lett. **28**, 637–639 (2003).

[6] S. Lepri and G. Casati, "Asymmetric wave propagation in nonlinear systems," Phys. Rev. Lett. **106**, 164 101 (2011).

[7] I. V. Shadrivov, V. A. Fedotov, D. A. Powell, Y. S. Kivshar, and N. I. Zheludev, "Electromagnetic wave analogue of an electronic diode," New J. Phys. **13**, 033 025 (2011).

[8] Z. Yu and S. Fan, "Complete optical isolation created by indirect interband photonic transitions," Nat. Photonics **3**, 91–94 (2009).

[9] M. S. Kang, A. Butsch, and P. S. J. Russell, "Reconfigurable light-driven opto-acoustic isolators in photonic crystal fibre," Nat. Photonics **5**, 549–553 (2011).

[10] S. Fan, R. Baets, A. Petrov, Z. Yu, J. D. Joannopoulos, W. Freude, A. Melloni, M. Popović, M. Vanwolleghem,

D. Jalas, M. Eich, M. Krause, H. Renner, E. Brinkmeyer, and C. R. Doerr, "Comment on 'Nonreciprocal light propagation in a silicon photonic circuit'," Science **335**, 38 (2012).

[11] D. W. Wang, H. T. Zhou, M. J. Guo, J. X. Zhang, J. Evers, and S. Y. Zhu, "Optical diode made from a moving photonic crystal," Phys. Rev. Lett. **110**, 093 901 (2013).

[12] D. Sounas, C. Caloz, and A. Alù, "Giant non-reciprocity at the subwavelength scale using angular momentum-biased metamaterials," Nat. Commun. **4**, 2407 (2013).

[13] C. Firby, P. Chang, A. Helmy, and A. Elezzabi, "Magnetoplasmonic Faraday Rotators: Enabling Gigahertz Active Polarization Control for Integrated Plasmonics," ACS Photonics **3**, 2344 (2016).

[14] M. Shirasaki and K. Asama, "Compact optical isolator for fibers using birefringent wedges," Appl. Opt. **21**, 4296–4299 (1982).

[15] L. Bi, J. Hu, P. Jiang, and D. Kim, "On-chip optical isolation in monolithically integrated non-reciprocal optical resonators," Nat. Photonics **5**, 758–762 (2011).

[16] L. Fan, J. Wang, L. T. Varghese, H. Shen, B. Niu, Y. Xuan, A. M. Weiner, and M. Qi, "An all-silicon passive optical diode," Science **335**, 447–450 (2012).

[17] I. Ikushima and M. Maeda, "Self-coupled phenomena of semiconductor lasers caused by an optical fiber," IEEE J. Quantum Electron. **14**, 331–332 (1978).

[18] T. Morikawa, Y. Mitsuhashi, J. Shimada, and Y. Kojima, "Return-beam-induced oscillations in self-coupled semiconductor lasers," Electron. Lett. **12**, 435 (1976).

[19] K. Petermann, "External optical feedback phenomena in semiconductor lasers," IEEE J. Sel. Top. Quantum Electron. **1**, 480–489 (1995).

[20] L. Sun, S. Jiang, and J. R. Marciante, "All-fiber optical magnetic-field sensor based on Faraday rotation in highly terbium-doped fiber," Opt. Express **18**, 5407–5412 (2010).

[21] M. N. Deeter, A. H. Rose, and G. W. Day, "Fast, sensitive magnetic-field sensors based on the Faraday effect in YIG," J. Light. Technol. **8**, 1838–1842 (1990).

[22] W. E. Ross, "Two-dimensional magneto-optic spatial light modulator for signal processing," Opt. Engeneering **22**, 485–490 (1983).

[23] M. Liu and X. Zhang, "Plasmon-boosted magneto-optics," Nat. Photonics **7**, 429–430 (2013).

[24] A. F. Koenderink, A. Alù, and A. Polman, "Nanophotonics: Shrinking light-based technology," Science **348**, 516 (2015).

[25] V. Temnov, G. Armelles, U. Woggon, D. Guzatov, A. Cebollada, A. Garcia-Martin, T. Thomay, A. Leitenstorfer, and R. Bratschitsch, "Active magneto-plasmonics in hybrid metal-ferromagnet structures," Nat. Photonics **4**, 107–111 (2010).

[26] V. I. Belotelov, I. A. Akimov, M. Pohl, V. A. Kotov, S. Kasture, A. S. Vengurlekar, A. V. Gopal, D. R. Yakovlev, A. K. Zvezdin, and M. Bayer, "Enhanced magneto-optical effects in magnetoplasmonic crystals," Nat. Nanotechnol. **6**, 370–376 (2011).

[27] V. Belotelov, L. Kreilkamp, I. Akimov, A. Kalish, D. Bykov, S. Kasture, V. Yallapragada, A. Venu Gopal, A. Grishin, S. Khartsev, M. Nur-E-Alam, M. Vasiliev, L. Doskolovich, D. Yakovlev, K. Alameh, A. Zvezdin, and M. Bayer, "Plasmon-mediated magneto-optical transparency," Nat. Commun. **4**, 2128 (2013).

[28] A. R. Davoyan and N. Engheta, "Nonreciprocal Rotating Power Flow within Plasmonic Nanostructures," Phys. Rev. Lett. **111**, 047 401 (2013).

[29] S. Fan, "Nanophotonics: Magnet-controlled plasmons," Nat. Photonics **4**, 76–77 (2010).

[30] A. B. Khanikaev, S. H. Mousavi, G. Shvets, and Y. S. Kivshar, "One-way extraordinary optical transmission and nonreciprocal spoof plasmons," Phys. Rev. Lett. **105**, 126 804 (2010).

[31] Z. Gevorkian and V. Gasparian, "Plasmon-enhanced Faraday rotation in thin films," Phys. Rev. A **89**, 023 830 (2014).

[32] P. K. Jain, Y. Xiao, R. Walsworth, and A. E. Cohen, "Surface plasmon resonance enhanced magneto-optics (SuPREMO): Faraday rotation enhancement in gold-coated iron oxide nanocrystals," Nano Lett. **9**, 1644–1650 (2009).

[33] M. J. Steel, M. Levy, and R. M. Osgood, "High transmission enhanced Faraday rotation in one-dimensional photonic crystals with defects," IEEE Photonics Technol. Lett. **12**, 1171–1173 (2000).

[34] A. A. Fedyanin, O. A. Aktsipetrov, D. Kobayashi, K. Nishimura, H. Uchida, and M. Inoue, "Enhanced Faraday and nonlinear magneto-optical Kerr effects in magnetophotonic crystals," J. Magn. Magn. Mater. **282**, 256–259 (2004).

[35] M. Diwekar, V. Kamaev, J. Shi, and Z. V. Vardeny, "Optical and magneto-optical studies of two-dimensional metallodielectric photonic crystals on cobalt films," Appl. Phys. Lett. **84**, 3112–3114 (2004).

[36] B. Caballero, A. García-Martín, and J. C. Cuevas, "Faraday effect in hybrid magneto-plasmonic photonic crystals," Opt. Express **23**, 22 238 (2015).

[37] B. Caballero, A. Garciá-Martín, and J. C. Cuevas, "Hybrid Magnetoplasmonic Crystals Boost the Performance of Nanohole Arrays as Plasmonic Sensors," ACS Photonics **3**, 203–208 (2016).

[38] R. Rosenberg, C. B. Rubinstein, and D. R. Herriott, "Resonant Optical Faraday Rotator," Appl. Opt. **3**, 1079–1083 (1964).

[39] M. Inoue, K. Arai, T. Fujii, and M. Abe, "One-dimensional magnetophotonic crystals," J. Appl. Phys. **85**, 5768 (1999).

[40] S. I. Khartsev and A. M. Grishin, "High performance [Bi3Fe5O12/Sm3Ga5O12]m magneto-optical photonic crystals," J. Appl. Phys. **101**, 053 906 (2007).

[41] B. Sepúlveda, J. B. González-Díaz, A. García-Martín, L. M. Lechuga, and G. Armelles, "Plasmon-Induced Magneto-Optical Activity in Nanosized Gold Disks," Phys. Rev. Lett. **104**, 147 401 (2010).

[42] J. B. González-Díaz, B. Sepúlveda, A. García-Martín, and G. Armelles, "Cobalt dependence of the magneto-optical response in magnetoplasmonic nanodisks," Appl. Phys. Lett. **97**, 043 114 (2010).

[43] J. C. Banthí, D. Meneses-Rodríguez, F. García, M. U. González, A. García-Martín, A. Cebollada, and G. Armelles, "High Magneto-Optical Activity and Low Optical Losses in Metal-Dielectric Au/Co/Au-SiO(2) Magnetoplasmonic Nanodisks," Adv. Mater. **24**, OP36 (2012).

[44] M. Kataja, T. K. Hakala, A. Julku, M. J. Huttunen, S. van Dijken, and P. Törmä, "Surface lattice resonances and magneto-optical response in magnetic nanoparticle arrays," Nat. Commun. **6**, 7072 (2015).

[45] L. E. Kreilkamp, V. I. Belotelov, J. Y. Chin, S. Neutzner, D. Dregely, T. Wehlus, I. A. Akimov, M. Bayer, B. Stritzker, and H. Giessen, "Waveguide-Plasmon Polaritons Enhance Transverse Magneto-Optical Kerr Effect," Phys. Rev. X **3**, 041 019 (2013).

[46] V. I. Belotelov, L. L. Doskolovich, and A. K. Zvezdin, "Extraordinary Magneto-Optical Effects and Transmission through Metal-Dielectric Plasmonic Systems," Phys. Rev. Lett. **98**, 077 401 (2007).

[47] J. Y. Chin, T. Steinle, T. Wehlus, D. Dregely, T. Weiss, V. I. Belotelov, B. Stritzker, and H. Giessen, "Nonreciprocal plasmonics enables giant enhancement of thin-film Faraday rotation," Nat. Commun. **4**, 1599 (2013).

[48] A. Christ, S. G. Tikhodeev, N. A. Gippius, J. Kuhl, and H. Giessen, "Waveguide-Plasmon Polaritons: Strong Coupling of Photonic and Electronic Resonances in a Metallic Photonic Crystal Slab," Phys. Rev. Lett. **91**, 183 901 (2003).

[49] A. Christ, T. Zentgraf, J. Kuhl, S. G. Tikhodeev, N. A. Gippius, and H. Giessen, "Optical properties of planar metallic photonic crystal structures: Experiment and theory," Phys. Rev. B **70**, 125 113 (2004).

[50] S. Linden, J. Kuhl, and H. Giessen, "Controlling the Interaction between Light and Gold Nanoparticles: Selective Suppression of Extinction," Phys. Rev. Lett. **86**, 4688–4691 (2001).

[51] A. M. Akulshin, S. Barreiro, and A. Lezama, "Electromagnetically induced absorption and transparency due to resonant two-field excitation of quasidegenerate levels in Rb vapor," Phys. Rev. A **57**, 2996–3002 (1998).

[52] A. Lezama, S. Barreiro, and A. M. Akulshin, "Electromagnetically induced absorption," Phys. Rev. A **59**, 4732–4735 (1999).

[53] D. Floess, J. Y. Chin, A. Kawatani, D. Dregely, H.-U. Habermeier, T. Weiss, and H. Giessen, "Tunable and switchable polarization rotation with non-reciprocal plasmonic thin films at designated wavelengths," Light Sci. Appl. **4**, e284 (2015).

[54] A. K. Zvezdin and V. A. Kotov, *Modern Magnetooptics and Magnetooptical Materials* (IOP Publishing Ltd, 1997).

[55] H. Fujiwara, *Spectroscopic Ellipsometry: Principles and Applications* (John Wiley & Sons, Inc., West Sussex, 2007).

[56] J. D. Jackson, *Classical Electrodynamics* (John Wiley & Sons, Inc., 1999), 3rd edn.

[57] A. Yariv and P. Yeh, *Photonics* (Oxford University Press, 2007), 6th edn.

[58] L. Landau and E. Lifshitz, *Electrodynamics of Continous Media* (Pergamon Press, 1960).

[59] R. J. Potton, "Reciprocity in optics," Reports Prog. Phys. **67**, 717–754 (2004).

[60] G. R. Fowles, *Introduction to Modern Optics* (Dover Publications, New York, 1975), 2nd edn.

[61] F. A. Hopf and G. I. Stegeman, "Applied Classical Electrodynamics," in *Vol. I Linear Opt.* (Krieger Publishing Company, 1992).

[62] M. Fox, *Optical Properties of Solids* (Oxford University Press, 2010), 2nd edn.

[63] J. Schoenes, "Magnetooptik und elektronische Struktur der magnetisch ordnenden Europiumchalkogenide," Zeitschrift für Phys. B Condens. Matter **20**, 345–368 (1975).

[64] X. Yin, M. Schäferling, B. Metzger, and H. Giessen, "Interpreting chiral nanophotonic spectra: The plasmonic Born-Kuhn model," Nano Lett. **13**, 6238–6243 (2013).

[65] J. F. Dillon, "Origin and Uses of the Faraday Rotation in Magnetic Crystals," J. Appl. Phys. **39**, 922 (1968).

[66] J. T. Devreese, *Theoretical Aspects and New Developments in Magneto-Optics* (Plenum Press, New York, 1980).

[67] J. Schoenes and P. Wachter, "Exchange optics in Gd-doped EuO," Phys. Rev. B **9**, 3097–3105 (1974).

[68] P. Wachter, "Europium Chalcogenides: EuO, EuS, EuSe and EuTe," in *Handb. Phys. Chem. Rare Earths* (North-Holland Publishing Company, Amsterdam, 1979), Vol. 2, pp. 507–574.

[69] Y. Shen and N. Bloembergen, "Faraday Rotation of Rare-Earth Ions in Ca F 2. II. Experiments," Phys. Rev. **257**, 5–10 (1964).

[70] T. Wehlus, T. Körner, S. Leitenmeier, A. Heinrich, and B. Stritzker, "Magneto-optical garnets for integrated optoelectronic devices," Phys. Status Solidi **208**, 252–263 (2011).

[71] R. W. Cooper, W. A. Crossley, J. L. Page, and R. F. Pearson, "Faraday rotation in YIG and TbIG," J. Appl. Phys. **39**, 565–567 (1968).

[72] S. Maier, *Plasmonics: Fundamentals and Applications* (Springer Science+Business Media LLC, New York, 2007).

[73] A. Tittl, H. Giessen, and N. Liu, "Plasmonic gas and chemical sensing," Nanomater. Nanoarchitectures A Complex Rev. Curr. Hot Top. their Appl. **3**, 239–272 (2015).

[74] G. Mie, "Beiträge zur Optik trüber Medien, speziell kolloidaler Metallösungen," Ann. Phys. **330**, 377–445 (1908).

[75] S. G. Tikhodeev, A. L. Yablonskii, E. A. Muljarov, N. A. Gippius, and T. Ishihara, "Quasiguided modes and optical properties of photonic crystal slabs," Phys. Rev. B **66**, 045 102 (2002).

[76] S. Linden, *Kontrolle der Wechselwirkung zwischen Licht und Partikelplasmonen durch selektive Unterdrückung der Extinktion*, Ph.D. thesis, Philipps-Universität Marburg (2001).

[77] A. Christ, *Optical properties of metallic photonic crystal structures*, Ph.D. thesis, University of Stuttgart (2005).

[78] P. K. Tien, R. Ulrich, and R. J. Martin, "Modes of propagating light waves in thin deposited semiconductor films," Appl. Phys. Lett. **14**, 291–294 (1969).

[79] J. E. Midwinter, "Evanescent field coupling into a thin-film waveguide," IEEE J. Quantum Electron. **6** (1970).

[80] C. Kittel, *Introduction to Solid State Physics* (John Wiley & Sons, Inc., 2004).

[81] J. C. Suits and B. E. Argyle, "Paramagnetic Faraday Rotation of EuSe," J. Appl. Phys. **36**, 1251–1252 (1965).

[82] J. Schoenes and P. Wachter, "High field magneto-optical study of EuSe and EuTe," Phys. B **89B**, 155–158 (1977).

[83] J. Suits and B. Argyle, "Magnetic birefringence of EuSe," Phys. Rev. Lett. **14**, 687–689 (1965).

[84] E. Mahan, *Physical Vapor Deposition of Thin Films* (Wiley-VCH, 2000).

[85] N. Koshizuka, "Research activities on magneto-optical devices in Japan," IEEE Trans. Magn. **23**, 3473 (1987).

[86] A. Ohido, T. Sugawara, K. Yamasawa, S. Kakei, K. Shimakawa, and K. Hosoya, "US Patent 7,517,406: Magnetic garnet material, faraday rotator, optical device, bismuth-substituted rare earth-iron-garnet single-crystal film and method for producing the same and crucible for producing the same," (2009).

[87] K. Shirai and N. Takeda, "US Patent 5,925,474: Bismuth-substituted rare earth iron garnet single crystal film," (1999).

[88] K. Shirai and N. Takeda, "US Patent 6,411,641: Faraday rotator for use with high energy lasers," (2002).

[89] *Thorlabs online catalog* (Availible at www.thorlabs.de, accessed 23 July 2014).

[90] C. Vieu, F. Carcenac, A. Pépin, Y. Chen, M. Mejias, A. Lebib, L. Manin-Ferlazzo, L. Couraud, and H. Launois, "Electron beam lithography: resolution limits and applications," (2000).

[91] T. Weiss, N. A. Gippius, S. G. Tikhodeev, G. Granet, and H. Giessen, "Derivation of plasmonic resonances in the Fourier modal method with adaptive spatial resolution and matched coordinates," J. Opt. Soc. Am. A **28**, 238–244 (2011).

[92] P. B. Johnson and R. W. Christy, "Optical constants of the noble metals," Phys. Rev. B **6**, 4370 (1972).

[93] G. Güntherodt, J. Schoenes, and P. Wachter, "Optical Constants of the Eu Chalcogenides Above and Below the Magnetic Ordering Temperatures," J. Appl. Phys. **41**, 1083 (1970).

[94] H. C. Guo, D. Nau, A. Radke, X. P. Zhang, J. Stodolka, X. L. Yang, S. G. Tikhodeev, N. a. Gippius, and H. Giessen, "Large-area metallic photonic crystal fabrication with interference lithography and dry etching," Appl. Phys. B **81**, 271–275 (2005).

[95] S. Bagheri, H. Giessen, and F. Neubrech, "Large-Area Antenna-Assisted SEIRA Substrates by Laser Interference Lithography," Adv. Opt. Mater. **2**, 1050–1056 (2014).

[96] X. Wang, G. Venugopal, J. Zeng, Y. Chen, D. H. Lee, N. M. Litchinitser, and A. N. Cartwright, "Optical fiber metamagnetics," Opt. Express **19**, 19 813–19 821 (2011).

[97] Y. Lin, Y. Zou, Y. Mo, J. Guo, and R. G. Lindquist, "E-beam patterned gold nanodot arrays on optical fiber tips for localized surface plasmon resonance biochemical sensing," Sensors **10**, 9397–406 (2010).

[98] X. Zeng, S. Jradi, J. Proust, R. Bachelot, Z. P. Zhang, P. Royer, and J. Plain, "Direct functionalization of an optical fiber by a plasmonic nanosensor," Opt. Lett. **36**, 2919–2921 (2011).

[99] D. J. Dentz, R. C. Puttbach, and R. F. Belt, "Terbium Gallium garnet for Faraday Effect Devices," AIP Conf. Proc. **18**, 954–958 (1974).

[100] K. Ahn and J. Suits, "Preparation and properties of EuO films," IEEE Trans. Magn. **3**, 2–4 (1967).

[101] M. W. Shafer, "Studies of Curie-Point Increases in EuO," J. Appl. Phys. **39**, 588–590 (1968).

[102] D. Floess, T. Weiss, S. G. Tikhodeev, and H. Giessen, "Lorentz nonreciprocal model for hybrid magnetoplasmonics," Phys. Rev. Lett. **117**, 063 901 (2016).

[103] M. B. Doost, W. Langbein, and E. A. Muljarov, "Resonant-state expansion applied to three-dimensional open optical systems," Phys. Rev. A **90**, 013 834 (2014).

[104] T. Weiss, M. Mesch, M. Schäferling, H. Giessen, W. Langbein, and E. Muljarov, "From Dark to Bright: First-Order Perturbation Theory with Analytical Mode Normalization for Plasmonic Nanoantenna Arrays Applied to Refractive Index Sensing," Phys. Rev. Lett. **116**, 237 401 (2016).

[105] T. Weiss, G. Granet, N. A. Gippius, S. G. Tikhodeev, and H. Giessen, "Matched coordinates and adaptive spatial resolution in the Fourier modal method," Opt. Express **17**, 8051–8061 (2009).

[106] A. B. Akimov, N. A. Gippius, and S. G. Tikhodeev, "Optical Fano Resonances in Photonic Crystal Slabs near Diffraction Threshold Anomalies," JETP Lett. **93**, 427–430 (2011).

[107] N. Maccaferri, K. E. Gregorczyk, T. de Oliveira, M. Kataja, S. van Dijken, Z. Pirzadeh, A. Dmitriev, J. Åkerman, M. Knez, and P. Vavassori, "Ultrasensitive and label-free

molecular-level detection enabled by light phase control in magnetoplasmonic nanoantennas," Nat. Commun. **6**, 6150 (2015).

[108] B. Metzger, M. Hentschel, M. Lippitz, and H. Giessen, "Third-harmonic spectroscopy and modeling of the nonlinear response of plasmonic nanoantennas," Opt. Lett. **37**, 4741 (2012).

[109] D. Floess, M. Hentschel, T. Weiss, H.-U. Habermeier, J. Jiao, S. G. Tikhodeev, and H. Giessen, "Plasmonic Analog of Electromagnetically Induced Absorption Leads to Giant Thin Film Faraday Rotation of 14 deg," Phys. Rev. X **7**, 021 048 (2017).

[110] R. Taubert, M. Hentschel, J. Kästel, and H. Giessen, "Classical Analogue of Electromagnetically Induced Absorption in Plasmonics," Nano Lett. **12**, 1367 (2012).

[111] R. Taubert, M. Hentschel, and H. Giessen, "Plasmonic analog of electromagnetically induced absorption: simulations, experiments, and coupled oscillator analysis," J. Opt. Soc. Am. B **30**, 3123 (2013).

[112] S. E. Harris, "Electromagnetically Induced Transparency," Phys. Today **50**, 36 (1997).

[113] K. J. Boller, A. Imamoglu, and S. E. Harris, "Observation of electromagnetically induced transparency," Phys. Rev. Lett. **66**, 2593–2596 (1991).

[114] N. Liu, L. Langguth, T. Weiss, J. Kästel, M. Fleischhauer, T. Pfau, and H. Giessen, "Plasmonic analogue of electromagnetically induced transparency at the Drude damping limit," Nat. Mater. **8**, 758–62 (2009).

[115] N. Liu, T. Weiss, M. Mesch, L. Langguth, U. Eigenthaler, M. Hirscher, C. Sönnichsen, and H. Giessen, "Planar metamaterial analogue of electromagnetically induced trans-

parency for plasmonic sensing," Nano Lett. **10**, 1103–1107 (2010).

[116] N. Verellen, P. Van Dorpe, C. Huang, K. Lodewijks, G. A. E. Vandenbosch, L. Lagae, and V. V. Moshchalkov, "Plasmon line shaping using nanocrosses for high sensitivity localized surface plasmon resonance sensing," Nano Lett. **11**, 391–397 (2011).

[117] J. B. Lassiter, H. Sobhani, J. A. Fan, J. Kundu, F. Capasso, P. Nordlander, and N. J. Halas, "Fano resonances in plasmonic nanoclusters: Geometrical and chemical tunability," Nano Lett. **10**, 3184–3189 (2010).

[118] M. F. Yanik, W. Suh, Z. Wang, and S. Fan, "Stopping light in a waveguide with an all-optical analog of electromagnetically induced transparency," Phys. Rev. Lett. **93**, 233 903 (2004).

[119] K. Totsuka, N. Kobayashi, and M. Tomita, "Slow Light in Coupled-Resonator-Induced Transparency," Phys. Rev. Lett. **98**, 213 904 (2007).

[120] A. Schönhardt, D. Nau, C. Bauer, A. Christ, H. Gräbeldinger, and H. Giessen, "Phase-resolved pulse propagation through metallic photonic crystal slabs: plasmonic slow light," Philos. Trans. A **275** (2017).

[121] L. Maleki, A. B. Matsko, A. A. Savchenkov, and V. S. Ilchenko, "Tunable delay line with interacting whispering-gallery-mode resonators," Opt. Lett. **29**, 626–628 (2004).

[122] N. Papasimakis, V. A. Fedotov, N. I. Zheludev, and S. L. Prosvirnin, "Metamaterial analog of electromagnetically induced transparency," Phys. Rev. Lett. **101**, 253 903 (2008).

[123] M. Fleischhauer and J. P. Marangos, "Electromagnetically induced transparency: Optics in coherent media," Rev. Mod. Phys. **77**, 633–673 (2005).

[124] B. Metzger, T. Schumacher, M. Hentschel, M. Lippitz, and H. Giessen, "Third Harmonic Mechanism in Complex Plasmonic Fano Structures," ACS Photonics **1**, 471–476 (2014).

[125] H. Hayashi, S. Iwasa, N. J. Vasa, and T. Yoshitake, "Fabrication of Bi-doped YIG optical thin for electric current sensor by pulsed laser deposition," Appl. Surf. Sci. **198**, 463–466 (2002).

[126] T. Zentgraf, S. Zhang, R. F. Oulton, and X. Zhang, "Ultranarrow coupling-induced transparency bands in hybrid plasmonic systems," Phys. Rev. B **80**, 195 415 (2009).

[127] L. Li, "Fourier modal method for crossed anisotropic gratings with arbitrary permittivity and permeability tensors," J. Opt. A Pure Appl. Opt. **5**, 345 (2003).

[128] M. Sagawa, S. Fujimura, N. Togawa, H. Yamamoto, and Y. Matsuura, "New material for permanent magnets on a base of Nd and Fe," J. Appl. Phys. **55**, 2083–2087 (1984).

[129] K. Tanaka, N. Tatehata, K. Fujita, and K. Hirao, "Preparation and Faraday effect of EuS microcrystal-embedded oxide thin films," J. Appl. Phys. **89**, 2213 (2001).

[130] H. Reddy, U. Guler, A. V. Kildishev, A. Boltasseva, and V. M. Shalaev, "Temperature-dependent optical properties of gold thin films," Opt. Mater. Express **6**, 2776 (2016).

[131] D. B. Leviton and B. J. Frey, "Temperature-dependent absolute refractive index measurements of synthetic fused silica," in *Proc. SPIE* (2006), p. 62732K.

[132] G. Castaldi, V. Galdi, A. Alù, and N. Engheta, "Nonlocal transformation optics," Phys. Rev. Lett. **108**, 063 902 (2012).

DANKSAGUNG

An dieser Stelle möchte ich allen danken, die zum Erfolg dieser Forschungsarbeit, sowohl fachlich als auch anderweitig, beigetragen haben. Ganz besonders gilt mein Dank

- Prof. Dr. Harald Gießen, der mich in das 4. Physikalische Institut aufgenommen hat und mir ermöglichte auf einem spannenden Forschungsfeld zu arbeiten. Seine permanente Unterstützung und Anleitung haben entscheidend zum Erfolg dieser Arbeit beigetragen. Die Zusammenarbeit mit ihm empfand ich als großes Privilleg und sie hat mich sehr bereichert.
- Frau Prof. Dr. Barz und Herrn Prof. Dr. Holm für deren Bereitschaft Teil des Prüfungskomitees zu sein.
- Frau Dr. Christine von Rekowski für ihre Hilfe in allen organisatorischen Belangen.
- Dr. Jessie Yao Chin, die mich in der Anfangszeit meiner Promotion begleitet und unterstützt hat.
- Jun.-Prof. Dr. Thomas Weiss für die Einbringung seiner theoretischen Kenntnisse in allen Projekten, sowie für die Bereitstellung des von ihm entwickelten S-Matrix Codes.
- Dr. Mario Hentschel für die vielen wertvollen Diskussionen, sowohl fachlicher als auch persönlicher Natur. Unsere Zusammenarbeit hat mich sehr bereichert.
- meinem stets hilfsbereiten und immer gut gelaunten Bürokollegen Florian Sterl für die schöne Zeit in Raum 4.507.
- Monika Ubl für Ihre große Hilfe in allen Reinraumangelegenheiten.

- Michael Kube, der mich bei vielen handwerklichen Belangen unterstützt hat.
- den Mitarbeiterinnen und Mitarbeitern der mechanischen Werkstatt und der Tieftemperaturwerkstatt. Deren Hilfe in technischen Angelegenheiten waren essenziell für meine experimentelle Arbeit.
- Prof. Dr. Manfred Bayer, der uns freundlicherweise den Magnet-Kryostaten geliehen hat.
- Prof. Dr. Jürgen Weis, der mir ermöglichte den Reinraum und die Gerätschaften für die Elektronenstrahllithografie des Max-Planck-Institus für Festkörperfoschung zu nutzen.
- meinen geschätzten Kolleginnen und Kollegen des 4. Physikalischen Instituts für die tolle Arbeitsathmosphäre und die schönen Momente innerhalb und außerhalb der Arbeitszeit.

Zum Schluss möchte ich mich in ganz besonderem Maße bei meinen Eltern Albertha und Franz bedanken. Ohne deren uneingeschränkte Unterstützung wäre es mir nicht möglich gewesen das zu tun woran ich Freude habe. Außerdem danke ich von ganzem Herzen meiner liebsten Ruth, die mir in den entscheidenden Momenten immer Kraft gegeben hat.